

Electronic Thesis and Dissertation Repository

---

7-22-2013 12:00 AM

## Magnetic Resonance Imaging of Iron in Early Multiple Sclerosis at 3 Tesla

Matthew P. Quinn  
*The University of Western Ontario*

Supervisor  
Ravi Menon  
*The University of Western Ontario*

Graduate Program in Medical Biophysics  
A thesis submitted in partial fulfillment of the requirements for the degree in Doctor of Philosophy  
© Matthew P. Quinn 2013

Follow this and additional works at: <https://ir.lib.uwo.ca/etd>



Part of the [Nervous System Diseases Commons](#)

---

### Recommended Citation

Quinn, Matthew P., "Magnetic Resonance Imaging of Iron in Early Multiple Sclerosis at 3 Tesla" (2013).  
*Electronic Thesis and Dissertation Repository*. 1392.  
<https://ir.lib.uwo.ca/etd/1392>

This Dissertation/Thesis is brought to you for free and open access by Scholarship@Western. It has been accepted for inclusion in Electronic Thesis and Dissertation Repository by an authorized administrator of Scholarship@Western. For more information, please contact [wlsadmin@uwo.ca](mailto:wlsadmin@uwo.ca).

**MAGNETIC RESONANCE IMAGING OF IRON  
IN EARLY MULTIPLE SCLEROSIS AT 3 TESLA**

(Thesis format: Integrated Article)

by

Matthew P Quinn

Graduate Program in Medical Biophysics

A thesis submitted in partial fulfillment  
of the requirements for the degree of  
Doctor of Philosophy

The School of Graduate and Postdoctoral Studies  
The University of Western Ontario  
London, Ontario, Canada

© Matthew Quinn 2013

## Abstract

Multiple sclerosis (MS) is the most common neurological disease in young Canadians, yet its etiology remains obscure. Two possibly related findings in MS are brain iron deposition and the presence of small veins in white matter lesions. This thesis concerns the development and application of 3 Tesla magnetic resonance imaging tools to image iron and veins in early multiple sclerosis.

To facilitate measurements of iron concentration as well as production of cerebral venograms, we first optimized multi-echo susceptibility weighted imaging (SWI), using numerical simulations and input from physicians. We validated measurements of  $R2^*$ , an MRI parameter that scales linearly with iron concentration.

Subsequently, we proposed quantification of the caliber of the internal jugular veins (IJVs) from magnetic resonance venograms. IJVs are implicated in the chronic cerebrospinal venous insufficiency model of MS, an increasingly disputed theory that attributes iron deposition in MS to venous abnormalities. We report that the coefficient of variation of measurements of average cross-sectional area of the IJVs is on the order of 7%.

We performed quantitative investigations of iron concentration in a cohort of patients at risk of MS diagnosis, compared to healthy controls. We report increased  $R2^*$  (putative iron) in deep as well as cortical grey matter in patients. We subsequently measured IJV area, finding a trend for reduced total IJV caliber in patients; however, we found no correlation between  $R2^*$  changes and IJV area.

We investigated the ability of multi-echo SWI to detect central veins within white matter hyperintensities (WMHs). We found that patients who converted from clinically isolated syndrome (CIS) to MS had a larger fraction of lesions with central veins compared to patients with non-converted CIS and healthy controls. Moreover, all patients who

received a diagnosis of MS within the study window had >40% lesions with central veins at their CIS baselines, suggesting there may be predictive value in this biomarker.

The subjects from these last two studies represent a subset of our cohort in an ongoing longitudinal study. Using methodology described herein, we are equipped to further investigate different biomarkers of disease to better understand early pathology in MS.

## Keywords

Multiple sclerosis, MRI, brain iron, clinically isolated syndromes, susceptibility weighted imaging, cervical veins



## Co-Authorship Statement

Much of Chapter 2 derives from a manuscript accepted for publication in the American Journal of Neuroradiology that was co-authored by Matthew Quinn, Joseph Gati, Martyn Klassen, Amy Lin, Stephanie Leung, Jeffery Bird, and Ravi Menon. Mr. Quinn, Mr. Gati, Dr. Klassen, and Dr. Menon were involved in conceptual development of this study. Mr. Quinn performed all experiment work, including data acquisition and analyses. Drs. Lin, Leung and Bird are radiology residents that performed image ratings and offered clinical viewpoints. Mr. Quinn drafted the original version of this manuscript; all authors were involved in review and editing. The release of copyright of this manuscript is included in Appendix C.

Chapter 4 derives from a manuscript accepted for publication in Multiple Sclerosis and Related Disorders. This manuscript was co-authored by Matthew Quinn, Joseph Gati, Martyn Klassen, Marcelo Kremenchtzky, Donald Lee, and Ravi Menon. All authors were involved in conceptual design of this study. Mr. Quinn performed all experimental work. Mr. Quinn drafted the original version of this manuscript; all other authors were involved in review and editing. The release of copyright of this manuscript is included in Appendix D.

## Acknowledgments

I am indebted to my supervisor, Dr. Ravi Menon, for the opportunity to contribute to this exciting project. I am truly appreciative of his endless insights, creativity, and the ability to lead me towards a good scientific explanation for otherwise boggling results.

I would also like to thank my advisory committee members for their guidance: Drs. Greg Dekaban, Paula Foster, and Martyn Klassen. In particular, I would like to express my gratitude to Dr. Marcelo Kremenchutzky for his efforts to recruit patients in addition to his mentorship and the opportunity to learn about multiple sclerosis first hand in his clinic.

Additionally, Dr. Sarah Morrow was instrumental in recruitment of several patients. Dr. Don Lee, on numerous occasions, offered invaluable radiological expertise. Dr. Amy Lin was always very excited to help, be it with lesion segmentation, image reading, or recruitment of other radiology residents for various experiments. To all of these physicians, I would like to extend my heartfelt thanks.

I would like to thank lab members: Joe Gati for his expertise and cleverness, and Dave Rudko for our surprisingly productive coffee breaks. I am also grateful for the dedication of Jennifer Moussa, our absolutely terrific study coordinator.

Finally, without the love and support of my parents Rick and Diane, siblings Jason, Nikki, and Emily, and my best friend Meg, I would not possess the drive towards excellence which is responsible for much of my success in life, academically and otherwise.

# Table of Contents

Abstract.....	ii
Co-Authorship Statement.....	iv
Acknowledgments.....	v
Table of Contents.....	vi
List of Tables.....	xi
List of Figures.....	xii
List of Appendices.....	xiii
List of Abbreviations and Symbols.....	xiv
1 Introduction.....	1
1.1 Multiple Sclerosis.....	1
1.1.1 Natural history.....	1
1.1.2 Magnetic resonance imaging for MS.....	3
1.1.3 Pathology.....	5
1.1.4 Iron in MS.....	8
1.1.5 Small veins in MS.....	10
1.2 Gradient Echo Imaging.....	12
1.2.1 Gradient echo signal: Magnitude.....	12
1.2.2 Gradient echo signal: Phase.....	13
1.2.3 Blood oxygenation level dependent (BOLD) effect.....	16
1.2.4 Susceptibility weighted imaging (SWI).....	17
1.2.5 Multi-echo gradient echo and $R_2^*$ relaxometry.....	20
1.3 Venous Drainage of the CNS.....	21
1.3.1 Normal drainage of the CNS.....	22
1.3.2 Chronic cerebrospinal venous insufficiency (CCSVI).....	25

1.4	In This Thesis .....	28
1.4.1	Specific Aim 1: Multi-echo SWI.....	29
1.4.2	Specific Aim 2: Time of flight MRV reproducibility .....	30
1.4.3	Specific Aim 3: Study of iron in clinically isolated syndromes .....	30
1.4.4	Specific Aim 4: Imaging central veins in MS lesions .....	31
1.5	References .....	32
2	Comparison of multi-echo post-processing schemes for susceptibility weighted imaging with use of linear and non-linear mask functions .....	48
2.1	Introduction .....	48
2.2	Methods .....	50
2.2.1	SWI post-processing schemes .....	50
2.2.2	SWI mask functions .....	51
2.2.3	MR imaging.....	52
2.2.4	Numerical optimization .....	53
2.2.5	Visual optimization .....	55
2.2.6	Measurements of $R_2^*$ .....	56
2.2.7	ROI analyses.....	56
2.2.8	Visual comparison .....	57
2.3	Results .....	58
2.3.1	Optimization of $m$ .....	58
2.3.2	In vivo data .....	61
2.3.3	ROI analyses.....	61
2.3.4	Visual comparison .....	64
2.3.5	$R_2^*$ measurements.....	64
2.4	Discussion.....	68

2.4.1	SWI optimization.....	68
2.4.2	In vivo data .....	69
2.4.3	$R_2^*$ measurements.....	70
2.4.4	Field inhomogeneity artifacts .....	71
2.4.5	Prospective applications .....	71
2.5	Conclusion .....	72
2.6	References .....	73
3	Metrics of internal jugular vein anatomy obtainable from time of flight magnetic resonance venography: Applicability to chronic cerebrospinal venous insufficiency .	75
3.1	Introduction .....	75
3.2	Methods .....	76
3.2.1	MR imaging.....	76
3.2.2	Measurements of CSA.....	77
3.2.3	Statistical analyses.....	78
3.3	Results .....	78
3.4	Discussion.....	81
3.5	Conclusion.....	84
3.6	References .....	85
4	Increased deep grey matter iron is present in clinically isolated syndromes.....	87
4.1	Introduction .....	87
4.2	Materials and Methods .....	89
4.2.1	Subject recruitment.....	89
4.2.2	MR imaging.....	90
4.2.3	Multi-echo gradient echo processing.....	90
4.2.4	Measurements of CSA.....	91
4.2.5	Lesion segmentation.....	92

4.2.6	Image-based general linear model (GLM) analysis .....	92
4.2.7	Lesion $R_2^*$ analyses .....	94
4.3	Results .....	94
4.3.1	$R_2^*$ depends on age in the cortex, putamen, edge of lateral ventricles .....	94
4.3.2	In patients, $R_2^*$ is decreased in normal appearing white matter (NAWM) and increased in deep grey matter and cortical areas.....	94
4.3.3	Mean CSA of the right IJV is reduced in patients compared to controls ..	96
4.3.4	Correlations of $R_2^*$ differences with clinical and imaging parameters.....	99
4.3.5	Baseline $R_2^*$ levels do not differ between MS and unconverted CIS.....	99
4.3.6	Lesion $R_2^*$ has no association with IJV CSA .....	99
4.4	Discussion.....	102
4.5	Conclusion .....	107
4.6	References .....	108
5	Central veins in white matter hyperintensities can be detected at 3 T and may be predictive of an MS diagnosis .....	111
5.1	Introduction .....	111
5.2	Methods .....	112
5.2.1	Subject recruitment.....	112
5.2.2	MR imaging.....	113
5.2.3	Image processing .....	113
5.2.4	Image analysis .....	114
5.2.5	Statistical evaluation.....	116
5.3	Results .....	117
5.4	Discussion.....	121
5.5	Conclusion .....	124
5.6	References .....	125

6 Conclusion .....	127
6.1 Thesis Summary and Discussion.....	127
6.2 Future Work.....	133
6.2.1 Longitudinal study of deep grey matter iron .....	134
6.2.2 Longitudinal study of lesion iron and microstructure .....	134
6.2.3 Study of venocentricity of white matter lesions .....	136
6.2.4 Longitudinal study of IJV caliber.....	138
6.3 In closing .....	138
6.4 References .....	139
Appendix A: Ethics approval notice.....	142
Appendix B: Ethics revision approval notice.....	143
Appendix C: Copyright release of material in Chapter 2 .....	144
Appendix D: Copyright release of material in Chapter 4.....	145
CURRICULUM VITAE .....	150

## List of Tables

Table 2.1 Optimization of $m$ .....	60
Table 2.2 $R_2^*$ measurements.....	67
Table 3.1 Summary of IJV CSA metrics and reproducibility. ....	80
Table 4.1 Cohort demographics .....	89
Table 4.2 Mean cross-sectional areas of internal jugular veins.....	97
Table 4.3 Mean $R_2^*$ and correlations in various ROIs .....	100
Table 5.1 Contingency table of WMH counts in healthy controls and patients.....	119



## List of Figures

Figure 1.1 SWI processing .....	18
Figure 1.2 Sagittal venogram of major intracranial veins. ....	23
Figure 1.3 Coronal venogram of major cervical veins. ....	26
Figure 2.1 CNR versus number of mask multiplications .....	59
Figure 2.2 Minimum intensity projections for different SWI schemes.....	62
Figure 2.3 CNR for various structures. ....	63
Figure 2.4 Mean ranks of visibility. ....	65
Figure 2.5 Mean rank of artifact severity at sinuses.....	66
Figure 3.1 Representative time of flight venogram.....	79
Figure 4.1 Representative results from voxel-wise age-adjusted t-tests .....	95
Figure 4.2 Bland-Altman plot of total IJV CSA.....	98
Figure 4.3 Mean $R_2^*$ at <i>baseline</i> for healthy controls, CIS patients, and MS patients.....	101
Figure 5.1 Multi-echo SWI images before and after correction with $S_0$ .....	115
Figure 5.2 FLAIR and multi-echo SWI of a venocentric and non-venocentric WMH...	118
Figure 5.3 %LCV for different study groups .....	120

## List of Appendices

Appendix A: Ethics approval notice.....	142
Appendix B: Ethics revision approval notice.....	143
Appendix C: Copyright release of material in Chapter 2.....	144
Appendix D: Copyright release of material in Chapter 4.....	145

## List of Abbreviations and Symbols

<b>Abbreviation</b>	<b>Definition</b>
$\Delta B$	magnetic field shift
$B_{local}$	local magnetic field
$B_{background}$	background magnetic field
$f$	SWI mask function
$H$	Hann mask function
$L$	linear mask function
$m$	mask multiplication power
$R_2$	transverse relaxation rate
$R'_2$	effective transverse relaxation rate - reversible component
$R_2^*$	effective transverse relaxation rate
$S$	magnitude
$S_0$	steady state magnitude
$T_1$	longitudinal relaxation time
$T_2$	transverse relaxation time
$T'_2$	effective transverse relaxation time - reversible component
$T_2^*$	effective transverse relaxation time
$TE$	echo time
$TR$	repetition time
$X$	phase or frequency constant
$x$	phase or frequency
$\phi$	phase
$\gamma$	gyromagnetic ratio
$\Delta\omega$	frequency shift
%LCV	percentage of lesions with central veins
BOLD	blood oxygenation level dependent
BW	bandwidth
C1	first cervical vertebra
CDMS	clinically definite multiple sclerosis
CCSVI	chronic cerebrospinal venous insufficiency
CIS	clinically isolated syndrome
CNR	contrast to noise ratio
CNS	central nervous system
CSA	cross sectional area
CSF	cerebrospinal fluid
CV	coefficient of variation
DIS	dissemination in space
DIT	dissemination in time
EDSS	extended disability status scale
FLAIR	fluid attenuated inversion recovery

GP	globus pallidus
GRAPPA	generalized autocalibrating partially parallel acquisitions
GRE	gradient recalled echo
IJV	internal jugular vein
mIP	minimum intensity projection
MPRAGE	magnetization prepared acquisition of gradient echo
MRI	magnetic resonance imaging
MRV	magnetic resonance venography
MS	multiple sclerosis
NAWM	normal appearing white matter
OR	optic radiations
PPMS	primary progressive multiple sclerosis
RF	radiofrequency
rms	root mean square
RN	red nucleus
ROI	region of interest
RRMS	relapsing remitting multiple sclerosis
SD	standard deviation
SNR	signal to noise ratio
SPMS	secondary progressive multiple sclerosis
STN	subthalamic nucleus
SWI	susceptibility weighted imaging
T1w	T1 weighted imaging
TA	acquisition time
TOF	time of flight
QSM	quantitative susceptibility mapping
WM	white matter
WMH	white matter hyperintensity

# 1 Introduction

This thesis is concerned with the development and application of magnetic resonance imaging (MRI) techniques for the study of pathological components in early multiple sclerosis (MS) including iron accumulation and a role for veins. This chapter will provide the background and rationale for imaging studies described in this thesis. First, a summary of natural history, imaging, and pathology of MS is presented. Second, relevant details of MRI techniques employed herein are provided, culminating in a description of susceptibility weighted imaging and  $R_2^*$  relaxometry. Third, in order to address a recent theory of MS pathogenesis, normal drainage of blood from the central nervous system (CNS) and chronic cerebrospinal venous insufficiency (CCSVI) are discussed. Finally, this chapter concludes with a brief overview of subsequent chapters of this thesis.

## 1.1 Multiple Sclerosis

### 1.1.1 Natural history

Multiple sclerosis (MS) is the most prevalent neurological disease that affects young adults in Canada, with roughly 55,000 to 75,000 individuals affected<sup>1</sup>. Prevalence varies by region, but MS affects approximately 88 per 100,000 individuals in London, Ontario, and 85 per 100,000 in surrounding Middlesex County<sup>2</sup>. MS affects more than twice as many women as it does men<sup>3</sup>, an unexplained bias. Curiously, this ratio has been steadily increasing since the early 20<sup>th</sup> century, also for unknown reasons; this is potentially

related to environmental or gene-environment contributions. MS affects primarily Caucasians of Northern European ancestry<sup>4</sup>.

In 85% of individuals with MS, disease onset is marked by a clinically isolated syndrome (CIS), typically affecting the optic nerves, spine, or brainstem<sup>5</sup>. In brief, a CIS is an acute or sub-acute episode of neurological disturbance due to a single white matter lesion; this *may* be the first evidence of MS, although further studies are required to confirm or exclude MS as the diagnosis. A brief summary of common differential diagnoses for MS is provided below. In general, 30-70% of patients presenting with a CIS will eventually be diagnosed with clinically definite MS (CDMS)<sup>6</sup>. In 80-90% of patients with MS, disease course is initially marked with relapsing/remitting symptoms – so called relapsing remitting MS (RRMS)<sup>4</sup>. In these patients, disease onset is usually in the third or fourth decade of life. The interval between relapses is random, but early in the disease course relapses typically occur once a year, decreasing in frequency with time. Eventually, the disease is marked by a steady worsening of symptoms that occurs independently of relapses. At this stage, the disease is called secondary progressive MS (SPMS)<sup>7</sup>. In one study, median time to SPMS from diagnosis of RRMS was 21.4 years, occurring at a median age of 53.7 years<sup>8</sup>.

In the remaining 10-20% of patients, the disease is characterized by steady progression of symptoms in the absence of relapses from onset<sup>9</sup>. This disease is termed primary progressive MS (PPMS) and generally carries the worst prognosis<sup>10</sup>. Although immunomodulatory drugs can reduce the frequency and severity of relapses in RRMS,

they are of no benefit for progressive symptoms. Onset of PPMS is generally during the fourth or fifth decade.

In about one quarter of patients, MS never affects activities of daily living; alternatively, 15% of patients become severely disabled within a short time<sup>4</sup>.

### 1.1.2 Magnetic resonance imaging for MS

MRI has an intimate role in the diagnosis of MS, where it is used to establish that the disease shows dissemination in space (DIS) as well as dissemination in time (DIT)<sup>11</sup>. Moreover, MRI can be used to evaluate and exclude many typical differential diagnoses in patients with MS-like presentations<sup>12</sup>. Current diagnostic criteria rely on MRI to visualize white matter lesions in different regions of the brain and spinal cord. Based on MRI findings, DIS can be demonstrated with one or more T2 lesions (i.e. a lesion with hyperintense signal on T2-weighted images) in at least two of four white matter areas: periventricular, juxtacortical, infratentorial, and spinal cord (however, symptomatic brainstem and cord lesions are excluded from lesion counts). DIT can be demonstrated by a new T2 or contrast-enhancing lesion (i.e. a lesion with hyperintense signal on T1-weighted images following intravenous injection of a contrast agent) on a follow-up MRI, or the simultaneous presence of asymptomatic contrast-enhancing and non-enhancing lesions at any time.

As noted above, the exclusion of other neurological disorders is an essential step when considering an MS diagnosis<sup>12</sup>. In general, there is a long list of diseases that share

radiological similarities with MS largely owing to the relatively limited specificity of abnormalities visualized by clinical MRI images (namely, hyperintense foci on T2 weighted images). How MRI may be used to vet a list of possible diagnoses is beyond the scope of this thesis (this information is available elsewhere<sup>13</sup>). Inflammatory demyelinating diseases that may challenge the differential diagnosis include atypical presentations of MS (acute presentations, Balo's sclerosis, tumefactive disease), acute disseminate encephalomyelitis, and neuromyelitis optica. The extensive list of diseases with similar MRI findings as MS despite distinct underlying pathologies includes vascular, metabolic, and neurodegenerative disorders. Additionally, many rheumatic diseases (Lupus, Sjögren's syndrome, Behçet's syndrome) may have neurological presentations<sup>14</sup> and MRI findings which can be challenging to differentiate from MS.

MRI-based criteria for MS diagnosis have been proposed and revised several times since 2001<sup>11,15-17</sup>, with a trend towards becoming simpler to use and less reliant on the use of a contrast agent. In addition to being an invasive and potentially uncomfortable procedure, intravenous administration of contrast agent holds a small risk of severe allergic reaction<sup>18</sup>. Revisions to diagnostic criteria have maintained a relatively high specificity to CDMS of approximately 90%, but sensitivity remains modest, at best. One study estimated sensitivity of the new criteria to CDMS to be at 72%<sup>19</sup> (in other words, there was a tendency to under-diagnose/miss cases of MS). In that study, diagnosis with CDMS took a median of 8 months from clinical presentation, and in some individuals



diagnosis may take years<sup>20</sup>. Clearly, the ideal criteria would facilitate high specificity, high sensitivity diagnosis to be made at first presentation.

The current diagnostic criteria do not indicate what MRI field strength is appropriate for these studies<sup>11</sup>; however, the criteria are generally based on the most common clinical strength of 1.5 T. As higher field strength scanners become more prevalent, extension of these criteria to different field strengths is imperative. It is clear from several studies that inflammatory white matter lesions are increasingly visible at higher field. One estimate suggests a 40% increase in the number of lesions detected at 3 T compared to 1.5 T<sup>21</sup>, although it is unclear how this will affect diagnosis and prognosis for patients<sup>22,23</sup>.

MRI contrasts (meaning image contrasts achieved by different acquisition methods) that are typically used in the clinic (generally at 1.5 T) do not visualize all damage to neurological tissues in MS, and therefore do not provide a complete assessment of disease burden. Non-conventional MR techniques (i.e. not yet used in a clinical setting) allow evaluation of diffuse changes to normal appearing white matter<sup>24</sup>, lesions in grey matter<sup>25</sup>, as well as iron accumulation<sup>26</sup>. It remains to be seen how these novel techniques can be used to complement existing diagnostic criteria. Ultimately, advanced MRI methods may provide better assessment of risk of conversion from CIS to MS<sup>27</sup>.

### 1.1.3 Pathology

MS is generally held to be a chronic autoimmune disorder of the CNS<sup>28,29</sup>. Manifestation of the disease arises from interactions between inherited predisposition<sup>30</sup> and

environmental factors<sup>31</sup>. The most familiar pathology of MS, and that from which the disease takes its name, is the demyelinating plaque or lesion of the white matter. Characteristically positioned along small veins<sup>32</sup>, white matter plaques in MS are by definition disseminated throughout the CNS.

Early in the lifetime of a lesion (i.e. when the lesion is referred to as an active plaque), adhesion molecules on the endothelial surface of a post-capillary venule interact with mononuclear cells (T cells, B cells, and macrophages) to facilitate the invasion of these cells from the circulation into the CNS parenchyma through the blood brain barrier<sup>33</sup>. Activated autoreactive T cells (i.e. that recognize one or more neuro self-antigens) produce cytokines that mediate the inflammatory environment and may cause direct injury to oligodendrocytes and myelin. Activated B cells also secrete cytokines and produce demyelinating antibodies<sup>34</sup>. Macrophages may adopt a pro-inflammatory phenotype: this appears to be associated with, and potentially induced by, high iron uptake<sup>35</sup>. Alternatively, macrophages may adopt an anti-inflammatory phenotype involving phagocytosis/clearance of myelin debris, which is necessary for remyelination of denuded axons<sup>36</sup>. Additionally, active plaques are characterized by edema, apoptosis of oligodendrocytes<sup>37</sup>, and the presence of reactive microglia<sup>38</sup>. There is considerable heterogeneity in the pathology of white matter lesions as well: Lucchinetti et al.<sup>39</sup> have characterized four fundamentally different types of demyelination from large pathology studies. Type I lesions demonstrate primarily T cell mediated demyelination. Type II lesions also show T cell mediated damage, in addition to antibody-mediated changes.

Both Type III and IV lesions show extensive damage to and loss of oligodendrocytes, with Type IV lesions being found exclusively in PPMS.

Alternatively, chronic plaques in MS are distinguished by diminished/absent inflammation<sup>40</sup>, relative lack of reactive glia, astrocytic scarring<sup>41</sup>, and myelin-laden macrophages typically found at the rim of the lesion<sup>35</sup>. Remyelination is the reparative process by which denuded axons are invested with new myelin sheaths. Remyelination may be present in chronic lesions, but is typically only located to the outer rim of the lesion<sup>42</sup>. Axonal transection and degeneration occur not only within the active lesion, but also in the chronic lesion<sup>43</sup> where the lack of trophic factors provided by myelin is postulated to be responsible for axonal loss<sup>44</sup>.

It has become increasingly apparent that damage to neurological tissues in multiple sclerosis extends beyond white matter. Demyelinating lesions are found in as much as 25-30% of the grey matter, as opposed to 5-15% of white matter<sup>45</sup>. Atrophy has been reported in both grey and white matter of MS patients, although grey matter atrophy appears to correlate better with disease disability than measures of white matter<sup>46,47</sup>. Over the past three decades, iron accumulation has been consistently reported in regions of the brain affected by multiple sclerosis<sup>26</sup>, although its role is, as of yet, unclear. Moreover, the close association of MS plaques and cerebral veins, noted from the earliest descriptions of the disease<sup>32</sup>, remains incompletely explained and may be central to the evolution of the plaque and the disease. These two findings – increased iron and

association of pathology with cerebral veins – form the central motivation for this thesis and will be discussed respectively below.

#### 1.1.4 Iron in MS

Neurological tissues normally contain high concentrations of iron<sup>48</sup>. In white matter, many components of the enzymatic machinery required for myelin synthesis and maintenance require iron as a catalytic center. As such, the normally high levels of intracellular iron, generally stored in ferritin, are unsurprising. The oft-cited calorimetry study of Hallgren and Sourander established that iron accumulates with age in cortical grey matter and, at a greater rate, in deep grey matter structures in the normal brain<sup>49</sup>.

Dysregulation of iron homeostasis is a feature of several neurological conditions, including Alzheimer<sup>50</sup> and Parkinson's<sup>51</sup> diseases. Starting in the early 1980's, a series of histological studies suggested abnormal iron accumulation might occur in MS as well. The study of Craelius et al. demonstrated the presence of iron reactivity surrounding MS lesions and associated with nearby blood vessels<sup>52</sup>. Adams found evidence of increased iron storage protein haemosiderin within the vein wall in MS lesions consistent with previous microhemorrhage, and concluded that the cerebral vein wall in MS is subject to extensive inflammatory damage<sup>53</sup>. Using a highly sensitive iron-staining technique, Levine et al. demonstrated increased iron in reactive microglia, amoeboid microglia, macrophages, oligodendrocytes, and myelin within MS lesions<sup>50</sup>, which may suggest an underlying iron metabolism disorder. The specific mechanism of iron accumulation in

MS remains unknown. Serum levels of transferrin receptor (whose ligand is the iron-binding protein transferrin) are increased in MS patients<sup>54</sup>; iron in this form can be transported across the blood brain barrier and released as elemental iron into the brain interstitial fluid<sup>55</sup>. Alterations in brain iron levels may be a downstream effect of an autoimmune response<sup>56</sup>; alternatively, iron may provoke inflammation directly<sup>35</sup>. In either case, iron might serve as a source of oxidative stress<sup>57</sup> (to which lipid-rich tissue, such as myelin, is especially susceptible<sup>58</sup>), thus increasing tissue damage.

In passing, it is interesting that iron and its homeostasis are major factors involved in inflammation in settings outside the CNS, where iron levels correlate with markers of chronic inflammation<sup>59</sup>. Notably, in rheumatic diseases, ferritin levels predict disease activity<sup>60</sup>, and removal of iron is associated with improved clinical outcomes<sup>61</sup>.

Owing to its high sensitivity to iron, MRI was utilized in several early studies of iron in MS, especially with respect to deep grey matter iron where it continues to be a preferred tool for such work. Drayer was the first to interpret decreased signal intensity on T2-weighted images of MS patients in several deep grey matter structures as increased iron<sup>62</sup>. Increased iron in basal ganglia structures has since been confirmed by numerous MRI studies using T2 hypointensity<sup>63</sup>, relaxation rate<sup>64</sup>, phase<sup>65</sup>, and magnetic field correlation<sup>66</sup>. The significance of deep grey matter iron is unknown in MS, although it may cause cellular damage<sup>57</sup> and thus contribute to clinical disability<sup>67</sup>.

As these studies tend to have been performed cross-sectionally in time on patients with CDMS, they have not established (i) at what stage of the disease iron accumulation

occurs (both within lesions and in deep grey matter), or (ii) whether iron is a primarily a cause or consequence of pathology. At least two recent studies have interrogated iron levels in deep grey matter or patients with CIS (a subset of who presumably will be diagnosed with MS), working under the hypothesis that, if iron is a cause of MS, it should be present at first clinical presentations. However, these studies have found contradictory results, with one reporting iron is increased in patients with a CIS<sup>68</sup>, and the other finding no such difference<sup>67</sup>. These contrasting results are likely related to methodological differences in iron concentration measurements or age of CIS patients as described more thoroughly in the Discussion in Chapter 4.

### 1.1.5 Small veins in MS

An anatomical association of MS lesions and small veins has been known for over a century, although pathological consequences of this association remain unclear. In 1868, Charcot reported that sclerotic plaques of MS were typically positioned along small veins, as determined from analyses of autopsy specimens<sup>32</sup>. In 1916, Dawson described lesions of MS that spread along prominent periventricular veins<sup>69</sup>. Today, such lesions are known to be very typical for MS and are known as Dawson's fingers<sup>70</sup>. In 1963, Fog reported on 30 MS plaques from cadaver brains, stating such lesions typically followed the course of small veins<sup>71</sup>.

Functionally, the central venule within a lesion is directly involved in the lesion's pathogenesis. Breakdown of the blood brain barrier precedes symptoms and other MRI

signs of a new lesion<sup>72</sup>. In the acute lesion<sup>40,53</sup>, perivenous inflammation and cuffing of the vascular wall are present and are associated with infiltration of mononuclear cells, demyelination, and axonal damage. In chronic lesions, evidence of long-standing vascular injury includes thickening or hyalinization of the vein wall, in addition to signs of previous microhemorrhage<sup>73</sup>.

More recently, MRI has been used to demonstrate the presence of a central venule in many MS plaques<sup>72,74</sup>. Recent studies have proposed that the presence of a central vein within white matter T2 hyperintensities may be specific to MS, and this specificity could be exploited for the benefit of diagnosis<sup>75,76</sup>.

Over the past century, various theories have been put forth that attribute the origins of MS pathology to venous occlusion or reflux in (relatively large) intra- or extra-cranial vessels resulting in microhemorrhage including pathological iron deposition upstream (putatively at the position of a subsequent lesion)<sup>77</sup>. In such a model, iron is a driving factor for inflammation and subsequent antigen presentation. While these theories might initially appeal to logic inasmuch as an association of demyelinating foci with small veins and iron is known, they have been insufficient with respect to objective evidence or scientific support. However, evidence is more supportive of increased iron in MS as secondary to an autoimmune response that is associated with (1) increased transport of iron into the brain from circulation<sup>54</sup>, and/or, (2) irregular metabolism of iron<sup>56</sup>. In these cases, a subsequent toxic<sup>57</sup> or pro-inflammatory role<sup>35</sup> for increased iron cannot yet be ruled out.

## 1.2 Gradient Echo Imaging

Gradient echo imaging forms the foundation of many applications on modern magnetic resonance imaging (MRI) systems<sup>78</sup>. Gradient echo imaging has found many practical applications where rapid imaging with low power deposition is required<sup>79</sup>, including dynamic cardiac imaging, MR angiography, perfusion imaging, and functional MR studies. The gradient echo acquisition represents the most basic MRI experiment: after excitation of spins in the imaging volume with a radio-frequency (RF) pulse, a readout gradient is applied and the signal is sampled<sup>80</sup>. Gradient echo sequences form the basis for much of the imaging work described in this thesis.

### 1.2.1 Gradient echo signal: Magnitude

After RF excitation, transverse magnetization (i.e. which generates signal) will decrease in magnitude with time, due to thermodynamic effects. This process is called transverse relaxation, and is characterized by an exponential rate of  $R_2$ , or its inverse, the decay time constant  $T_2$ <sup>81</sup>.  $R_2$  is inversely proportional to water concentration.  $R_2$  will also increase in the presence of iron. Variations in magnetic field within the imaging voxel cause spins to precess at a range of frequencies resulting in dephasing, or loss of coherence. In gradient echo imaging, this dephasing is not reversed. Therefore, the measured magnitude of the vector sum of these spins is reduced compared to what is expected due to  $T_2$  decay alone. This additional field-induced decay is characterized by rate  $R_2'$ , or its inverse, the decay time constant  $T_2'$ <sup>79</sup>.  $R_2'$  is dependent on the sample and machine, and will increase with



increasing iron concentrations in the imaging volume. The effective transverse relaxation of magnetization magnitude occurs due to both thermodynamic ( $R_2$ ) and field-induced ( $R'_2$ ) effects, and is characterized by a rate  $R_2^*$  (Eq. 1.1), or equivalently, its inverse, the relaxation time  $T_2^*$  (Eq. 1.2).

$$R_2^* = R_2 + R'_2 \quad [1.1]$$

$$\frac{1}{T_2^*} = \frac{1}{T_2} + \frac{1}{T'_2} \quad [1.2]$$

The magnitude ( $S$ ) of gradient echo signal therefore depends on the effective transverse relaxation rate, in addition to the time at which the signal is sampled (i.e. the echo time,  $TE$ ), and the steady state signal ( $S_0$ ), as described in Eq. 1.3.

$$S(TE) = S_0 \exp(TE \cdot R_2^*) \quad [1.3]$$

### 1.2.2 Gradient echo signal: Phase

Magnetization, which gives rise to MR signal, is a vector, having both magnitude and phase. Once magnetization is excited into the transverse plane, it precesses about the magnetic field at a frequency that is linearly related to magnetic field; equivalently, frequency offset ( $\Delta\omega$ ) from resonance is proportional to the shift ( $\Delta B$ ) from the main magnetic field as in Eq. 1.4, where the constant of proportionality ( $\gamma$ ) is the gyromagnetic ratio.

$$\Delta\omega = \gamma\Delta B \quad [1.4]$$

The phase ( $\phi$ ) of magnetization represents the difference in phase accrued by some time ( $TE$ ) compared to on-resonance spins (i.e. those spins where  $\Delta\omega=0$ ), as in Eq. 1.5a; or, after considering the relationship presented in Eq. 1.4, as in 1.5b.

$$\phi(TE) = \Delta\omega \cdot TE \quad [1.5a]$$

$$\phi(TE) = \gamma\Delta B \cdot TE \quad [1.5b]$$

The phase of the signal measured for a given voxel is the phase of the vector sum of all magnetizations within the voxel. In reality, there will be a range of magnetic fields within the voxel; in other words, it would be inappropriate to assume a single value of  $\Delta B$  for the entire voxel. The interpretation of voxel phase is further complicated by the fact that a range of transverse relaxation times within a voxel will cause magnetizations to contribute differentially to measured phase, especially at increasing TEs. The measured phase of a voxel can be considered related to an average  $\Delta B$  within the voxel, weighted towards positions within the voxel with the largest magnetization at the  $TE$ .

The distribution of magnetic susceptibilities within the imaging volume of interest, for example the brain, gives rise to changes in ‘local’ (ideally, microscopic and mesoscopic) magnetic field ( $B_{\text{local}}$ )<sup>82</sup>. However, inhomogeneities in the main magnetic field and abrupt magnetic susceptibility interfaces (for example, at the sinuses) result in a so-called ‘background’ field ( $B_{\text{background}}$ ). Any deviation from the main field  $\Delta B$ , to which magnetization phase is proportional (Eq. 1.5b), is thus the superposition of deviations due to local and background effects<sup>83</sup>, as in Eq. 1.6.

$$\Delta B = \Delta B_{local} + \Delta B_{background} \quad [1.6]$$

Background contributions are generally undesirable and efforts are made to remove them from the phase image before further processing. The background field tends to vary slowly over the image; therefore its effects on phase can be removed with spatial high-pass filtering. A number of such techniques have been proposed to remove these unwanted contributions from phase, including heuristic approaches (homodyne filtering<sup>84</sup>, fitting of high order polynomials<sup>85</sup>) and application of physical models (dipole fitting<sup>86</sup>, SHARP filtering<sup>87</sup>). In reality, the classification of field shifts into ‘local’ and ‘background’ is quite arbitrary and in many cases, appears to be retrospectively defined: those contributions which can be removed with by the implemented spatial filter are deemed ‘background,’ and everything else, ‘local.’

In clinical practice, phase data are nearly always discarded, with exceptions limited to phase contrast angiography<sup>88</sup>, where phase is sensitized to flow speed by application of magnetic field gradients. In research settings, phase contrast has been exploited for an increasing number of applications in recent years, including calculation of quantitative susceptibility maps<sup>89</sup>, measurement of cerebral metabolic rate of oxygen<sup>90</sup>, and measurement of iron concentrations<sup>91</sup>. Due to field shifts that arise in the presence of deoxygenated blood, phase plays a crucial role in susceptibility weighted imaging, as described below.

Ultimately, both phase and  $R_2^*$  (and thus magnitude, as in Eq. 1.3) are dependent on the distribution of magnetic field within the imaging volume. Differences in phase are related

to differences in  $\Delta B$  *between* voxels. Differences in magnitude may be attributed to differences in  $\Delta B$  experienced by magnetization *within* voxels (i.e. differences in  $R_2'$  between voxels) in addition to differences in  $R_2$ .

### 1.2.3 Blood oxygenation level dependent (BOLD) effect

The BOLD effect represented a major breakthrough in the visualization of capillaries, venules, and veins by using deoxyhemoglobin as an intrinsic contrast agent<sup>92</sup>. In blood, the transverse relaxation times ( $T_2$  and  $T_2^*$ ) are a function of deoxyhemoglobin content and thus of blood oxygenation. As oxygenation increases, deoxyhemoglobin concentration decreases, and the relaxation times – and thus the signal in  $T_2$  or  $T_2^*$  weighted images – will increase.

Early work in animals and humans demonstrated that the BOLD effect could be exploited to image veins, visibility of which was a function of available signal-to-noise ratio, degree of oxygenation, and size of vessel<sup>93</sup>. Shortly thereafter, the BOLD mechanism found use in functional MRI, where the increase in oxygenation that accompanies neural activation results in increase of MRI signal<sup>94</sup>.

The study of Lai et al. was the first to describe efforts to enhance BOLD contrast in gradient echo images to improve visibility of veins<sup>95</sup>. In that study, a commutator filter was described that incorporated information from the complex image into the magnitude image, wherein some venous contrast was present and attributable to the BOLD effect. This formed the basis for MR venography with susceptibility weighted imaging (SWI)

where phase data is used directly to enhance BOLD contrast in magnitude images, as described in the subsequent section.

#### 1.2.4 Susceptibility weighted imaging (SWI)

Extending the work of Lai et al., Reichenbach formally described imaging small veins using the phase image explicitly to enhance magnitude contrast<sup>96</sup>. This technique was originally referred to as BOLD MR venography, however it has since been named susceptibility weighted imaging. At 3 T and with a resolution of  $0.5 \times 0.5 \times 1.0 \text{ mm}^3$ , SWI was estimated to visualize veins with diameters on the order of 100 to 200  $\mu\text{m}$ <sup>97</sup>, which speaks to the remarkable ability of SWI for visualizing small veins.

In SWI processing<sup>83</sup>, the low spatial frequency components of the phase image (putatively those arising from  $\Delta B_{\text{background}}$  in Eq. 1.6) are first removed using homodyne filtering. The resulting filtered phase image is used to create a phase mask. The typical function<sup>98</sup> used to create this mask image is described in Eq. 1.7, and illustrated with Figure 1.1, although other functions are certainly possible. Effectively, this particular function scales negative phases of  $-\pi$  to 0 rad ( $-180^\circ$  to  $0^\circ$ ) linearly from 0 to 1, and sets all positive phase (0 to  $+\pi$  rad, i.e.  $0^\circ$  to  $+180^\circ$ ) to 1.

$$f(\phi) = \begin{cases} \frac{\pi + \phi(x)}{\pi} & \text{if } -\pi \leq \phi < 0 \\ 1 & \text{if } \phi \geq 0 \end{cases} \quad [1.7]$$

Due to paramagnetic deoxyhemoglobin<sup>99</sup>, voxels containing veins typically will have negative phase and thus will be assigned values less than 1 in the phase mask.

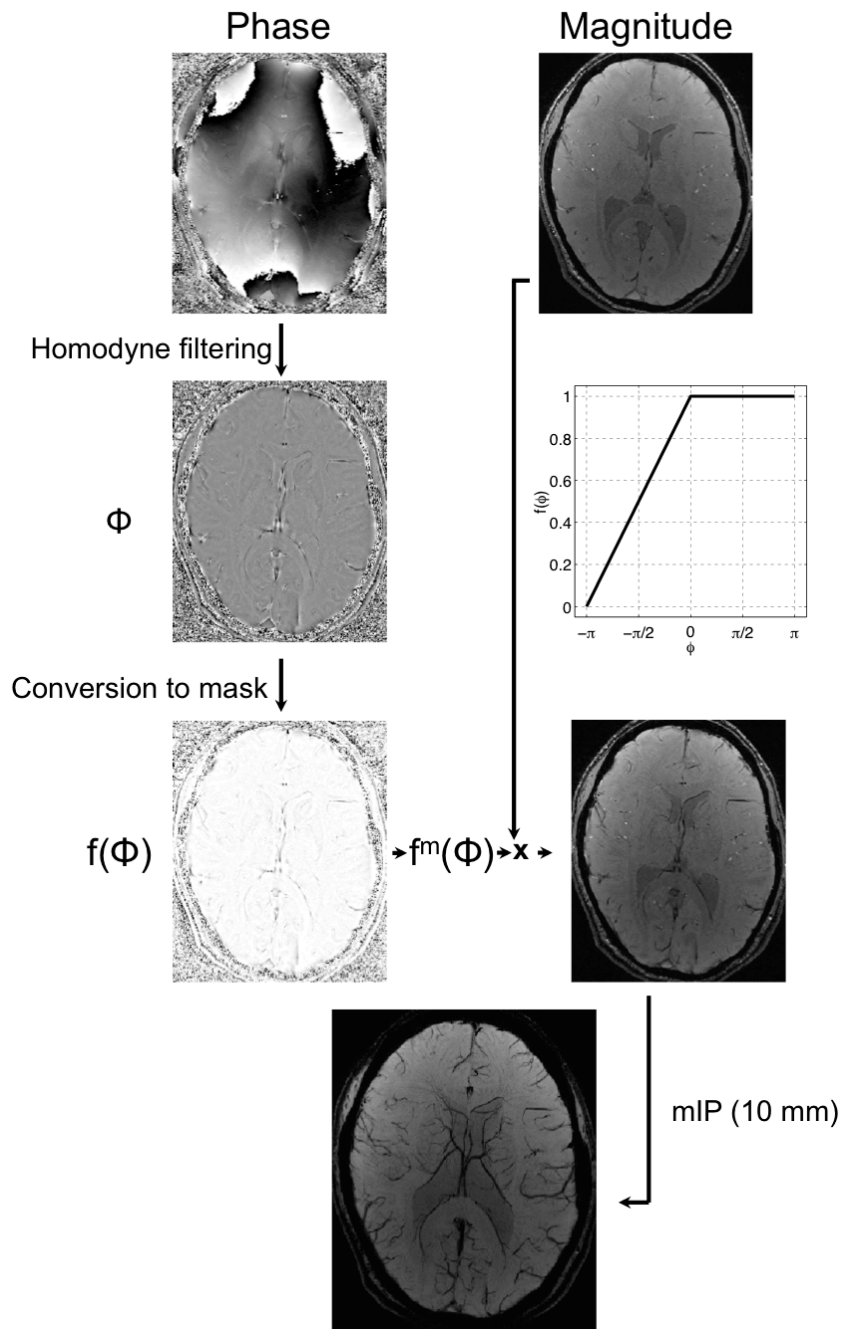


Figure 1.1 SWI processing. Phase and magnitude data are reconstructed. The background field contributions to phase are removed using homodyne filtering. The filtered phase image ( $\Phi$ ) is converted to a mask [ $f(\Phi)$ ], using the plotted function. The  $m^{\text{th}}$  power of the mask is multiplied with the magnitude image. A minimum intensity projection (mIP) over 10 mm is shown, where veins are readily apparent.

By multiplying the phase mask with itself several times, contrast between veins and surrounding tissue can be enhanced. However, while venous contrast can be accentuated by increasing the exponential power of the phase mask, generally referred to as  $m$ , doing so also increases noise, therefore the optimal value of  $m$  must be carefully considered<sup>100</sup>. Multiplication of the  $m^{\text{th}}$  power of the phase mask with the magnitude image (wherein veins may have some contrast already in part due to the BOLD effect) results in enhanced venous contrast, i.e. veins appear darker. If illustrating venous vessel contiguity is the goal of the study, adjacent slices can be viewed as a minimum intensity projection (mIP).

These steps are illustrated in Fig. 1.1.

The technical foundations of SWI processing were well established by the early 2000's and work has continued to optimize acquisition<sup>101</sup> and post-processing parameters<sup>100,102</sup>. One component of the post-processing chain that is very flexible and thus a research target is the mask function. While the linear mask function described above (Eq. 1.7) is the commonest function, other functions have been proposed for specific applications, such as improving contrast of veins for oblique acquisitions<sup>103</sup>, improving contrast of implanted microelectrodes<sup>104</sup>, and kidney imaging<sup>105</sup>.

Since its earliest descriptions as a technique for venography, SWI has found uses in visualizing other tissues in the brain, such as blood products, iron, and calcium. As a result, major clinical applications of SWI are numerous<sup>106</sup> and include investigations for trauma, stroke, cerebral amyloid angiopathy, and tumor grading.

### 1.2.5 Multi-echo gradient echo and $R_2^*$ relaxometry

Extension of gradient echo to multiple acquisitions of signal (i.e. at a series of TEs) after the RF excitation allows multiple contrasts to be acquired in the same sequence. By serially sampling the decay of magnetization, one obtains a dataset from which  $R_2^*$  can be measured for each voxel. The most basic approach to measuring  $R_2^*$  involves fitting the magnitude data from each voxel as a function of TE to the exponential decay function<sup>107</sup> (Eq. 1.3). Phase data can be incorporated into the curve fit in order to eliminate undesirable increases in  $R_2^*$  due to magnetic field inhomogeneity across the voxel<sup>108</sup>, an effect that is more pronounced with increasing voxel size.  $R_2^*$  can also be measured by summing measurements of  $R_2$  and  $R_2'$ , although this may require novel pulse sequences<sup>109</sup>.

Each of  $R_2$ ,  $R_2'$ , and  $R_2^*$  has been used in the study of iron in chronic brain disorders<sup>110</sup>, however for the following reasons,  $R_2^*$  appears to be the most widely used. A linear relationship between local iron concentration and  $R_2^*$  has been chemically validated<sup>85</sup>; moreover,  $R_2^*$  images show contrast that correlates well with histological iron stains<sup>111</sup>. Well-known trends in brain iron accumulation with age have been reproduced with  $R_2^*$  mapping<sup>107</sup>.  $R_2^*$  has been used to study brain iron accumulation in chronic brain disorders including multiple sclerosis<sup>67</sup>, Parkinson's<sup>112</sup>, Alzheimer's<sup>113</sup>, essential tremor<sup>114</sup>, and non-specific demyelination<sup>115</sup>. In the brain,  $R_2^*$  is also sensitive to myelin content and has been used to characterize location, direction, and myelination of white matter fiber bundles<sup>116</sup>.  $R_2^*$  mapping in non-brain is also useful for iron studies, such as in the liver<sup>117</sup>



and heart<sup>118</sup>. Like  $R_2$ ,  $R_2^*$  will decrease in the presence of increasing water concentration; and like  $R_2'$ ,  $R_2^*$  will increase in the presence increasing field inhomogeneity, although in the brain, iron and myelin are the major sources of such inhomogeneity.

SWI images and  $R_2^*$  maps contain useful and potentially complementary information regarding the anatomy and quantitation, respectively, of different perturbors in the brain. However, SWI processing involves only a single-echo gradient echo dataset, whereas  $R_2^*$  mapping requires multiple echoes. Multi-echo SWI processing has been proposed in previous studies<sup>103,108</sup> and allows generation of high-quality venograms *in addition to* intrinsically co-registered  $R_2^*$  maps. However, no previous work has identified the optimal method by which a series of echoes can be combined into a single SWI image. This is the focus of Chapter 2 of this thesis.

### 1.3 Venous Drainage of the CNS

Owing largely to the well-established but unexplained association of MS lesions and small veins in the brain, a number of theories have been proposed in the last century that attempt to connect circulatory abnormalities to MS etiology. In the 1930's, Putnam studied obstructed venous flow in the cerebral veins of dogs<sup>119</sup>, and described similarities between resulting symptoms and those experienced by patients with MS. In the late 1970's and 80's, Schelling postulated that venous reflux into the CNS may be associated with MS<sup>120</sup>. In the last decade, a theory proposed by an Italian vascular surgeon suggested a direct link between occlusion of extra-cranial veins, cerebral

microhemorrhages, and iron-mediated inflammation in MS<sup>121</sup>. These theories have been met with substantial scientific evidence to the contrary, but questions still remain. Are venous abnormalities associated with MS? And if so, do they represent an integral component in disease pathogenesis? Is there an association with iron deposition? We attempt to address these issues, in part, in Chapter 4 of this thesis. An overview of the topic is presented here.

### 1.3.1 Normal drainage of the CNS

The vascular system that drains the cerebrum can be divided into two parts: the superficial system and deep cerebral venous system<sup>122</sup>. The superficial system consists of superficial cerebral veins that run along the cortex and receive blood from subcortical white matter and cortical grey matter. These veins empty into dural sinuses, which include the occipital sinus and superior sagittal sinus. These sinuses flow posteriorly and inferiorly and merge at the confluence of the sinuses. The deep cerebral system drains deep white matter and deep grey matter via the internal cerebral veins and the Vein of Rosenthal. The site of drainage of this system is the great vein of Galen, which then empties into the straight sinus<sup>123</sup>. The straight sinus runs posteriorly and joins with the superficial sinuses at the confluence of sinuses. The confluence then bifurcates into the left and right transverse sinuses, through which blood flows anteriorly as these vessels become the left and right sigmoid sinuses. The sigmoid sinuses turn inferiorly as they become confluent with the left and right internal jugular veins (IJVs) at the cranial base. These veins are identified in a time-of-flight magnetic resonance venogram in Figure 1.2.

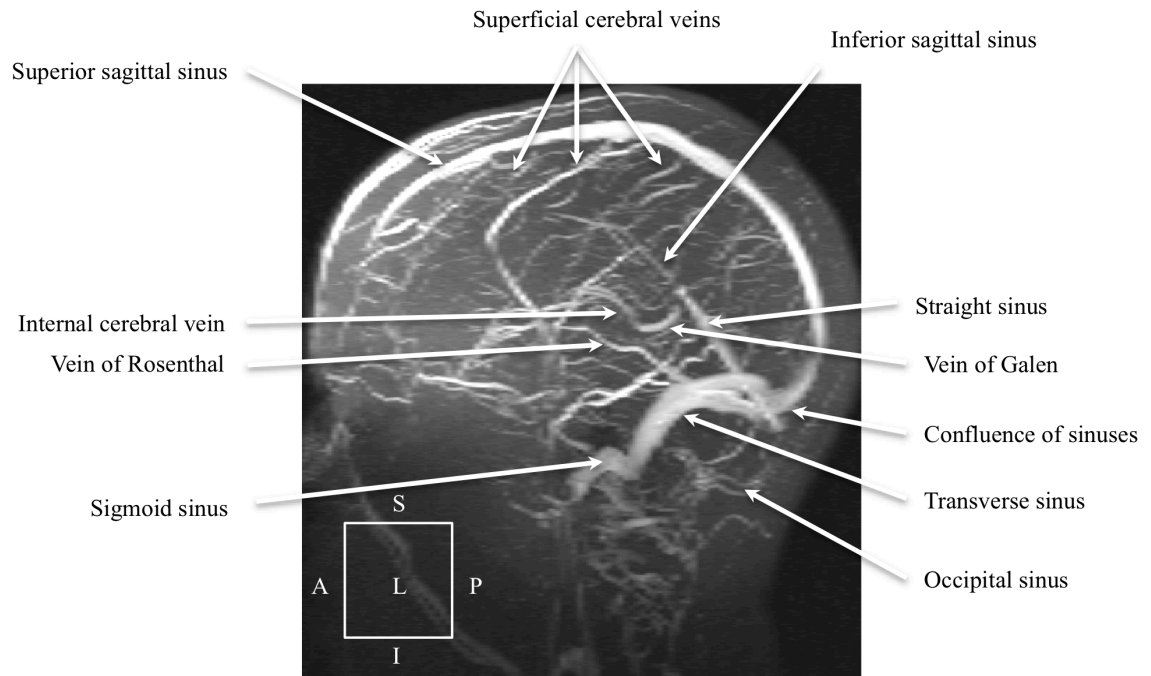


Figure 1.2 Sagittal maximum intensity projection of time of flight magnetic resonance venogram of major intracranial veins. A sinus (more properly, a dural venous sinus) is a venous channel, but unlike a vein, the walls of a sinus are composed of dura mater.

Veins of the cerebellum drain into adjacent sinuses, including the transverse, occipital, and straight sinuses<sup>123</sup>. The veins of the brainstem form a venous plexus (a network or tangle of veins), parts of which may become continuous with spinal veins, or empty into nearby sinuses.

In addition to draining blood from the brain, the IJVs also drain much of the skull and deep parts of the neck and face<sup>122</sup>. Each IJV descends parallel to the ipsilateral carotid artery: at its termination, the IJV joins with the subclavian vein to form the brachiocephalic vein. This vein in turn merges with the contralateral vessel and empties into the superior vena cava. Slightly superior to the IJV termination, the inferior bulb is a dilation of the IJV that is present in most individuals. Superior to the bulb are a pair of valves<sup>124</sup>.

The vertebral vein forms from numerous tributaries of internal venous plexuses within the vertebral canal, which exit the canal at the first cervical vertebra<sup>124</sup>. The vein descends through transverse foramina of the cervical vertebra as a plexus and emerges from the transverse foramen of the sixth cervical vertebra. Subsequently, the vertebral vein empties into the brachiocephalic vein, but also communicates with deep thoracic, lumbar, and intercostal veins. The azygos vein is the final collector for this system, and represents an alternative pathway for blood to return to the right atrium<sup>125</sup>.

In addition to the IJVs, numerous tributaries, which are variable between individuals, may form anastomoses (cross-links) between veins of the neck. As such, the veins of the neck cannot necessarily be entirely separated<sup>122</sup> and it is not possible to define a single

normal anatomy for drainage of the CNS. The main veins of the neck are identified in a magnetic resonance venogram in Figure 1.3.

### 1.3.2 Chronic cerebrospinal venous insufficiency (CCSVI)

An Italian vascular surgeon, Paulo Zamboni, first proposed parallels in the inflammatory environment of MS lesions and ulcers associated with chronic venous disease in 2006, and suggested that a similar pathological substrate – impaired venous drainage – was to blame<sup>121</sup>. Specifically, Zamboni proposed that inflammation in both diseases was iron-dependent. He interpreted reflux during Valsalva maneuver in a patient with MS as evidence of insufficient venous flow, and suggested that such insufficiency might lead to iron deposition and inflammation upstream, i.e. in the CNS.

In subsequent studies, Zamboni interrogated intracranial<sup>126</sup> and extracranial<sup>127</sup> hemodynamics in a larger group of MS patients using ultrasound and selective venography. Five ultrasound-measurable parameters were identified to be typical of a condition Zamboni called CCSVI. A subject in whom two or more parameters were detected was said to have CCSVI. A diagnosis of CCSVI was found to overlap perfectly with a diagnosis of MS<sup>128</sup>. In interpreting this remarkable association, Zamboni suggested that structural abnormalities in the IJVs and azygos vein (which are main outflow routes for venous blood from the brain, as described in section 1.3.1) resulted in venous reflux, increased intracranial pressure, extravasation of red blood cells, and ultimately iron-mediated inflammation.

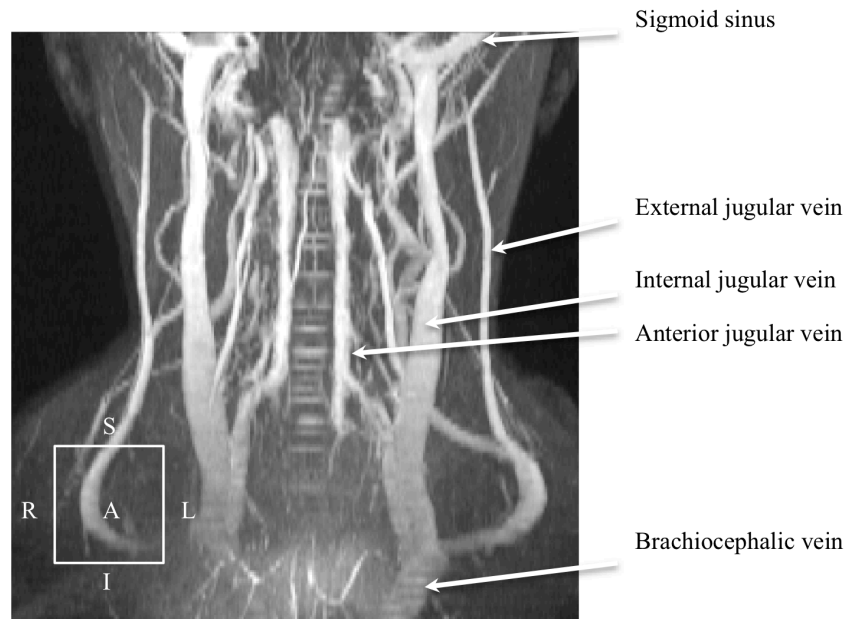


Figure 1.3 Coronal maximum intensity projection of time of flight magnetic resonance venogram of major cervical veins. Vertebral veins are not readily separable from other veins and have not been labeled.

Subsequently, an association between venous abnormalities and MS became the focus of intense scrutiny. Several ultrasound studies failed to reproduce as strong of association between CCSVI and MS as reported initially<sup>129,130</sup>, or failed to detect CCSVI in MS at all<sup>131,132</sup>. In rebuttal, Zamboni claimed this was due to lack of operator training for sonography<sup>133</sup>. Reports of normal intracranial pressure<sup>134</sup> and normal cerebrospinal fluid (CSF) ferritin levels<sup>135</sup> in MS patients were also inconsistent with the CCSVI model. Weinstock-Gutman et al. reported CCSVI in MS patients, however found no relation to clinical disability, raising further questions about the relevance of the CCSVI condition<sup>136</sup>. Indeed, major questions about CCSVI remain unanswered, including whether it exists at all, and if so, if it is associated with MS<sup>137</sup>.

Fueling the controversy surrounding CCSVI, Zamboni reported on an endovascular surgery for CCSVI, describing it to be initially successful at treating extracranial venous stenoses<sup>138</sup>. Reports of positive clinical outcomes in patients were taken with considerable caution given the lack of blinding or control wings in these studies<sup>139</sup>. Enthusiasm for the procedure was increased dramatically by media reports despite the absence of any conclusive evidence that treatment of CCSVI was indicated in MS<sup>140</sup>.

While sonography is the only imaging technique with which CCSVI can be diagnosed (CCSVI is, after all, an *ultrasound-defined* entity)<sup>128,141</sup>, it suffers from several setbacks including a large dependence on operator training. For this reason, and because sonography is foreign to conventional MS studies, a number of research groups have investigated the suitability for magnetic resonance imaging for studying extracranial

veins in patients with MS<sup>142-144</sup>. MRI techniques are less dependent on operator training and allow 3D visualizing of the intra- and extra-cranial vasculature. In general, these studies suggest that time-of-flight (TOF) magnetic resonance venography (MRV) may be a suitable method by which to visualize the internal jugular veins. While the neurological community grows increasingly reluctant to consider a role for CCSVI in MS, recent MRV studies have shown structural abnormalities of the IJVs (such as narrowing or flattening) to be more prevalent in MS patients than healthy controls<sup>143,144</sup>. Such studies have used a subjective or categorical rating scale to classify vessel anatomy. It is our belief that a quantitative measure of vessel caliber would be more useful in such work. The suitability of TOF MRV for quantitative measures of IJV caliber is the focus of Chapter 3 of this thesis, and in Chapter 4, we describe the application of such measurement techniques in patients with CIS.

## 1.4 In This Thesis

This thesis is concerned with work done thus far in an on-going longitudinal MRI study of iron in patients with CIS at high risk of MS diagnosis. Given the unresolved question regarding iron's role as either a cause or consequence of MS, we identify the following as the objective for this thesis: to characterize MRI biomarkers associated with iron deposition in patients with early presentations of MS. Specifically, we identify the following specific aims, each of which is the basis for a subsequent chapter. **Specific Aim 1:** to optimize an MRI post-processing technique to create both cerebral venograms and quantitative images for measuring iron. **Specific Aim 2:** to establish reproducibility



of quantitative measures of IJV caliber, given the proposed (and increasingly tenuous role) for these veins in MS pathogenesis. **Specific Aim 3:** to compare relative levels of iron between CIS patients and healthy controls, in order to determine the spatial distribution of any increased iron present early in the disease. **Specific Aim 4:** to determine if, using techniques developed in this thesis, venules can be detected within lesions in CIS patients. Such venules may be involved in iron deposition<sup>53</sup> and may also have predictive value for subsequent MS diagnosis<sup>145</sup>. Thus, with work proposed here, we are able to investigate a role in early MS for not only iron but additionally veins that drain the CNS - including cerebral venules (about which lesions are centred) and cervical veins, which ostensibly have a role in MS pathogenesis as mediators of iron deposition.

#### 1.4.1 Specific Aim 1: Multi-echo SWI

Multi-echo SWI allows for generation of an image with contrast derived from the distribution of susceptibility within the brain (i.e. a SWI image, useful for visualizing veins), in addition to a quantitative  $R_2^*$  map, the latter being particularly useful for quantifying iron. It has been shown that  $T_2^*$ -weighted magnitude images are sufficient for discrimination of MS plaques from other non-specific lesions in white matter at ultra-high field strengths, based on the presence of a central vein<sup>76</sup>. However, at clinical field strengths the endogenous contrast in the  $T_2^*$ -weighted magnitude is insufficient for this type of analysis<sup>75</sup>. Multi-echo SWI may provide the necessary boost in venous contrast at clinical field strengths to facilitate improved diagnostic specificity based on the presence of a central vein. With this in mind, Chapter 2 of this thesis describes efforts to optimize

multi-echo SWI processing and characterize improvements in the contrast of a number of structures in healthy controls. We also perform measurements of  $R_2^*$  and validate our measurements against previously reported values. Part of this work has been accepted for publication in the American Journal of Neuroradiology. This sequence and post-processing form the methodological foundation for our on-going longitudinal study of CIS patients.

#### 1.4.2 Specific Aim 2: Time of flight MRV reproducibility

As described in Section 1.3.2, an interesting, if not altogether convincing, theory has been proposed that attributes MS pathogenesis to extra-cranial venous pathology resulting in cerebral iron deposition. Most MR studies of CCSVI examine the IJVs with a categorical rating scale<sup>144</sup>, which may in fact be suboptimal. In Chapter 3 of this thesis, we investigate *quantitative* measures of IJV caliber including the cross-sectional area as measured from TOF MRV. Specifically, this chapter is concerned with establishing the inter-scan reproducibility of these metrics in healthy controls.

#### 1.4.3 Specific Aim 3: Study of iron in clinically isolated syndromes

In Chapter 4 of this thesis, we use  $R_2^*$  maps to establish differences in iron between our study's cohort of CIS patients and healthy controls. First, changes in  $R_2^*$  with age are estimated from the normal cohort. Next, the expected normal contributions to aging are removed from  $R_2^*$  datasets for both patients and healthy controls. For each voxel in the brain, statistical testing is used to determine if there are any differences between groups

in age-corrected  $R_2^*$  and thus, potentially iron. For clusters of voxels where significant differences were found, regions of interest are defined. Correlations of the average  $R_2^*$  in each region of interest with additional imaging and clinical measures are investigated in order to explain the observed differences. To assess the predictive value of increased  $R_2^*$  for MS diagnosis, we compare  $R_2^*$  increases between those CIS patients who have been diagnosed with MS since recruitment and those who remain unconverted. Additionally, as a potential explanation for increased iron in MS, we explore the cross-sectional area of the IJVs in both patients and healthy controls using methodology proposed in Chapter 3.

#### 1.4.4 Specific Aim 4: Imaging central veins in MS lesions

It has been proposed that a large fraction of lesions with MRI-detectable penetrating veins in potential MS is predictive of future MS diagnosis; however, questions remain about the practical feasibility of this technique. In Chapter 5 of this thesis, we employ tools proposed in Chapter 2 (multi-echo SWI) to characterize the visibility of veins within white matter hyperintensities (WMHs). Using multi-echo SWI, WMHs in all subjects are rated for the presence of a central vein. The prevalence of veins within WMHs is compared between healthy controls, CIS patients who have not yet converted to MS (after approximately 1 year of follow up), and CIS patients who have converted to MS. Moreover, the predictive value of a high percentage of lesions with central veins for conversion to MS is evaluated on a patient-by-patient basis.

The last chapter of this thesis summarizes the work performed for this thesis and also briefly discusses some prospective analyses to be carried out on study data.

## 1.5 References

1. Poppe AY, Wolfson C, Zhu B. Prevalence of multiple sclerosis in Canada: a systematic review. *Can J Neurol Sci* 2008; **35**:593-601.
2. Hader WJ, Elliot M, Ebers GC. Epidemiology of multiple sclerosis in London and Middlesex County, Ontario, Canada. *Neurology* 1988; **38**:317-321.
3. Ramagopalan SV, Byrnes JK, Orton SM et al. Sex ratio of multiple sclerosis and clinical phenotype. *Eur J Neurol* 2010; **17**:634-637.
4. Compston A, Coles A. Multiple sclerosis. *Lancet* 2002; **359**:1221-1231.
5. Miller D, Barkhof F, Montalban X, Thompson A, Filippi M. Clinically isolated syndromes suggestive of multiple sclerosis, part I: natural history, pathogenesis, diagnosis, and prognosis. *Lancet Neurol* 2005; **4**:281-288.
6. Moraal B, Pohl C, Uitdehaag BM et al. Magnetic resonance imaging predictors of conversion to multiple sclerosis in the BENEFIT study. *Arch Neurol* 2009; **66**:1345-1352.
7. Tremlett H, Yinshan Z, Devonshire V. Natural history of secondary-progressive multiple sclerosis. *Mult Scler* 2008; **14**:314-324.
8. Koch M, Kingwell E, Rieckmann P, Tremlett H. The natural history of secondary progressive multiple sclerosis. *J Neurol Neurosurg Psychiatry* 2010; **81**:1039-1043.
9. Koch M, Kingwell E, Rieckmann P, Tremlett H. The natural history of primary progressive multiple sclerosis. *Neurology* 2009; **73**:1996-2002.

10. Ebers GC. Natural history of primary progressive multiple sclerosis. *Mult Scler* 2004; **10**:8-15.
11. Polman CH, Reingold SC, Banwell B et al. Diagnostic criteria for multiple sclerosis: 2010 revisions to the McDonald criteria. *Ann Neurol* 2011; **69**:292-302.
12. Charil A, Yousry TA, Rovaris M et al. MRI and the diagnosis of multiple sclerosis: expanding the concept of "no better explanation". *Lancet Neurol* 2006; **5**:841-852.
13. Miller DH, Weinshenker BG, Filippi M et al. Differential diagnosis of suspected multiple sclerosis: a consensus approach. *Mult Scler* 2008; **14**:1157-1174.
14. Theodoridou A, Settas L. Demyelination in rheumatic diseases. *Postgrad Med J* 2008; **84**:127-132.
15. McDonald WI, Compston A, Edan G et al. Recommended diagnostic criteria for multiple sclerosis: guidelines from the International Panel on the diagnosis of multiple sclerosis. *Ann Neurol* 2001; **50**:121-127.
16. Polman CH, Reingold SC, Edan G et al. Diagnostic criteria for multiple sclerosis: 2005 revisions to the "McDonald Criteria". *Ann Neurol* 2005; **58**:840-846.
17. Swanton JK, Fernando K, Dalton CM et al. Modification of MRI criteria for multiple sclerosis in patients with clinically isolated syndromes. *J Neurol Neurosurg Psychiatry* 2006; **77**:830-833.
18. Dillman JR, Ellis JH, Cohan RH, Strouse PJ, Jan SC. Frequency and severity of acute allergic-like reactions to gadolinium-containing i.v. contrast media in children and adults. *AJR Am J Roentgenol* 2007; **189**:1533-1538.
19. Swanton JK, Rovira A, Tintore M et al. MRI criteria for multiple sclerosis in patients presenting with clinically isolated syndromes: a multicentre retrospective study. *Lancet Neurol* 2007; **6**:677-686.

20. Brex PA, Ciccarelli O, O'Riordan JI, Sailer M, Thompson AJ, Miller DH. A longitudinal study of abnormalities on MRI and disability from multiple sclerosis. *N Engl J Med* 2002; **346**:158-164.
21. Bachmann R, Reilmann R, Schwindt W, Kugel H, Heindel W, Kramer S. FLAIR imaging for multiple sclerosis: a comparative MR study at 1.5 and 3.0 Tesla. *Eur Radiol* 2006; **16**:915-921.
22. Wattjes MP, Harzheim M, Kuhl CK et al. Does high-field MR imaging have an influence on the classification of patients with clinically isolated syndromes according to current diagnostic mr imaging criteria for multiple sclerosis? *AJNR Am J Neuroradiol* 2006; **27**:1794-1798.
23. Wattjes MP, Harzheim M, Lutterbey GG et al. Does high field MRI allow an earlier diagnosis of multiple sclerosis? *J Neurol* 2008; **255**:1159-1163.
24. Neema M, Goldberg-Zimring D, Guss ZD et al. 3 T MRI relaxometry detects T2 prolongation in the cerebral normal-appearing white matter in multiple sclerosis. *Neuroimage* 2009; **46**:633-641.
25. Nelson F, Datta S, Garcia N et al. Intracortical lesions by 3T magnetic resonance imaging and correlation with cognitive impairment in multiple sclerosis. *Mult Scler* 2011; **17**:1122-1129.
26. Ropele S, de Graaf W, Khalil M et al. MRI assessment of iron deposition in multiple sclerosis. *J Magn Reson Imaging* 2011; **34**:13-21.
27. Bakshi R, Thompson AJ, Rocca MA et al. MRI in multiple sclerosis: current status and future prospects. *Lancet Neurol* 2008; **7**:615-625.
28. Noseworthy JH, Lucchinetti C, Rodriguez M, Weinshenker BG. Multiple sclerosis. *N Engl J Med* 2000; **343**:938-952.

29. Pender MP, Greer JM. Immunology of multiple sclerosis. *Curr Allergy Asthma Rep* 2007; **7**:285-292.
30. Sadovnick AD. Genetic background of multiple sclerosis. *Autoimmun Rev* 2012; **11**:163-166.
31. Ebers GC. Environmental factors and multiple sclerosis. *Lancet Neurol* 2008; **7**:268-277.
32. Charcot JM. Histologie de la sclérose en plaque. *Gazette des Hopitaux, Paris* 1868; **41**:554-555.
33. Frohman EM, Racke MK, Raine CS. Multiple sclerosis--the plaque and its pathogenesis. *N Engl J Med* 2006; **354**:942-955.
34. Krumbholz M, Derfuss T, Hohlfeld R, Meinl E. B cells and antibodies in multiple sclerosis pathogenesis and therapy. *Nat Rev Neurol* 2012; **8**:613-623.
35. Mehta V, Pei W, Yang G et al. Iron is a sensitive biomarker for inflammation in multiple sclerosis lesions. *PLoS One* 2013; **8**:e57573.
36. Kotter MR, Zhao C, van Rooijen N, Franklin RJM. Macrophage-depletion induced impairment of experimental CNS remyelination is associated with a reduced oligodendrocyte progenitor cell response and altered growth factor expression. *Neurobiology of disease* 2005; **18**:166-175.
37. Barnett MH, Prineas JW. Relapsing and remitting multiple sclerosis: pathology of the newly forming lesion. *Annals of neurology* 2004; **55**:458-468.
38. Sanders P, De Keyser J. Janus faces of microglia in multiple sclerosis. *Brain Res Rev* 2007; **54**:274-285.

39. Lucchinetti C, Bruck W, Parisi J, Scheithauer B, Rodriguez M, Lassmann H. Heterogeneity of multiple sclerosis lesions: implications for the pathogenesis of demyelination. *Ann Neurol* 2000; **47**:707-717.
40. Tanaka R, Iwasaki Y, Koprowski H. Ultrastructural studies of perivascular cuffing cells in multiple sclerosis brain. *Am J Pathol* 1975; **81**:467-478.
41. Nair A, Frederick TJ, Miller SD. Astrocytes in multiple sclerosis: a product of their environment. *Cell Mol Life Sci* 2008; **65**:2702-2720.
42. Patani R, Balaratnam M, Vora A, Reynolds R. Remyelination can be extensive in multiple sclerosis despite a long disease course. *Neuropathology and applied neurobiology* 2007; **33**:277-287.
43. Trapp BD, Peterson J, Ransohoff RM, Rudick R, Mork S, Bo L. Axonal transection in the lesions of multiple sclerosis. *N Engl J Med* 1998; **338**:278-285.
44. Kotter MR, Stadelmann C, Hartung HP. Enhancing remyelination in disease--can we wrap it up? *Brain* 2011; **134**:1882-1900.
45. Bo L, Geurts JJ, Mork SJ, van der Valk P. Grey matter pathology in multiple sclerosis. *Acta Neurol Scand Suppl* 2006; **183**:48-50.
46. Fisher E, Lee JC, Nakamura K, Rudick RA. Gray matter atrophy in multiple sclerosis: a longitudinal study. *Ann Neurol* 2008; **64**:255-265.
47. Fisniku LK, Chard DT, Jackson JS et al. Gray matter atrophy is related to long-term disability in multiple sclerosis. *Ann Neurol* 2008; **64**:247-254.
48. LeVine SM, Chakrabarty A. The role of iron in the pathogenesis of experimental allergic encephalomyelitis and multiple sclerosis. *Ann N Y Acad Sci* 2004; **1012**:252-266.



49. Hallgren B, Sourander P. The effect of age on the non-haemin iron in the human brain. *J Neurochem* 1958; **3**:41-51.
50. LeVine SM. Iron deposits in multiple sclerosis and Alzheimer's disease brains. *Brain Res* 1997; **760**:298-303.
51. Griffiths PD, Dobson BR, Jones GR, Clarke DT. Iron in the basal ganglia in Parkinson's disease. An in vitro study using extended X-ray absorption fine structure and cryo-electron microscopy. *Brain* 1999; **122**:667-673.
52. Craelius W, Migdal MW, Luessenhop CP, Sugar A, Mihalakis I. Iron deposits surrounding multiple sclerosis plaques. *Arch Pathol Lab Med* 1982; **106**:397-399.
53. Adams CW. Perivascular iron deposition and other vascular damage in multiple sclerosis. *J Neurol Neurosurg Psychiatry* 1988; **51**:260-265.
54. Sfagos C, Makis AC, Chaidos A et al. Serum ferritin, transferrin and soluble transferrin receptor levels in multiple sclerosis patients. *mult scler* 2005; **11**:272-275.
55. Rouault TA, Cooperman S. Brain iron metabolism. *Semin Pediatr Neurol* 2006; **13**:142-148.
56. Mehindate K, Sahlas DJ, Frankel D et al. Proinflammatory cytokines promote glial heme oxygenase-1 expression and mitochondrial iron deposition: implications for multiple sclerosis. *J Neurochem* 2001; **77**:1386-1395.
57. Campbell A, Smith MA, Sayre LM, Bondy SC, Perry G. Mechanisms by which metals promote events connected to neurodegenerative diseases. *Brain Res Bull* 2001; **55**:125-132.
58. Halliwell B. Oxidative stress and neurodegeneration: where are we now? *J Neurochem* 2006; **97**:1634-1658.

59. Wellsing-Resnick M. Iron homeostasis and the inflammatory response. *Ann Rev Nutr* 2010; **30**:102-122.
60. Blake DR, Gallagher PJ, Potter AR, Bell MJ, Bacon PA. The effect of synovial iron on the progression of rheumatoid disease. A histological assessment of patients with early rheumatoid synovitis. *Arthritis Rheum* 1984; **27**:495-501.
61. Facchini FS. Near-iron deficiency-induced remission of gouty arthritis. *Rheumatology* 2003; **42**:1550-1555.
62. Drayer B, Burger P, Hurwitz B, Dawson D, Cain J. Reduced signal intensity on MR images of thalamus and putamen in multiple sclerosis: increased iron content? *AJR Am J Roentgenol* 1987; **149**:357-363.
63. Neema M, Arora A, Healy BC et al. Deep gray matter involvement on brain MRI scans is associated with clinical progression in multiple sclerosis. *J Neuroimaging* 2009; **19**:3-8.
64. Khalil M, Enzinger C, Langkammer C et al. Quantitative assessment of brain iron by R(2)\* relaxometry in patients with clinically isolated syndrome and relapsing-remitting multiple sclerosis. *Mult Scler* 2009; **15**:1048-1054.
65. Hammond KE, Metcalf M, Carvajal L et al. Quantitative in vivo magnetic resonance imaging of multiple sclerosis at 7 Tesla with sensitivity to iron. *Ann Neurol* 2008; **64**:707-713.
66. Ge Y, Jensen JH, Lu H et al. Quantitative assessment of iron accumulation in the deep gray matter of multiple sclerosis by magnetic field correlation imaging. *AJNR Am J Neuroradiol* 2007; **28**:1639-1644.
67. Khalil M, Langkammer C, Ropele S et al. Determinants of brain iron in multiple sclerosis: A quantitative 3T MRI study. *Neurology* 2011; **77**:1691-1697.

68. Hagemeyer J, Weinstock-Guttman B, Bergsland N et al. Iron deposition on SWI-filtered phase in the subcortical deep gray matter of patients with clinically isolated syndrome may precede structure-specific atrophy. *AJNR Am J Neuroradiol* 2012; **33**:1596-1601.
69. Dawson JD. The histology of disseminated sclerosis. *Trans Roy Soc Edinb* 1916; **50**:517-740.
70. Palmer S, Bradley WG, Chen DY, Patel S. Subcallosal striations: early findings of multiple sclerosis on sagittal, thin-section, fast FLAIR MR images. *Radiology* 1999; **210**:149-153.
71. FOG T. ON THE VESSEL-PLAQUE RELATIONS IN THE BRAIN IN MULTIPLE SCLEROSIS. *Acta Neurol Scand Suppl* 1963; **39**:SUPPL4:258-62.
72. Kermode AG, Thompson AJ, Tofts P et al. Breakdown of the blood-brain barrier precedes symptoms and other MRI signs of new lesions in multiple sclerosis. Pathogenetic and clinical implications. *Brain* 1990; **113**:1477-1489.
73. Adams CW, Poston RN, Buk SJ, Sidhu YS, Vipond H. Inflammatory vasculitis in multiple sclerosis. *J Neurol Sci* 1985; **69**:269-283.
74. Tan IL, van Schijndel RA, Pouwels PJ et al. MR venography of multiple sclerosis. *AJNR Am J Neuroradiol* 2000; **21**:1039-1042.
75. Tallantyre EC, Morgan PS, Dixon JE et al. A comparison of 3T and 7T in the detection of small parenchymal veins within MS lesions. *Invest Radiol* 2009; **44**:491-494.
76. Tallantyre EC, Dixon JE, Donaldson I et al. Ultra-high-field imaging distinguishes MS lesions from asymptomatic white matter lesions. *Neurology* 2011; **76**:534-539.

77. Putnam TJ. Evidences of vascular occlusion in multiple sclerosis and "encephalomyelitis". *Arch NeurPsych* 1937; **37**:1298-1321.
78. Markl M, Leupold J. Gradient echo imaging. *J Magn Reson Imaging* 2012; **35**:1274-1289.
79. Reichenbach JR, Venkatesan R, Yablonskiy DA, Thompson MR, Lai S, Haacke EM. Theory and application of static field inhomogeneity effects in gradient-echo imaging. *J Magn Reson Imaging* 1997; **7**:266-279.
80. Haacke EM, Brown RW, Thompson MR, Venkatesan R. One-dimensional fourier imaging, k-space and gradient echoes. eds. *Magnetic resonance imaging: physical principles and sequence design*. New York: J. Wiley-Liss, 1999: 139-163.
81. Haacke EM, Brown RW, Thompson MR, Venkatesan R. Introductory signal acquisition methods: free induction decay, spin echoes, inversion recovery and spectroscopy. eds. *Magnetic resonance imaging: physical principles and sequence design*. New York: J. Wiley-Liss, 1999: 111-138.
82. Chu SC, Xu Y, Balschi JA, Springer CSJ. Bulk magnetic susceptibility shifts in NMR studies of compartmentalized samples: use of paramagnetic reagents. *Magn Reson Med* 1990; **13**:239-262.
83. Haacke EM, Mittal S, Wu Z, Neelavalli J, Cheng YCN. Susceptibility-weighted imaging: technical aspects and clinical applications, part 1. *AJNR Am J Neuroradiol* 2009; **30**:19-30.
84. Noll DC, Nishimura DG, Macovski A. Homodyne detection in magnetic resonance imaging. *IEEE Trans Med Imaging* 1991; **10**:154-163.

85. Yao B, Li TQ, Gelderen P, Shmueli K, de Zwart JA, Duyn JH. Susceptibility contrast in high field MRI of human brain as a function of tissue iron content. *Neuroimage* 2009; **44**:1259-1266.
86. Liu T, Khalidov I, de Rochefort L et al. A novel background field removal method for MRI using projection onto dipole fields (PDF). *NMR Biomed* 2011; **24**:1129-1136.
87. Schweser F, Deistung A, Lehr BW, Reichenbach JR. Quantitative imaging of intrinsic magnetic tissue properties using MRI signal phase: an approach to in vivo brain iron metabolism? *Neuroimage* 2011; **54**:2789-2807.
88. Dumoulin CL, Souza SP, Walker MF, Wagle W. Three-dimensional phase contrast angiography. *Magn Reson Med* 1989; **9**:139-149.
89. de Rochefort L, Liu T, Kressler B et al. Quantitative susceptibility map reconstruction from MR phase data using bayesian regularization: validation and application to brain imaging. *Magn Reson Med* 2010; **63**:194-206.
90. Jain V, Langham MC, Wehrli FW. MRI estimation of global brain oxygen consumption rate. *J Cereb Blood Flow Metab* 2010; **30**:1598-1607.
91. Haacke EM, Miao Y, Liu M et al. Correlation of putative iron content as represented by changes in R2\* and phase with age in deep gray matter of healthy adults. *J Magn Reson Imaging* 2010; **32**:561-576.
92. Ogawa S, Lee TM, Kay AR, Tank DW. Brain magnetic resonance imaging with contrast dependent on blood oxygenation. *Proc Natl Acad Sci U S A* 1990; **87**:9868-9872.

93. Ogawa S, Lee TM, Barrere B. The sensitivity of magnetic resonance image signals of a rat brain to changes in the cerebral venous blood oxygenation. *Magn Reson Med* 1993; **29**:205-210.
94. Ogawa S, Menon RS, Tank DW et al. Functional brain mapping by blood oxygenation level-dependent contrast magnetic resonance imaging. A comparison of signal characteristics with a biophysical model. *Biophys J* 1993; **64**:803-812.
95. Lai S, Reichenbach JR, Haacke EM. Commutator filter: a novel technique for the identification of structures producing significant susceptibility inhomogeneities and its application to functional MRI. *Magn Reson Med* 1996; **36**:781-787.
96. Reichenbach JR, Venkatesan R, Schillinger DJ, Kido DK, Haacke EM. Small vessels in the human brain: MR venography with deoxyhemoglobin as an intrinsic contrast agent. *Radiology* 1997; **204**:272-277.
97. Reichenbach JR, Barth M, Haacke EM, Klarhofer M, Kaiser WA, Moser E. High-resolution MR venography at 3.0 Tesla. *J Comput Assist Tomogr* 2000; **24**:949-957.
98. Reichenbach JR, Essig M, Haacke EM et al. High-resolution venography of the brain using magnetic resonance imaging. *MAGMA* 1998; **6**:62-69.
99. Weisskoff RM, Kiihne S. MRI susceptometry: image-based measurement of absolute susceptibility of MR contrast agents and human blood. *Magn Reson Imaging* 1992; **24**:375-383.
100. Haacke EM, Xu Y, Cheng YC, Reichenbach JR. Susceptibility weighted imaging (SWI). *Magn Reson Med* 2004; **52**:612-618.
101. Xu Y, Haacke EM. The role of voxel aspect ratio in determining apparent vascular phase behavior in susceptibility weighted imaging. *Magn Reson Imaging* 2006; **24**:155-160.

102. Casciaro S, Bianco R, Franchini R, Casciaro E, Conversano F. A new automatic phase mask filter for high-resolution brain venography at 3 T: theoretical background and experimental validation. *Magn Reson Imaging* 2010; **28**:511-519.
103. Brainovich V, Sabatini U, Hagberg GE. Advantages of using multiple-echo image combination and asymmetric triangular phase masking in magnetic resonance venography at 3 T. *Magn Reson Imaging* 2009; **27**:23-37.
104. Martinez Santiesteban FM, Swanson SD, Noll DC, Anderson DJ. Object orientation independence of Susceptibility Weighted Imaging by using a Sigmoid-type phase window. *14th Annual Meeting of ISMRM* 2006; 2399.
105. Mie MB, Nissen JC, Zollner FG et al. Susceptibility weighted imaging (SWI) of the kidney at 3T--initial results. *Z Med Phys* 2010; **20**:143-150.
106. Mittal S, Wu Z, Neelavalli J, Haacke EM. Susceptibility-weighted imaging: technical aspects and clinical applications, part 2. *AJNR Am J Neuroradiol* 2009; **30**:232-252.
107. Peran P, Hagberg G, Luccichenti G et al. Voxel-based analysis of R2\* maps in the healthy human brain. *J Magn Reson Imaging* 2007; **26**:1413-1420.
108. Denk C, Rauscher A. Susceptibility weighted imaging with multiple echoes. *J Magn Reson Imaging* 2010; **31**:185-191.
109. Gelman N, Gorell JM, Barker PB et al. MR imaging of human brain at 3.0 T: preliminary report on transverse relaxation rates and relation to estimated iron content. *Neuroradiology* 1999; **210**:759-767.
110. Stankiewicz J, Panter SS, Neema M, Arora A, Batt CE, Bakshi R. Iron in chronic brain disorders: imaging and neurotherapeutic implications. *Neurotherapeutics* 2007; **4**:371-386.

111. Walsh AJ, Lebel RM, Eissa A et al. Multiple sclerosis: validation of MR imaging for quantification and detection of iron. *Radiology* 2013; **267**:531-542.
112. Peran P, Cherubini A, Assogna F et al. Magnetic resonance imaging markers of Parkinson's disease nigrostriatal signature. *Brain* 2010; **133**:3423-3433.
113. Moon WJ, Kim HJ, Roh HG, Choi JW, Han SH. Fluid-attenuated inversion recovery hypointensity of the pulvinar nucleus of patients with Alzheimer disease: its possible association with iron accumulation as evidenced by the t2(\*) map. *Korean J Radiol* 2012; **13**:674-683.
114. Novellino F, Cherubini A, Chiriaco C et al. Brain iron deposition in essential tremor: A quantitative 3-tesla magnetic resonance imaging study. *Mov Disord* 2012; **28**:196-200.
115. Yan S, Sun J, Chen Y, Selim M, Lou M. Brain iron deposition in white matter hyperintensities: a 3-T MRI study. *Age* 2012; DOI:10.1007/s11.54-012-9487-6.
116. Cherubini A, Peran P, Hagberg GE et al. Characterization of white matter fiber bundles with T2\* relaxometry and diffusion tensor imaging. *Magn Reson Med* 2009; **61**:1066-1072.
117. Feng Y, He T, Gatehouse PD et al. Improved MRI R(2) \* relaxometry of iron-loaded liver with noise correction. *Magn Reson Med* 2013; DOI:10.1002/mrm.24607.
118. He T, Gatehouse PD, Smith GC, Mohiaddin RH, Pennell DJ, Firmin DN. Myocardial T2\* measurements in iron-overloaded thalassemia: An in vivo study to investigate optimal methods of quantification. *Magn Reson Med* 2008; **60**:1082-1089.



119. Putnam TJ. Studies in multiple sclerosis IV. "Encephalitis" and sclerotic plaques produced by venular obstruction. *Arch NeurPsych* 1935; **33**:929-940.
120. Schelling F. Damaging venous reflux into the skull or spine: relevance to multiple sclerosis. *Med Hypotheses* 1986; **21**:141-148.
121. Zamboni P. The big idea: iron-dependent inflammation in venous disease and proposed parallels in multiple sclerosis. *J R Soc Med* 2006; **99**:589-593.
122. Uflacker R. Veins of the head and neck. ed. Atlas of vascular anatomy: an angiographic approach. Philadelphia: Lippincott Williams & Wilkins, 2007: 69-102.
123. Vascular supply of the brain. In: Standring S, Crossman AR, eds. Gray's anatomy: the anatomical basis of clinical practice. London: Elsevier Ltd, 2005: 295-306.
124. Neck. In: Standring S, Berkovitz BKB, eds. Gray's anatomy: the anatomical basis of clinical practice. London: Elsevier Ltd, 2005: 531-566.
125. Abrams HL. The vertebral and azygos venous systems, and some variations in systemic venous return. *Radiology* 1957; **69**:508-526.
126. Zamboni P, Menegatti E, Bartolomei I et al. Intracranial venous haemodynamics in multiple sclerosis. *Curr Neurovasc Res* 2007; **4**:252-258.
127. Zamboni P, Galeotti R, Menegatti E et al. Chronic cerebrospinal venous insufficiency in patients with multiple sclerosis. *J Neurol Neurosurg Psychiatry* 2009; **80**:392-399.
128. Zamboni P, Menegatti E, Galeotti R et al. The value of cerebral Doppler venous haemodynamics in the assessment of multiple sclerosis. *J Neurol Sci* 2009; **282**:21-27.

129. Baracchini C, Perini P, Calabrese M, Causin F, Rinaldi F, Gallo P. No evidence of chronic cerebrospinal venous insufficiency at multiple sclerosis onset. *Ann Neurol* 2011; **69**:90-99.
130. Garaci FG, Marziali S, Meschini A et al. Brain hemodynamic changes associated with chronic cerebrospinal venous insufficiency are not specific to multiple sclerosis and do not increase its severity. *Radiology* 2012; **265**:233-239.
131. Mayer CA, Pfeilschifter W, Lorenz MW et al. The perfect crime? CCSVI not leaving a trace in MS. *J Neurol Neurosurg Psychiatry* 2011; **82**:436-440.
132. Chambers B, Chambers J, Cameron H, Macdonell R. Chronic cerebrospinal venous insufficiency is not more prevalent in patients with mild multiple sclerosis: a sonographer-blinded, case-control ultrasound study. *Mult Scler* 2012; **19**:749-756.
133. Zamboni P, Morovic S, Menegatti E, Viselner G, Nicolaidis AN. Screening for chronic cerebrospinal venous insufficiency (CCSVI) using ultrasound - Recommendations for a protocol. *Int Angiol* 2011; **30**:571-597.
134. Meyer-Schwickerath R, Haug C, Hacker A et al. Intracranial venous pressure is normal in patients with multiple sclerosis. *Mult Scler* 2011; **17**:637-638.
135. Worthington V, Killestein J, Eikelenboom MJ et al. Normal CSF ferritin levels in MS suggest against etiologic role of chronic venous insufficiency. *Neurology* 2010; **75**:1617-1622.
136. Weinstock-Guttman B, Ramanathan M, Marr K et al. Clinical correlates of chronic cerebrospinal venous insufficiency in multiple sclerosis. *BMC Neurol* 2012; **12**:26.
137. Reekers JA. CCSVI and MS: A Never-Ending Story. *Eur J Vasc Endovasc Surg* 2012; **43**:127-128.

138. Zamboni P, Galeotti R, Menegatti E et al. A prospective open-label study of endovascular treatment of chronic cerebrospinal venous insufficiency. *J Vasc Surg* 2009; **50**:1348-1358.
139. Zamboni P, Galeotti R, Weinstock-Guttman B, Kennedy C, Salvi F, Zivadinov R. Venous Angioplasty in Patients with Multiple Sclerosis: Results of a Pilot Study. *Eur J Vasc Endovasc Surg* 2011; **43**:116-122.
140. Laupacis A, Slutsky AS. Endovascular treatment for multiple sclerosis: The intersection of science, policy and the public. *Open Med* 2010; **4**:e197-9.
141. Menegatti E, Genova V, Tessari M et al. The reproducibility of colour Doppler in chronic cerebrospinal venous insufficiency associated with multiple sclerosis. *Int Angiol* 2010; **29**:121-126.
142. Doepp F, Wurfel JT, Pfueller CF et al. Venous drainage in multiple sclerosis: a combined MRI and ultrasound study. *Neurology* 2011; **77**:1745-1751.
143. Dolic K, Marr K, Valnarov V et al. Intra- and extraluminal structural and functional venous anomalies in multiple sclerosis, as evidenced by 2 noninvasive imaging techniques. *AJNR Am J Neuroradiol* 2012; **33**:16-23.
144. McTaggart RA, Fischbein NJ, Elkins CJ et al. Extracranial venous drainage patterns in patients with multiple sclerosis and healthy controls. *AJNR Am J Neuroradiol* 2012; **33**:1615-1620.
145. Mistry N, Dixon J, Tallantyre E et al. Central Veins in Brain Lesions Visualized With High-Field Magnetic Resonance Imaging: A Pathologically Specific Diagnostic Biomarker for Inflammatory Demyelination in the Brain. *JAMA Neurol* 2013; 1-6.

## 2 Comparison of multi-echo post-processing schemes for susceptibility weighted imaging with use of linear and non-linear mask functions

### 2.1 Introduction

Susceptibility weighted imaging (SWI) is a magnetic resonance imaging (MRI) technique that exploits the effect of variations in magnetic susceptibility (the degree of magnetization of a material in response to an applied magnetic field) on gradient echo signal to produce enhanced image contrast. Most MRI studies reconstruct only the magnitude image; phase is generally discarded. However, the phase data contain potentially useful information about inclusions in the imaging volume that change the local magnetic field, i.e. of non-homogeneous magnetic susceptibility. SWI processing allows this information to be incorporated into the magnitude image since the underlying structure may not necessarily be visible on magnitude alone<sup>1</sup>.

SWI was originally used to produce high-resolution venograms<sup>2</sup>. SWI has found additional uses in clinical and research settings due to its sensitivity to other physiologically relevant magnetic field perturbors such as blood products<sup>3</sup>, iron<sup>4</sup> and calcium<sup>5</sup>. However, single-echo SWI is useful in the visualization but not the quantification of field perturbors. Modifications of SWI allow simultaneous quantification of the nature or amount of the perturber. For example, the effective transverse relaxation rate ( $R_2^*$ ), which can be extracted from multi-echo gradient echo

data via voxel-wise curve fitting, is a metric that scales linearly with iron concentration in the brain<sup>6</sup>.

Brainovich et al.<sup>7</sup> described a post-processing scheme for dual-echo gradient echo data. In this scheme, average phase and average magnitude volumes were generated and subsequently used to produce a single SWI volume. Denk and Rauscher<sup>8</sup> used a multi-echo acquisition with five echoes to produce five SWI volumes that were subsequently averaged to produce a single average SWI volume. They reported improvements in contrast to noise ratio (CNR) of veins compared to conventional SWI. Additionally, they described computation of  $R_2^*$  maps as a natural extension of the multi-echo acquisition. In all cases, a conventional linear phase mask function for SWI was employed. The use of alternative mask functions theoretically results in increased CNR of cerebral veins<sup>9</sup>, although this claim has not been rigorously tested in vivo.

There are two main goals of this work: first, a comparison of three SWI post-processing schemes (single echo and two multi-echo methods); and second, a comparison of the conventional (i.e. linear) mask function with a novel non-linear mask function. We identified the following objectives: (i) to describe and outline modifications to previously published multi-echo SWI, as well as describe a non-linear mask function, (ii) to optimize the number of mask function multiplications for all combinations of post-processing scheme and mask function; and, (iii) to compare all post-processing schemes and mask functions in vivo using both quantitative and radiological assessments.

This work has been presented, in part, at the 20<sup>th</sup> Annual Meeting of the ISMRM<sup>10</sup>.

## 2.2 Methods

Processing was performed in MATLAB (The MathWorks, Inc., Natwick, MA) and FSL (FMRIB, Oxford, UK). Statistical analyses were performed in SPSS (IBM, Armonk, NY).

### 2.2.1 SWI post-processing schemes

Three post-processing schemes were compared: one for single-echo SWI and two for multi-echo SWI. First, single-echo SWI processing involves background phase removal using the homodyne method<sup>11</sup>, generation of a phase mask, and multiplication of the  $m^{\text{th}}$  power of the mask by the magnitude image<sup>12</sup>.

Second, the multi-echo SWI method of Denk and Rauscher<sup>8</sup> was modified, and herein is referred to as the post-average method. Post-average multi-echo SWI involves single-echo SWI processing on data from each echo, and averaging of the resulting images. Denk and Rauscher prescribe this technique with a linearly (in echo time) increasing homodyne filter width to remove background contributions to phase from each echo in order to account for the additional phase wrapping at longer echo times. We used a constant (with echo time) filter size, as a compromise between eliminating phase wraps in later echoes and preserving the relevant contrast between echoes in a consistent manner.

Third, a frequency-based method for multi-echo SWI was used, and is based upon the method described initially by Brainovich et al.<sup>7</sup>. For the image volume reconstructed from each echo, the background phase was removed using the homodyne method.

Successive phase images were then temporally unwrapped using MATLAB's 1D unwrap function on the echo time dependent voxel data. Each unwrapped phase image was then divided by its corresponding TE to produce a frequency image. A weighted average of frequency was calculated from these individual frequency images: weights were inversely proportional to the variance of the frequency:  $(\text{magnitude})^2(\text{TE})^2$ . A mask was computed from the average frequency image, and its  $m^{\text{th}}$  power was multiplied by the average magnitude image for that slice. This method is similar to what has been described by Brainovich et al.<sup>7</sup> but additionally involves the temporal unwrapping of phase, as well as masking the weighted average of frequency maps rather than the arithmetic mean of the phase images. While the mean of the frequency maps is a physical and intuitive quantity, the mean of the phase images used by Brainovich et al.<sup>7</sup> is not logical from a physical or mathematical perspective.

For the homodyne filter, a 2D Hann window (one period of a raised cosine) with dimensions equal to 30% (for multi-echo) or 20% (for single-echo) of the respective matrix dimensions, rounded to the nearest integer, was employed. This constant width filter, in conjunction with the temporal phase unwrapping that was used, resulted in the ability to remove all relevant phase wraps.

### 2.2.2 SWI mask functions

Two different mask functions were compared. First, the conventional linear mask function was used. In general form, the linear mask,  $L$ , is defined as follows:

$$L(x) = \begin{cases} 0 & \text{if } x < -X \\ \frac{1}{X}(x + X) & \text{if } -X \leq x \leq 0 \\ 1 & \text{if } x > 0 \end{cases} . \quad [2.1]$$

For single-echo and post-average,  $X = -\pi$  rad is used, with  $x$  in radians. For frequency-based SWI where  $x$  is in units of Hertz,  $X$  is set to the equivalent value:  $(-\pi \text{ rad})(1 \text{ cycle}/2\pi \text{ rad})(1/\text{TE}_{\text{average}}) = 18.2 \text{ Hz}$ , where  $\text{TE}_{\text{average}}$  is the average of the echo times used (described below).

Second, a non-linear mask function was used. This Hann-derived mask,  $H$ , is defined as follows:

$$H(x) = \begin{cases} 0 & \text{if } x < -X \\ \frac{1}{2} [1 + \cos(\frac{\pi x}{X})] & \text{if } -X \leq x \leq 0 \\ 1 & \text{if } x > 0 \end{cases} . \quad [2.2]$$

The values  $X$  and  $x$  can be expressed in either units of phase or frequency.  $X$  was set to  $\pi$  (for single-echo and post-average) or the equivalent value of 18.2 Hz (for frequency-based SWI). Compared to the linear filter, it was expected that this filter would result in reduced image noise and increased contrast for negative phase/frequency structures.

### 2.2.3 MR imaging

All scanning was performed on a 3T MRI scanner (TIM Trio, Siemens Medical Solutions, Erlangen, Germany) using a 32-channel head coil. For evaluation and comparison of different SWI post-processing schemes, 10 healthy volunteers were scanned (7 women/3 men; mean $\pm$ standard deviation age=28 $\pm$ 7 years). Data were



collected using a single-echo 3D gradient echo (TE/TR=20/30 ms, BW=80 Hz/pixel, TA=6:28, fully flow-compensated) and multi-echo 3D gradient echo sequence (TE<sub>1</sub>=10 ms, echo spacing=7 ms, 6 echoes, TR=52 ms, BW=160 Hz/pixel, TA=11:12, first echo fully flow-compensated). For both sequences, common parameters were: matrix, 448 x 336 x 60; field of view, 224 x 178 x 60 mm<sup>3</sup>; flip angle, 12°; slice oversampling, 12.5%. Both acquisitions were accelerated with GRAPPA (R=2, reference lines=24). Phase data from each channel were combined on-line using vendor software. This study was approved by the institutional review board. Informed consent was obtained in writing from all participants.

Six SWI volumes were created per subject: three post-processing schemes with two mask functions each. The single-echo magnitude volume was registered to the first echo magnitude of the multi-echo volumes to allow careful comparison of the different methods on individual vessels or regions even if motion were present between the different volumes. Single-echo SWI volumes were computed, following which the magnitude registration parameters were applied.

#### 2.2.4 Numerical optimization

A 2D numerical phantom was created to evaluate the CNR of a vein using different post-processing schemes and mask functions. The purpose of this simulation was to optimize the number of mask multiplications,  $m$ , for different post-processing schemes. The phantom consisted of a 512x512 array. All pixels were assigned values of the effective transverse relaxation time,  $T_2^*$  (32 ms), and equilibrium signal,  $S_0$  (425), based on their

measured values in white matter (WM) in the in vivo multi-echo data. One column was designated the vein compartment and assigned a frequency which was varied for different trials. All other pixels were assigned a frequency of zero for all trials. This is similar to a previously described simulation to optimize the number of mask multiplications for conventional SWI<sup>12</sup>.

Data were simulated by creating magnitude and phase image pairs for different TEs. At a given TE, signal magnitude was calculated according to:

$$S(TE) = S_0 \exp(-TE/T_2^*). \quad [2.3]$$

Phase was calculated as (frequency)x(TE). Each magnitude and phase pair was converted into real and imaginary images, to each of which normally distributed noise with standard deviation of 18 was added to ensure comparable signal-to-noise ratio (SNR) in simulated data when compared to periventricular WM using our acquisition parameters. The noisy real and imaginary images were then converted back to magnitude and phase.

A multi-echo data set was simulated by creating magnitude/phase pairs for TEs of 10, 17, 24, 31, 38 and 45 ms. From the same simulated multi-echo data, one multi-echo SWI image was generated according to each of the four possible combinations of multi-echo post-processing scheme (post-average and frequency-based) and mask function (linear and non-linear).

Single-echo data were simulated by creating one magnitude/phase pair at TE=20 ms. Noise was decreased by a factor of  $2^{0.5}$  to simulate decreased noise accompanying the

reduction in bandwidth from 160 Hz/pixel in the multi-echo acquisition to 80 Hz/pixel in the single-echo acquisition. Additionally, the WM  $S_0$  was decreased by 16% to account for the reduction in steady state signal accompanying the decrease in TR. For the simulated single-echo data, one SWI image was produced with each mask function.

Contrast was measured as the difference in mean signals between two regions of interest (ROIs) in the SWI volumes: one placed in the vein compartment, and one in the WM compartment. The CNR was calculated as this contrast divided by the standard deviation of the signal in the latter ROI, which is the standard definition of CNR used in SWI numerical optimization<sup>13</sup>.

### 2.2.5 Visual optimization

Values of the mask power,  $m$ , were also optimized by three radiology residents, each with 29 months experience, who rated SWI images from four volunteers. For each volunteer, image volumes included each of the six SWI combinations processed with a range of  $m$  values. Images processed with the linear mask function were processed with  $m$ 's from 0 to 11, incremented in steps of 1. Images processed with the non-conventional filter were processed with  $m$ 's from 0 to 55, incremented in steps of 5. This larger range and coarser increment of  $m$  values was found to yield a similar range of contrasts to the images processed with the conventional mask. Accordingly, raters were shown 24 sets of 12 volumes. The raters were not blinded to the value of  $m$ , but each set was presented in a random order to ensure experience from early sets did not influence rating of later sets. Rating instructions were as follows: "For each set, identify the single value of  $m$  which is

optimal. When considering optimal  $m$ , consider SWI quality from a radiological standpoint. Please consider how structure contrast as well as image noise are affected by choice of  $m$ . Specifically, you should consider the visibility of veins (both small veins such as those at the lateral ventricles, and large veins) as well as other structures that may be targeted with SWI such as: red nucleus, subthalamic nucleus, globus pallidus.” Each rater performed rating independently. To evaluate inter-rater agreement, two-way mixed average measures interclass correlation coefficient was calculated for the pooled ratings.

### 2.2.6 Measurements of $R_2^*$

$R_2^*$  images were calculated by performing a voxel-wise curve fit of the magnitude time curve to Eq. 2.3 above. The fitting was performed using the Levenberg-Marquardt algorithm for non-linear least-squares curve fitting.

### 2.2.7 ROI analyses

For in vivo data, ROI analyses were used to compare optimized SWI techniques. For each subject, ROIs were drawn in the right hemisphere of single-echo, linearly masked SWI volume and propagated into the other volumes. SNR was approximated in the frontal WM of all subjects as the mean divided by standard deviation of the signal in the ROI. CNR was measured between various anatomical structures [globus pallidus (GP), optic radiations (OR), periventricular veins, subthalamic nucleus (STN), and red nucleus (RN)] and adjacent WM as the difference between mean values of signal in two ROIs

(one in the structure of interest, one in adjacent WM) divided by the standard deviation of signal in the WM ROI.

### 2.2.8 Visual comparison

The same three raters evaluated the optimized SWI images with respect to visibility of different structures. For each of the ten volunteers, the six different SWI volumes were assigned a random letter for blinding purposes. Raters were instructed to rank the volumes from best (rank 1) to worst (rank 6) for different structures. Specific instructions were: “consider: the contrast of the structure with surrounding tissue, the ability to resolve its borders, and how image noise influences visibility.” Visibility was ranked for the same structures in which CNR was measured. Qualitative impression of SNR in frontal WM was also ranked. Images were rated for severity of artifacts at sinuses from least severe (rank 1) to most severe (rank 6).

To evaluate inter-rater agreement, interclass correlation coefficient was calculated on rankings of each structure analyzed. For each volunteer, for each combination of processing scheme and mask function, the three ranks assigned by the raters were averaged to create a mean rank. To separately test the significance of the two main effects (processing scheme and filter), for each level of each main effect, mean ranks were added across all levels of the other main effect. Non-parametric related samples tests were then used to compare all levels of a given effect: Friedman test for scheme, Wilcoxon signed-rank test for filter. Where appropriate, the Wilcoxon test was used post-hoc with Bonferroni correction.

## 2.3 Results

### 2.3.1 Optimization of $m$

Plots of CNR as a function of the mask power  $m$  are presented (Figure 2.1) for several different choices of the frequency of the vein compartment of the numerical phantom. Optimal values of  $m$  depend strongly on frequency of the vein; minimum and maximum values of optimal  $m$  over the range of frequencies investigated are presented in Table 2.1. According to simulation, greater CNR is achievable with the non-linear mask, although typically larger values of  $m$  are required. Simulation predicts that the frequency-based method allows the greatest CNR, and that both multi-echo methods are superior to single-echo SWI.

Optimization of  $m$  was also performed via visual rating of images. To measure the optimal value of  $m$  for a given processing combination, the median (across the four volunteers) of the median (across the three raters) is reported in Table 2.1. In all cases, the optimal value as determined by the raters falls within the range of optimal values predicted by simulation. The interclass correlation coefficient was found to be 0.96, indicating excellent inter-rater agreement. When implementing different SWI techniques herein, we use the values of  $m$  determined to be optimal by the raters.

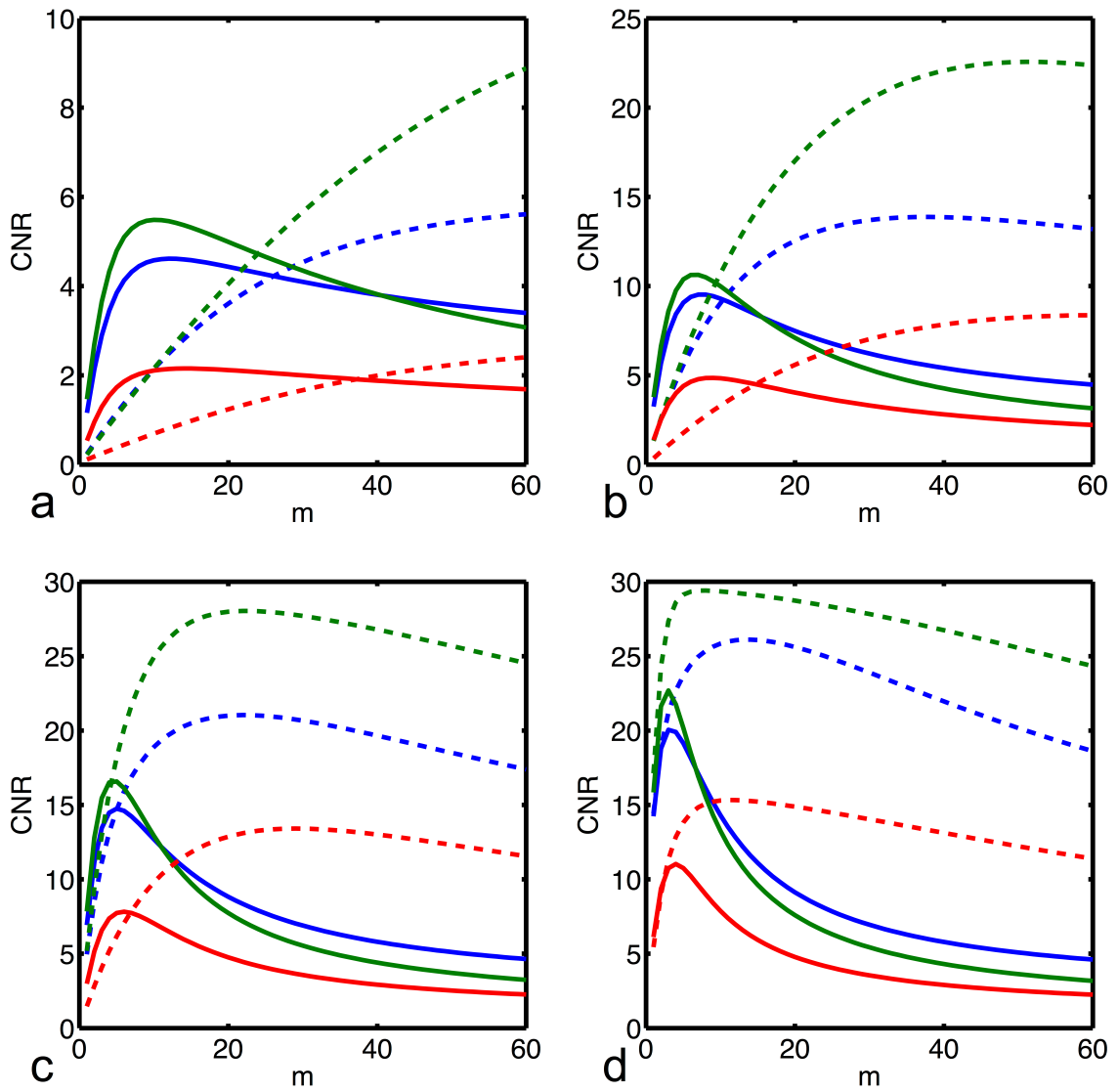


Figure 2.1 CNR versus number of mask multiplications ( $m$ ) for different SWI post-processing schemes (red: single-echo, blue: post-average, green: frequency-based) and mask functions (solid: linear, dashed: non-linear) as simulated for a vein of varying frequency in WM. Simulated frequencies were: -1.0 Hz (a), -2.5 Hz (b), -5 Hz (c), -10.0 Hz (d).

Table 2.1 Optimization of  $m$ 

		Simulation		Radiologist Rating
		Min. optimal $m^a$	Max. optimal $m^b$	Optimal $m$ (min <sup>c</sup> ,max <sup>d</sup> )
Single echo	Linear	4	17	<b>6</b> (4,7)
	Non-linear	11	>60	<b>35</b> (20,35)
Post-average	Linear	3	15	<b>7</b> (5,10)
	Non-linear	14	>60	<b>35</b> (25,45)
Frequency-based	Linear	3	15	<b>5</b> (2,7)
	Non-linear	8	>60	<b>25</b> (20,40)

<sup>a,b</sup>Minimum, maximum values, respectively, of  $m$  that yield maximum CNR for any frequency of vein simulated.

<sup>c,d</sup>Minimum, maximum values, respectively, assigned by any of the three raters.



### 2.3.2 In vivo data

Minimum intensity projections through 4 mm for a subset of a slice at the level of the basal ganglia are shown in Figure 2.2 for all permutations of post-processing scheme and mask function, using optimal values of  $m$  from Table 2.1.

In general, the non-linear mask function results in improved noise characteristics compared to the linear filter, and its use also dramatically enhances contrast in some regions, for example for large veins (arrow in Fig. 2.2f) and at the edges of the basal ganglia (arrowheads in Fig. 2.2f). Small veins which are not visible in single-echo SWI are readily detected in all implementations of multi-echo SWI, such as at the horns of the ventricles (arrows in Fig. 2.2b), although their appearance is smoother and more continuous when the linear filter and/or post-average processing is used.

### 2.3.3 ROI analyses

Normalized measurements of SNR and CNR are presented in Figure 2.3. The non-linear mask function results in a significantly larger SNR or CNR ( $P < 0.05$  for GP,  $P < 0.01$  for periventricular veins, STN;  $P < 0.001$  for frontal WM, OR, RN). The frequency-based scheme results in significantly larger CNR or SNR than both post-average and single-echo, except for GP where no significant difference is detected between post-average and frequency-based processing, although both result in significantly larger CNR than single-echo. Specific P-values are presented for pair-wise comparisons of processing scheme in Fig. 2.3.

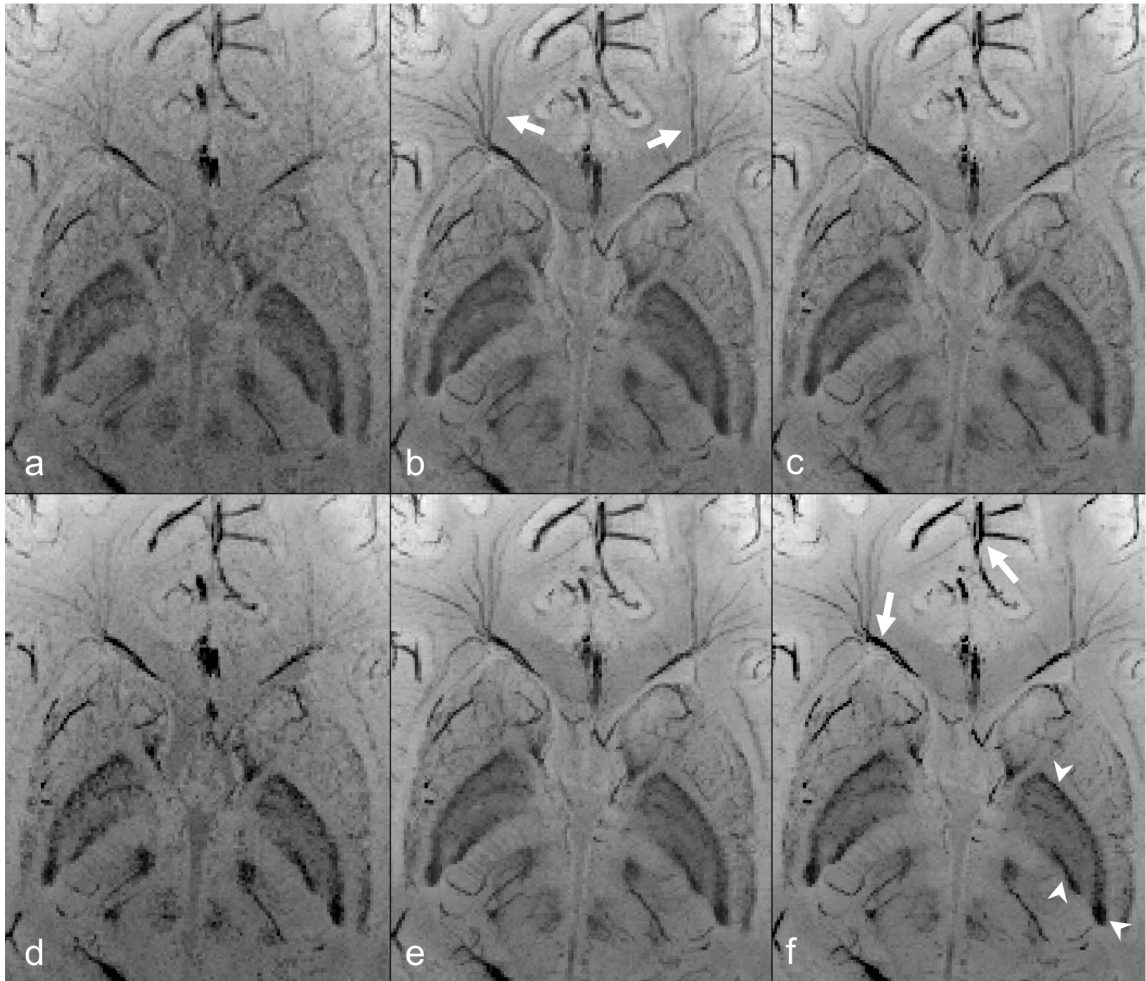


Figure 2.2 Minimum intensity projections through 4 mm at the basal ganglia for different SWI post-processing schemes (first column: single-echo, second column: post-average, third column: frequency-based) and mask functions (first row: linear mask, second row: non-linear mask).

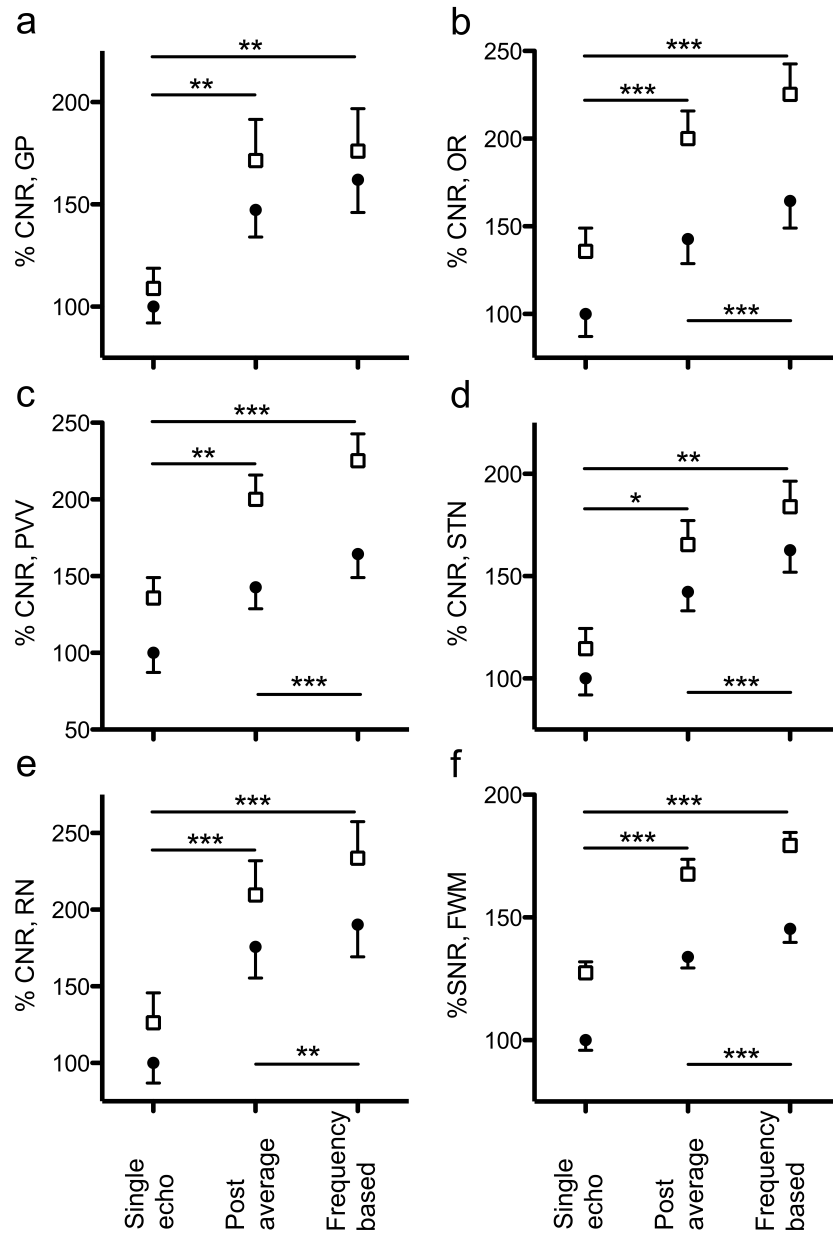


Figure 2.3 CNR for GP (a), OR (b), periventricular veins (PVV) (c), STN (d), RN (e), and SNR for frontal WM (f). Filled black circles: linear mask function; empty squares: non-linear mask function. Points: mean; bars: standard error (n=10). Values have been normalized by the mean value of the metric in linearly masked single-echo SWI. Illustrated are significant P-values for pairwise comparison of post-processing schemes (\*  $P < 0.05$ , \*\*  $P < 0.01$ , \*\*\*  $P < 0.001$ ).

### 2.3.4 Visual comparison

Mean ranks are presented (Figure 2.4) for qualitative impression of SNR of frontal WM, and for visibility of various structures. For all paramagnetic perturbors (GP, STN, RN, periventricular veins), the linear filter resulted in significantly ( $P<0.001$ ) greater visibility (equivalently, lower mean rank). The post-average scheme resulted in significantly lower mean ranks than both frequency-based and single-echo schemes for these structures as well – except periventricular veins, where there was no significant difference between post-average and frequency-based processing. In contrast, for visibility of OR and SNR of frontal WM, the non-linear filter was ranked as significantly better ( $P<0.001$ ). For OR, the frequency-based scheme was significantly better than both single-echo and post-average schemes. Specific P-values are presented for pair-wise comparisons of processing scheme in Fig. 2.4. Mean ranks of artifact severity are presented (Figure 2.5). In general, the linear mask function results in less severe artifacts, ( $P<0.001$ ); the post-average scheme results in the least severe artifacts. Inter-rater agreement, as assessed by interclass correlation coefficient, was excellent (frontal WM, 0.88; GP, 0.93; OR, 0.85; periventricular veins, 0.82; STN, 0.91; RN, 0.93; artifacts, 0.96).

### 2.3.5 $R_2^*$ measurements

Values of  $R_2^*$  are presented in Table 2.2 as measured in ROI's placed in various structures. For comparative purposes, values reported by Denk and Rauscher<sup>8</sup>, Perán et al.<sup>14</sup>, and Gelman et al.<sup>15</sup> are provided.

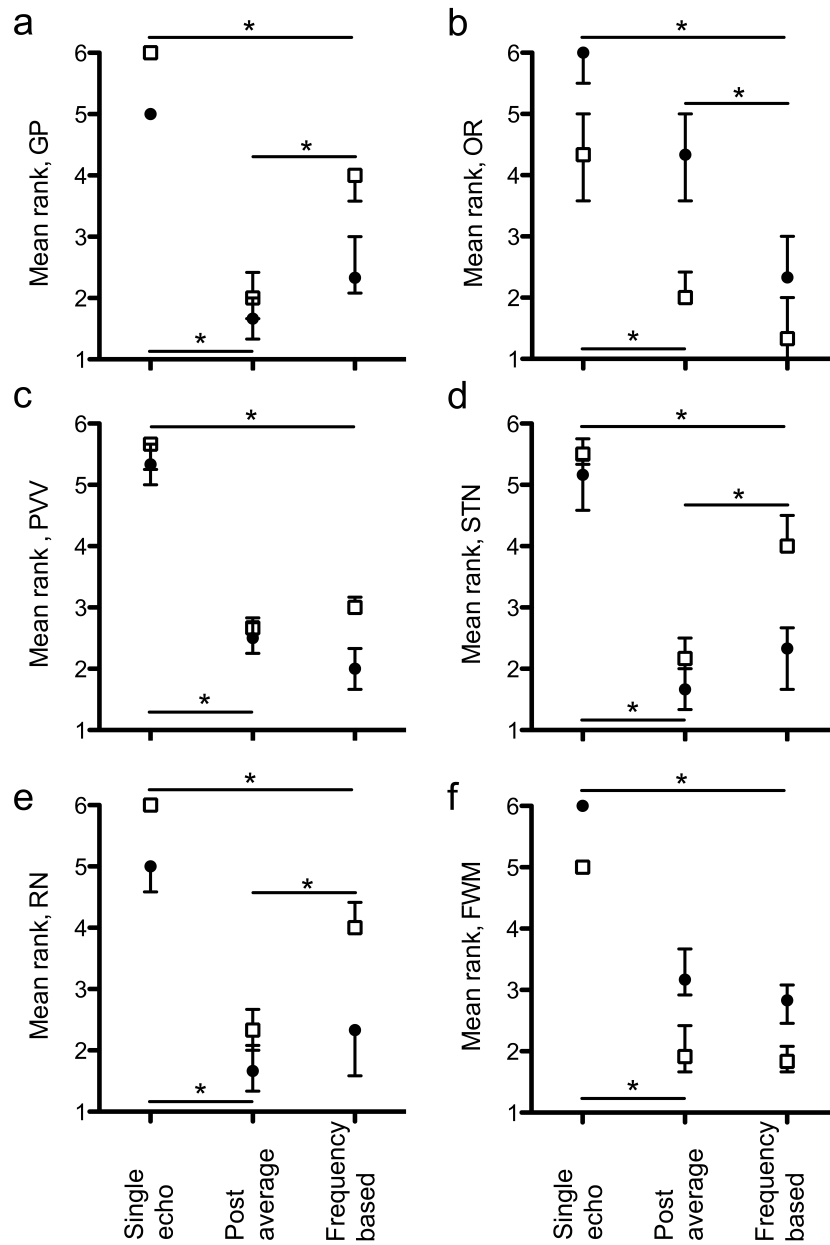


Figure 2.4 Mean rank of visibility for GP (a), OR (b), periventricular veins (PVV) (c), STN (d), RN (e), and mean rank of visual impression of signal to noise ratio for frontal WM (f). Filled black circles: linear mask function; empty squares: non-linear mask function. Points: median; bars: interquartile range (n=10). Illustrated are significant P-values for pairwise comparison of post-processing schemes (\*  $P < 0.05$ ).

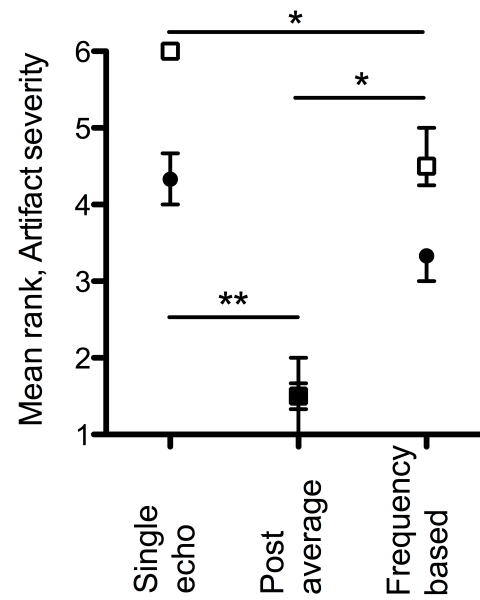


Figure 2.5 Mean rank of artifact severity at sinuses. Filled black circles: linear mask function; empty squares: non-linear mask function. Points: median; bars: interquartile range (n=10). Illustrated are significant P-values for pairwise comparisons of post-processing schemes (\*  $P < 0.05$ , \*\*  $P < 0.01$ ).

Table 2.2  $R_2^*$  measurements

	$R_2^*$ (s <sup>-1</sup> )	Literature Values		
		Denk and Rauscher 2010	Perán et al 2007	Gelman et al 1999 <sup>a</sup>
frontal WM	19.2 ± 1.4	19.7 ± 1.1	18.48 ± 1.5	21.9 ± 1.7
frontal grey matter	13.9 ± 1.0	15.26 ± 2.1	13.30 ± 3.9	17.8 ± 2.1
OR	22.4 ± 2.3	21.1 ± 1.0	--	--
GP	37.7 ± 4.0	--	33.99 ± 3.7	37.8 ± 2.4
putamen	26.1 ± 4.9	27.1 ± 1.0	24.08 ± 2.2	26.1 ± 1.5

Values shown are mean ± standard deviation.

<sup>a</sup>  $R_2^*$  values presented in this column are calculated as the sum of  $R_2$  and  $R_2'$  reported by Gelman et al. Standard deviations presented are root sum of squares of standard deviations of  $R_2$  and  $R_2'$ .

## 2.4 Discussion

This study presents a comparison of (i) different SWI processing schemes, and, (ii) different mask functions, in terms of SWI image quality as assessed by ROI analysis *and* visual rating.

### 2.4.1 SWI optimization

Our choice of  $m$  for implementation in human data was based on optimized values as determined by radiologist raters. This is justified for several reasons: (i) in all cases, rater-optimized values fell within the range of optimal  $m$  predicted by simulation; (ii) raters were instructed to consider the influence of  $m$  not only on veins but also on other structures and noise; (iii) there was excellent inter-rater agreement; and (iv) radiologists are the end-users of SWI. Our optimal  $m$  value for linearly masked single-echo (i.e. conventional) SWI was 6. In contrast, conventional SWI is virtually always implemented with  $m=4$ . This choice is influenced by a seminal SWI study<sup>12</sup> where CNR vs  $m$  was *simulated* for a comparable range of vein phases. As in our simulation, that study found that a lower  $m$  is required for maximum CNR for increasingly large phase. Our raters found a slightly larger value of  $m$  to be most suitable. As our optimizations involved simulation *and* rating, they are more comprehensive than previous efforts. We have endeavored to choose values of  $m$  that are suitable for optimal visibility of a range of structures, however, if re-optimization is required for a specific application, it should be performed by trained raters.



## 2.4.2 In vivo data

For small veins, typical targets of SWI, ROI measurements in vivo agree with those predicted by simulation: optimal CNR can be achieved with the non-linear mask implemented with a frequency-based processing scheme. This conclusion can be extended to CNR of paramagnetic perturbers in general. However, according to visual assessment by trained raters, these same structures are most visible when SWI is performed with the linear mask and post-average processing. This apparent contradiction highlights a discrepancy between CNR and qualitative impression of visibility. While the non-linear filter and frequency-based scheme might independently result in more dramatic contrast (for example, at the edges of GP in Fig. 2.2f), they do not necessarily increase the information content of the image compared to other implementations of multi-echo SWI. Rather, their implementation can result in an image with harsher contrast wherein more subtle structure is less apparent. Images appear ‘burnt-out’ when contrast is too high, with little gradation in the greyscale, which was interpreted by raters as potential loss of information. It appears that maximum contrast should not be the exclusive target when optimizing visibility.

The non-linear mask function and frequency-based processing demonstrated best performance with respect to frontal WM and OR, a diamagnetic perturber, as judged by both quantitative measures in ROI analyses, and visual ranking. For both frontal WM and OR, we do not expect the mean signal in an ROI to change after multiplication with the described mask functions, given their zero or positive frequency, respectively. Therefore,

the improved performance of non-linear mask function and frequency based processing for frontal WM and OR can be attributed to the reduced noise introduced into the image in these regions by these post-processing strategies, given the absence of changes in mean signal or contrast.

One limitation of multi-echo SWI is increased scan time. Fewer echoes or reduced coverage could be used to reduce scan time. Alternatively, if coverage were expanded to allow imaging of the entire supratentorial brain, scan time would be on the order of 20 minutes. In addition to SWI, it is possible to obtain many contrasts from this acquisition, including  $R_2^*$  maps, frequency maps, and quantitative susceptibility maps. Given the high-yield nature of this acquisition, the parameters recommended here are not unreasonable in a clinical setting.

### 2.4.3 $R_2^*$ measurements

Measured values of  $R_2^*$  agree closely with previously reported values. In the case of the GP as well as the putamen, the standard deviations we report are higher than in other papers. This result does not reflect less precise measurements.  $R_2^*$  is approximately linear to iron concentration<sup>6</sup>, which varies considerably with age in these structures<sup>16</sup>. Since this study involved a range of ages, we expect a large variation in iron concentration in basal ganglia structures and the corresponding values of  $R_2^*$ . In white matter and grey matter, our values of standard deviations are intermediate to and smaller than, respectively, previously reported values. Thus, our measurements of  $R_2^*$  have comparable accuracy and precision to previously reported values.

#### 2.4.4 Field inhomogeneity artifacts

Multi-echo SWI processing, in particularly post-average, typically resulted in less severe field inhomogeneity artifacts compared to single-echo SWI. Denk and Rauscher<sup>8</sup> showed that, by employing a filter width that varies with echo time, field inhomogeneity artifacts could be reduced further in post-average processing while preserving contrast elsewhere in the image. To limit the matrix of comparisons in the present study, we elected not to investigate the effects of an adaptive filter, although we expect its use would result in further reduction of these artifacts.

#### 2.4.5 Prospective applications

Ultimately, our recommendation for SWI implementation depends on the desired application and allowed time. Certainly, it is clear that any implementation of multi-echo SWI results in superior images than single-echo SWI.

For radiological use, post-average processing and the linear filter are favored. Given its favored performance for visualizing paramagnetic perturbers, this implementation of multi-echo SWI seems especially well suited to the study of neurodegenerative diseases in which iron deposition is implicated. In addition, this technique might have a role in the study of traumatic brain injury, stroke, and other conditions where abnormalities in vasculature or blood products are involved. One specific diagnostic application is assessing the presence of veins within white matter lesions. At 7 T, this has been demonstrated to be specific to multiple sclerosis<sup>17</sup>, however current techniques at 3 T lack

the sensitivity to delineate such veins. Optimized multi-echo SWI holds promise for reproducing these findings at clinical field strengths.

In this study, volunteers were free of pathology and raters were thus only able to evaluate visibility of normal structure. It is possible that the high contrast, low noise properties of either (or both) frequency-based processing and the non-linear filter may facilitate more rapid detection of very subtle pathology such as microbleeds. Alternatively, while frequency-based, non-linearly filtered SWI may be undesirable for radiological assessment, such an image may be optimal for automated tasks where high contrast and low noise would be favored such as STN segmentation for electrode targeting, computer-based delineation of veins, or registration tasks.

## 2.5 Conclusion

Linearly masked post-average SWI is the recommended implementation of multi-echo SWI for radiological use; however, non-linearly masked frequency-based SWI may have use in computer-based segmentation or registration. A discrepancy between measures of CNR and subjective impressions of visibility was found, highlighting an important caution for SWI optimization.

## 2.6 References

1. Haacke EM, Mittal S, Wu Z, Neelavalli J, Cheng YCN. Susceptibility-weighted imaging: technical aspects and clinical applications, part 1. *AJNR Am J Neuroradiol* 2009;30:19–30.
2. Reichenbach JR, Venkatesan R, Schillinger DJ, Kido DK, Haacke EM. Small vessels in the human brain: MR venography with deoxyhemoglobin as an intrinsic contrast agent. *Radiology* 1997;204:272–277.
3. Sehgal V, Delproposto Z, Haddar D, et al. Susceptibility-weighted imaging to visualize blood products and improve tumor contrast in the study of brain masses. *J Magn Reson Imaging* 2006;24:41–51.
4. Haacke EM, Makki M, Ge Y, et al. Characterizing iron deposition in multiple sclerosis lesions using susceptibility weighted imaging. *J Magn Reson Imaging* 2009;29:537–544.
5. Wu Z, Mittal S, Kish K, Yu Y, Hu J, Haacke EM. Identification of calcification with MRI using susceptibility-weighted imaging: a case study. *J Magn Reson Imaging* 2009;29:177–182.
6. Yao B, Li TQ, Gelderen P, Shmueli K, de Zwart JA, Duyn JH. Susceptibility contrast in high field MRI of human brain as a function of tissue iron content. *Neuroimage* 2009;44:1259–1266.
7. Brainovich V, Sabatini U, Hagberg GE. Advantages of using multiple-echo image combination and asymmetric triangular phase masking in magnetic resonance venography at 3 T. *Magn Reson Imaging* 2009;27:23–37.
8. Denk C, Rauscher A. Susceptibility weighted imaging with multiple echoes. *J Magn Reson Imaging* 2010;31:185–191.
9. Casciaro S, Bianco R, Franchini R, Casciaro E, Conversano F. A new automatic phase mask filter for high-resolution brain venography at 3 T: theoretical background and experimental validation. *Magn Reson Imaging* 2010;28:511–519.
10. Quinn MP, Klassen LM, Gati JS, Menon RS. Frequency-based Multi-echo Susceptibility Weighted Imaging. In *Proceedings of the 20th Annual Meeting of ISMRM, Melbourne, Australia, 2012*. p. 1062.
11. Noll DC, Nishimura DG, Macovski A. Homodyne detection in magnetic resonance imaging. *IEEE Trans Med Imaging* 1991;10:154–163.

12. Haacke EM, Xu Y, Cheng YC, Reichenbach JR. Susceptibility weighted imaging (SWI). *Magn Reson Med* 2004;52:612–618.
13. Reichenbach JR, Venkatesan R, Yablonskiy DA, Thompson MR, Lai S, Haacke EM. Theory and application of static field inhomogeneity effects in gradient-echo imaging. *J Magn Reson Imaging* 1997;7:266–279.
14. Peran P, Hagberg G, Luccichenti G, et al. Voxel-based analysis of R2\* maps in the healthy human brain. *J Magn Reson Imaging* 2007;26:1413–1420.
15. Gelman N, Gorell JM, Barker PB, et al. MR imaging of human brain at 3.0 T: preliminary report on transverse relaxation rates and relation to estimated iron content. *Neuroradiology* 1999;210:759–767.
16. Hallgren B, Sourander P. The effect of age on the non-haemin iron in the human brain. *J Neurochem* 1958;3:41–51.
17. Tallantyre EC, Dixon JE, Donaldson I, et al. Ultra-high-field imaging distinguishes MS lesions from asymptomatic white matter lesions. *Neurology* 2011;76:534–539.

### 3 Metrics of internal jugular vein anatomy obtainable from time of flight magnetic resonance venography: Applicability to chronic cerebrospinal venous insufficiency

#### 3.1 Introduction

Recently, a role for structural and functional abnormalities of intra- and extra-cranial veins in the pathogenesis of multiple sclerosis (MS) has been proposed<sup>1-3</sup>. This so-called chronic cerebrospinal venous insufficiency (CCSVI) is reported to involve occlusion of major veins, frequently one or both of the internal jugular veins (IJVs)<sup>3</sup>. CCSVI has motivated some patients to seek out endovascular treatments, despite growing doubt that CCSVI in MS exists at all<sup>4</sup>.

A diagnosis of CCSVI requires extra-cranial and trans-cranial color-coded Doppler sonography<sup>5</sup>. These tools are foreign to the conventional study of MS. The vast majority of imaging for the diagnosis and monitoring of MS involves MRI<sup>6</sup>. Doppler sonography is well suited for visualizing and quantifying blood flow, and is relatively portable and inexpensive compared to MRI, but obviously does not demonstrate central nervous system lesions. For logistical reasons, the addition of an extensive sonography study is generally not warranted for MS investigations. If however, imaging of the draining cerebral veins is desired, MRI can instead be used to produce three-dimensional venograms of high quality and is capable of determining the presence of structural abnormalities<sup>7,8</sup>. Susceptibility weighted imaging (SWI) is capable of visualizing intra-

cranial veins with sizes on the order of the voxel dimensions, but is not appropriate for visualizing major intra- or extra-cranial veins. Alternatively, time-of-flight (TOF) MR venography (MRV), which enjoys clinical acceptance for intra-cranial venography<sup>9</sup> and can be used for extra-cranial venography, does not require administration of a contrast agent and is an acceptable addition to research protocols on the criteria of safety for control subjects.

The objective of this study is to classify metrics of IJV anatomy (CSA) obtainable from TOF venograms. Specifically, we present strategies for the measurement of these metrics, as well as expected reproducibility in healthy subjects. The results are discussed in the context of suitability of TOF MRV for the study of CCSVI in MS.

## 3.2 Methods

### 3.2.1 MR imaging

This study was approved by the institutional research ethics board. Informed written consent was obtained from all participants. Nine healthy volunteers (6 females, mean age $\pm$ standard deviation = 25 $\pm$ 7 years) with no history of neurological or vascular disease were recruited. Volunteers were scanned on a 3T MR scanner (TIM Trio, Siemens Medical Solutions, Erlangen, Germany) with a 12-channel head coil and 4-channel neck coil. Two-dimensional MR venography was performed in the axial plane using the following parameters: TR/TE = 39/4.99 ms; flip angle, 50°; slice thickness, 2 mm; gap, -0.4 mm; matrix, 640 x 303; field of view, 400 mm x 250 mm; number of slices, 110; GRAPPA acceleration factor, 2. An inferior saturation slab was used to null arterial



signal. This sequence was performed three times for each volunteer. Between scans, volunteers were instructed to rotate their head and neck and then return to a comfortable centerline position. This paradigm was employed to introduce variation between scans similar to what might be observed in serial scans within a longitudinal study.

### 3.2.2 Measurements of CSA

Left and right IJVs were segmented in each slice using a semi-automated 2D region-growing tool in OsiriX version 3.9.4 32 bit (Geneva, Switzerland). Specifically, a seed point was manually placed within the IJVs on each slice. Subsequently, a region of interest containing all neighboring pixels with intensities greater than a user-defined segmentation threshold was generated. The same threshold was used for all segmentations.

Trends in CSA and its reproducibility were assessed at three positions of interest along each IJV that were commonly observed in volunteers: (I) a local minimum in area near the transverse process of the first cervical vertebra (C1), (II) a local maximum in area where the common facial vein enters the IJV, and, (III) a local maximum in area at the inferior bulb of the IJV. Positions were chosen independently for each volume; no co-registration was performed. The average CSAs of the right and left IJVs were also computed by taking the mean of CSA of all slices between the sigmoid sinus and either the confluence of the IJV with the subclavian vein or wherever the IJV was obscured by respiratory/flow motion. Intra-subject variation in CSA at each position of interest and in

average CSA on each side was quantified as the standard deviation (SD) and the coefficient of variation (CV) of the three measurements for each volunteer.

### 3.2.3 Statistical analyses

Differences in left versus right IJV anatomy were assessed at the three positions of interest and for the average area along the entire vessel. The mean values (across the three acquisitions) of CSA at each position of interest as well as average CSA were calculated for each volunteer. Subsequently, these four left-right pairs of metrics were independently compared using the Wilcoxon signed-rank test. Statistical analyses were performed in GraphPad Prism version 5.0 (GraphPad Software, La Jolla, California). A two-sided P-value of 0.05 was deemed significant for all tests.

## 3.3 Results

A representative maximum intensity projection from a single volunteer is shown (Figure 3.1a). The three positions of interest in this study are clearly visible and are identified with Roman numerals for the right IJV. Vascular signal is decreased in the inferior-most slices, as is expected due to turbulent flow and respiratory motion. From the same acquisition, representative axial images are presented in Fig. 3.1b (superior-most) through Fig. 3.1d (inferior-most). The right IJV is clearly larger in caliber than the left.

At each of positions I, II, and III, arithmetic means and SDs of area measurements were calculated for each volunteer (for left and right IJVs separately); CVs were calculated for each subject at each position from those metrics as  $(SD)/(\text{mean}) \times 100\%$ . Additionally, in

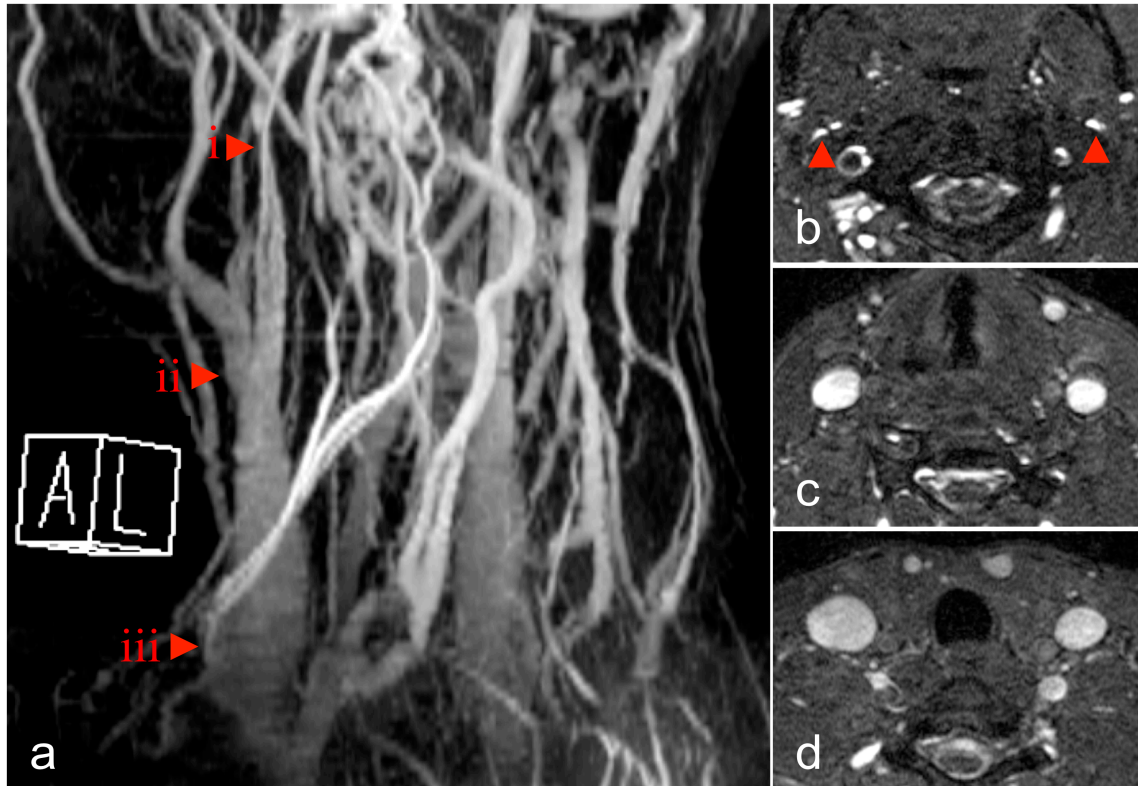


Figure 3.1 Representative time of flight venogram. Maximum intensity projection is shown in (a), where the levels of the three positions interrogated in this study are approximately identified with arrows. Position I is a minimum in cross sectional area (CSA) near the first cervical vertebra (C1), position II is a local maximum in CSA at the merge with the common facial vein, and position III is a local maximum in CSA at the inferior bulb. Both internal jugular veins are visible in the representative axial slices in (b) through (d). At the narrowing in the IJV near C1 shown in (b), the IJVs are highlighted with arrows. In (c) and (d), the subject's right IJV (on the reader's left) is visibly of larger caliber than the left.

each subject, a single value (for each of left and right IJVs) of mean of average CSA was measured as the mean of the three average CSA measurements, as was SD of these three measurements and, subsequently, CV. As measured from these metrics in all volunteers, grand mean CSA (mean of means) and root-mean-square (rms) SD and rms CV are tabulated in Table 3.1 for left and right IJVs.

Table 3.1 Summary of IJV CSA metrics and reproducibility.

	Left	Right
<b>Position I</b>		
grand mean (mm <sup>2</sup> )	17.8	29.1
rms SD (mm <sup>2</sup> )	2.7	3.5
rms CV (%)	28	20
<b>Position II</b>		
grand mean	75.1	98.1
rms SD	5.0	7.5
rms CV	7	8
<b>Position III</b>		
grand mean	82.9	123.8
rms SD	4.0	8.2
rms CV	6	8
<b>Average CSA</b>		
grand mean	44.9	66.8
rms SD	2.0	4.4
rms CV	5	7

It is readily clear that these metrics of IJV CSA tend to be larger on the right than the left. This trend was found to be significant for the average area ( $P=0.008$ ) and for position III: the local maximum at the facial vein ( $P=0.02$ ). A trend was apparent at the other two positions investigated: the local minimum near C1 ( $P=0.07$ ) and the local maximum at the inferior bulb ( $P=0.06$ ).

### 3.4 Discussion

The objective of this study was to characterize metrics of IJV anatomy obtainable from TOF MRV that might be used for evaluation of CCSVI in MS. Previous studies have investigated the suitability of TOF MRV for CCSVI using qualitative scales that vary from study to study. For example, in previous studies, IJVs have been dichotomously classified as stenotic or normal<sup>10</sup>, rated from normal to severely narrowed on a 4-point ordinal scale<sup>11</sup>, or categorized in terms of morphology<sup>12</sup>. This makes direct comparison of results challenging. To our knowledge, ours is the first work to rigorously study a *quantitative* metric (CSA) using a semi-automated area measurement tool. Advantages of such an approach are that CSA is a continuous (as opposed to dichotomous or categorical) variable, and logically one would anticipate such measurements to be associated with less ambiguity, increased reproducibility, and less dependence on the rater than previously implemented methods.

In general, we find that the right IJV is of consistently larger caliber than the left, in line with previous studies<sup>13</sup>. It is imperative that future studies of CCSVI consider normal left/right differences in order to avoid false positive for occlusion, especially on the left

side. Additionally, a minimum near C1 is present in all volunteers. Indeed, we report a grand mean CSA of the minimum near C1 of the left and right IJV to be approximately  $20 \text{ mm}^2$  and  $30 \text{ mm}^2$ , the former being considerably smaller than the ostensibly pathological CSA described by Zamboni and colleagues of  $30 \text{ mm}^2$ <sup>3</sup>. A recent study of CCSVI in MS notes that as many as 78% of MS patients have IJV “stenosis” at the C1–2 level when interrogated with MRV<sup>11</sup>. That study did not have a control wing: the findings of the present study imply this narrowing may in fact be normal, as was reported by another recent study<sup>14</sup>.

While the volunteers in this study were free of pathological narrowing, the minimum in CSA of the IJV near C1 can serve as a model of stenosis. At this position, we find that the rms SD of CSA is on the order of  $3 \text{ mm}^2$ . Stenosis of the IJV has been defined as CSA less than  $30 \text{ mm}^2$ <sup>3</sup>: this is an order of magnitude larger than our expected measurement error. Our observations favor a conclusion that TOF MRV is a sufficiently reproducible method by which stenoses in CCSVI can be quantitatively studied without resorting to an additional modality such as ultrasound. This conclusion is in line with a previous study that finds TOF MRV to have modest image-reimage stability for qualitative monitoring of morphologic features of the IJV<sup>15</sup>. In particular, measurements of average CSA (i.e. along the entire vessel) are the most reproducible of all metrics studied here ( $CV \leq 7\%$ ); classification of this metric in MS patients is required in the future. Average CSA measurements have the additional benefit that no co-registration is required to guarantee perfect alignment. Other authors have investigated the caliber of IJVs after dividing the vessel into segments, for example, into lower, mid, and upper

thirds<sup>16</sup>, or lower and upper halves<sup>10</sup>. While such an approach was not described in this study, it is certainly possible given that we measure CSA for all slices of the IJVs. This would simply involve defining segments to be studied, and averaging the CSA of all slices within each segment.

To our knowledge, no previous studies have attempted to quantify intra-subject reproducibility of IJV CSA measured with ultrasound, so a direct comparison between modalities is not possible. However, at least three advantages of MRI over ultrasound are noteworthy. First, CCSVI imaging with ultrasound requires extensive training<sup>5</sup>, the absence of which can dramatically affect diagnostic outcomes<sup>17</sup>. Second, even mild pressure exerted by the ultrasound probe inevitably alters the vein diameter, likely leading to false-positive results<sup>14</sup>. Third, maximum intensity projections of MRV data allow simultaneous visualization of the entire three-dimensional cervical venous vasculature (ex. Fig. 3.1a).

Advantages of TOF over contrast enhanced MRV are two-fold: first, the former does not require the administration of a contrast agent, making its use more acceptable in studies involving a control wing; and second, in-plane resolutions of TOF MRV are typically higher than for contrast enhanced MRV, allowing for more precise measurements of CSA and more confident visualization of stenosis.

TOF MRV can be used to monitor morphological features of the cervical venous vasculature, whereas both anatomy and flow are of interest in CCSVI. Additional studies are required to identify an optimal MR strategy by which flow may be interrogated,

although a recent study suggests a strong association between reductions in IJV caliber and reductions in flow<sup>10</sup>.

Additional analyses of the potential dependence of CSA on acquisition parameters and segmentation threshold would be useful. Despite this, the proposed methodology is well suited for quantitative comparisons between patients and healthy controls, assuming the same parameters, including segmentation threshold, are used for all groups.

This study was not without limitations. The paradigm employed to introduce variation between serial scans – readjustment of head and neck – was relatively simple compared to what might be expected between scans on separate days or separate scanners. Additionally, a number of factors that were not accounted for might introduce variation in caliber of IJVs, including hydration level, clothing, and how tightly the subject is packed into the imaging coil. Ultimately, the present study classifies the contribution to CSA variation due to measurement error. Comprehensive evaluations in a patient cohort of scan-rescan stability of TOF MRV for measurement of IJV mean CSA are presented in Chapter 4 of this thesis.

### 3.5 Conclusion

We find that TOF MRV can be used for robust quantitative assessments of IJV anatomy. In healthy controls, we find that the right IJV is of larger caliber than the left, an important consideration for CCSVI studies. A characteristic narrowing of the IJV near C1 is present in all volunteers and must not be confused with pathological stenosis in patients. We recommend that these metrics of IJV anatomy, in particular average CSA,



be classified in patients with MS in order to evaluate the presence of a structural substrate for CCSVI.

### 3.6 References

1. Zamboni P. The big idea: iron-dependent inflammation in venous disease and proposed parallels in multiple sclerosis. *J R Soc Med* 2006; **99**:589-593.
2. Zamboni P, Menegatti E, Bartolomei I et al. Intracranial venous haemodynamics in multiple sclerosis. *Curr Neurovasc Res* 2007; **4**:252-258.
3. Zamboni P, Galeotti R, Menegatti E et al. Chronic cerebrospinal venous insufficiency in patients with multiple sclerosis. *J Neurol Neurosurg Psychiatry* 2009; **80**:392-399.
4. Bagert BA, Marder E, Stuve O. Chronic cerebrospinal venous insufficiency and multiple sclerosis. *Arch Neurol* 2011; **68**:1379-1384.
5. Zamboni P, Morovic S, Menegatti E, Viselner G, Nicolaidis AN. Screening for chronic cerebrospinal venous insufficiency (CCSVI) using ultrasound - Recommendations for a protocol. *Int Angiol* 2011; **30**:571-597.
6. Polman CH, Reingold SC, Banwell B et al. Diagnostic criteria for multiple sclerosis: 2010 revisions to the McDonald criteria. *Ann Neurol* 2011; **69**:292-302.
7. Rollins N, Ison C, Reyes T, Chia J. Cerebral MR venography in children: comparison of 2D time-of-flight and gadolinium-enhanced 3D gradient-echo techniques. *Radiology* 2005; **235**:1011-1017.
8. Lettau M, Sartor K, Heiland S, Hahnel S. 3T high-spatial-resolution contrast-enhanced MR angiography of the intracranial venous system with parallel imaging. *AJNR Am J Neuroradiol* 2009; **30**:185-187.

9. Liauw L, van Buchem MA, Spilt A et al. MR angiography of the intracranial venous system. *Radiology* 2000; **214**:678-682.
10. Haacke EM, Feng W, Utraiainen D et al. Patients with Multiple Sclerosis with Structural Venous Abnormalities on MR Imaging Exhibit an Abnormal Flow Distribution of the Internal Jugular Veins. *J Vasc Interv Radiol* 2012; **23**:60-68.e3.
11. Zaharchuk G, Fischbein NJ, Rosenberg J, Herfkens RJ, Dake MD. Comparison of MR and contrast venography of the cervical venous system in multiple sclerosis. *AJNR Am J Neuroradiol* 2011; **32**:1482-1489.
12. Dolic K, Marr K, Valnarov V et al. Intra- and extraluminal structural and functional venous anomalies in multiple sclerosis, as evidenced by 2 noninvasive imaging techniques. *AJNR Am J Neuroradiol* 2012; **33**:16-23.
13. Lobato EB, Sulek CA, Moody RL, Morey TE. Cross-sectional area of the right and left internal jugular veins. *J Cardiothorac Vasc Anesth* 1999; **13**:136-138.
14. Mayer CA, Pfeilschifter W, Lorenz MW et al. The perfect crime? CCSVI not leaving a trace in MS. *J Neurol Neurosurg Psychiatry* 2011; **82**:436-440.
15. Zivadinov R, Galeotti R, Hojnacki D et al. Value of MR Venography for Detection of Internal Jugular Vein Anomalies in Multiple Sclerosis: A Pilot Longitudinal Study. *AJNR Am J Neuroradiol* 2011; **32**:938-946.
16. McTaggart RA, Fischbein NJ, Elkins CJ et al. Extracranial venous drainage patterns in patients with multiple sclerosis and healthy controls. *AJNR Am J Neuroradiol* 2012; **33**:1615-1620.
17. Menegatti E, Genova V, Tessari M et al. The reproducibility of colour Doppler in chronic cerebrospinal venous insufficiency associated with multiple sclerosis. *Int Angiol* 2010; **29**:121-126.

## 4 Increased deep grey matter iron is present in clinically isolated syndromes

### 4.1 Introduction

In multiple sclerosis (MS), abnormal iron deposition within subcortical nuclei<sup>1</sup> and at the periphery of some white matter lesions<sup>2</sup> has been known to exist for decades. However, this evidence has been derived from cross-sectional imaging studies, or from ex vivo work, and thus does not establish whether the observed iron accumulation was a cause or consequence of pathology in MS.

The presence of iron in MS has generally been thought to be *secondary* to an autoimmune response that either affected normal metabolism of brain iron<sup>3</sup> or induced extravasation of hemoglobin-containing red blood cells into the central nervous system (CNS) parenchyma<sup>2</sup>. However, it has also been recognized that increased brain iron could directly promote oxidative damage at many levels in the cell<sup>4</sup>. The disease stage at which iron accumulation is detected might provide insight into iron's role (or roles) in MS.

In this work, we performed quantitative MRI investigations of brain iron in patients with a clinically isolated syndrome (CIS) who are at high risk of being diagnosed with MS in order to determine if iron is present in early MS and if so, to determine its spatial distribution. Using a well-validated surrogate MRI-derived metric of iron (the effective transverse relaxation rate,  $R_2^*$ )<sup>5</sup>, we evaluated iron in the brains of CIS patients on a voxel-by-voxel basis. For clusters of voxels where differences in  $R_2^*$  (and thus potentially

Reprinted from Multiple Sclerosis and Related Disorders, DOI: 10.1016/j.msard.2013/06/017, Quinn, MP, Gati, JS, Klassen, LM, Lee, DH, Kremenchutzky, M, Menon, RS. Increased deep grey matter iron is present in clinically isolated syndromes, ©2013, with permission from Elsevier.

iron) were detected between groups, mean  $R_2^*$  was regressed against a number of disease status-related parameters.

To further explore the observed increases in iron in deep grey matter in CIS, we measured the caliber of the major extra-cranial veins. These vessels have been implicated in a theory that proposes iron accumulation occurs in the brains of MS patients as a consequence of abnormal venous drainage of the CNS<sup>6</sup>. According to this chronic cerebrospinal venous insufficiency (CCSVI) theory, CNS iron, derived from extravasated red blood cells, mediates damage as a potent chemo-attractant for pathogenic cellular effectors. While an association of MS lesions with small venules has been observed since the earliest descriptions of the disease<sup>7</sup>, the abnormal venous drainage theory lacks independent verification. Using magnetic resonance venography (MRV) and offline segmentation, we measured the mean cross-sectional areas (CSAs) of the internal jugular veins (IJVs) in patients and healthy controls. Subsequent correlations between IJV CSA and mean  $R_2^*$  in regions where significantly increased iron was detected allowed for assessment of any association between increases in iron and IJV caliber.

Ultimately, the main focus of the present study – differences in brain iron between healthy controls and patients with clinically isolated syndromes – need not be coupled with the topic of CCSVI. Indeed, while the support for a pathogenic role for venous abnormalities in MS becomes increasingly tenuous, the timeline of *well-established* iron accumulation in MS remains an unresolved, yet important issue for addressing potentially early pathological changes in MS patients.

## 4.2 Materials and Methods

### 4.2.1 Subject recruitment

Twenty-two CIS patients were prospectively recruited from the MS clinic in the London Health Sciences Centre. Inclusion criteria were: (1) a single clinical attack indicative of risk for developing MS according to McDonald's 2010 criteria<sup>8</sup>, (2) less than one year from clinical presentation, (3) 18 to 50 years of age, (4) no contraindication for serial MRI scanning, (5) ability to provide informed consent. Sixteen healthy controls were recruited from the general population. Cohort demographics are provided (Table 4.1). Informed, written consent was obtained from all study participants. This study was approved by the Health Sciences Research Ethics Board of The University of Western Ontario.

Table 4.1 Cohort demographics

	Controls	Patients	P
n	16	22	--
Age [mean (SD)]	38.6 (7.6)	36.7 (7.6)	0.44 <sup>a</sup>
females	13	17	1.00 <sup>b</sup>
EDSS [median (95% CI)]	--	1.0 (0.0,1.125)	--
Disease duration [mean (SD)] days	--	235 (183)	--

<sup>a</sup>Two-sided t-test

<sup>b</sup>Fisher's exact test

## 4.2.2 MR imaging

All study participants were imaged on a 3T MRI system (TIM Trio, Siemens Medical Solutions, Erlangen, Germany). Using a 32-channel head coil, the following contrasts were acquired. Axial FLAIR: TE/TI/TR = 136/2850/15000 ms; voxel size = 1x1x3 mm<sup>3</sup>. Axial T2-weighted turbo spin echo: TE/TR = 99/5100 ms; voxel size = 1x1x3 mm<sup>3</sup>. T1-weighted (T1w) three-dimensional MPRAGE: TI/TE/TR = 900/6.9/2060 ms; voxel size = 0.5x0.5x1.0 mm<sup>3</sup>. Three-dimensional multi-echo gradient echo (GRE): TE<sub>1</sub>/ΔTE/TR = 10/7/52 ms (6 echoes). Three GRE volumes were acquired, with approximately 15 to 20 mm of overlap between adjacent slabs, providing full brain coverage including the cerebellum. With a 12-channel head coil and 4-channel neck coil, two-dimensional time of flight (TOF) MRV was performed in the axial plane using the following parameters: TE/TR = 5/50 ms; voxel size = 0.8x0.6x2.0 mm<sup>3</sup>; 0.4 mm overlap between slices; flip angle = 50°. An inferior saturation slab was used to null arterial signal.

## 4.2.3 Multi-echo gradient echo processing

Image processing was performed in MATLAB (The Mathworks, Natwick, MA), FSL (FMRIB, Oxford, UK), and OsiriX (Geneva, Switzerland).

To quantify iron, maps of  $R_2^*$  were calculated for each multi-echo gradient echo slab via a voxel-wise curve fit to a single exponential decay curve. Mean magnitude from each GRE slab was registered to the T1w volume using the FSL tool FLIRT. Registration parameters were then applied to the  $R_2^*$  slabs. Co-registered  $R_2^*$  slabs were concatenated by arithmetic averaging of overlapping voxels.

For each volunteer, the T1w volume was then registered to the MNI\_152 1x1x1 mm<sup>3</sup> template provided with FSL. These registration parameters were then applied to the concatenated  $R_2^*$  volume. The  $R_2^*$  volume, now in the space of the template, was blurred using a 3D Gaussian kernel (full-width at half maximum, 6 mm) and down sampled to 3x3x3 mm<sup>3</sup>.

#### 4.2.4 Measurements of CSA

From the TOF volumes, the right and left IJVs were segmented in each slice using a semi-automated region-growing tool in OsiriX, where a seed point was first placed within the IJV. Subsequently, all neighbouring pixels with intensities greater than a user-defined threshold (constant for all segmentations) were included in an ROI, the area of which was reported. For each participant, mean CSA was calculated for both right and left IJVs along their extent from the sigmoid sinus to the confluence of the IJV with the subclavian vein, generally at the level of the first thoracic vertebra. Mean CSA of both right and left IJVs were compared between patients and controls using two-sided t-tests or Mann-Whitney U test, depending on distribution of data as assessed with Shapiro-Wilk testing, using SPSS version 20.0 (IBM, Armonk, NY). Since the two IJVs form a downstream bifurcation from a common major draining cerebral vein, we combined the CSAs of the two IJVs together as the best indicator of a venous return anomaly from the brain. To establish the test-retest reproducibility of the CSA measurements, IJVs were segmented and measured in MRVs from a follow-up scan, nominally 4 months later. Additionally, correlations between right, left, and total CSA with EDSS and disease duration were performed.

#### 4.2.5 Lesion segmentation

Lesions were segmented on FLAIR via seed-point-based semi-automated region growing, as well as manually where the semi-automated method did not yield accurate borders. FLAIR volumes were registered to the  $1 \times 1 \times 1 \text{ mm}^3$  template; these registration parameters were applied to the lesion masks. Lesion masks were then blurred as above, downsampled to  $3 \times 3 \times 3 \text{ mm}^3$  to be matched to the aforementioned  $R_2^*$  volumes. All values in the blurred masks greater than a threshold of 0.05 (determined by visual inspection to be suitable) were assigned as lesion.

#### 4.2.6 Image-based general linear model (GLM) analysis

A modified age-adjusted t-test was performed for each voxel in the co-registered  $3 \times 3 \times 3 \text{ mm}^3$   $R_2^*$  volumes between patients and controls as follows. The change in  $R_2^*$  with age due to normal aging was estimated by linear regression of  $R_2^*$  against age in the healthy control cohort. This effect was subsequently subtracted from all subjects. Specifically, in a given subject, for each voxel, the rate of change of  $R_2^*$  with age (as estimated in all healthy controls) was multiplied by the subject's age. This value was then subtracted from the measured value of  $R_2^*$  in that voxel to 'adjust' it for age. A two-sided t-test was then performed for each voxel in the age-adjusted volumes. Data points coming from lesions were excluded.

This is highly similar to what is done in an age-adjusted t-test (i.e. a t-test with age as a covariate), except that the effect of the covariate was measured only on one study group (healthy controls), not both groups. We felt this to be appropriate given that the rate of



change of  $R_2^*$  with age in patients is possibly influenced by disease duration. Therefore, the most reliable way to estimate the effect of age *alone* on  $R_2^*$  is to calculate the covariate coefficients in healthy controls. A potential limitation of this methodology is that we have a relatively small group of controls from which to estimate the coefficients; however, we do have a relatively large and well-sampled range of ages (from early 20's to late 40's), which is arguably of equal importance. In the future, this study's methodology will be extended to a larger group of subjects and we anticipate improved accuracy of this method at such time.

Significant clusters were identified as groups of >10 edge-wise neighboring significant voxels after controlling the false discovery rate at 10%. Anatomically similar clusters were grouped to select ROIs. In patients, mean value of  $R_2^*$  in each group of clusters as regressed against a number of parameters, including age, extended disability status scale (EDSS), disease duration, and IJV CSA. For correlations involving non-normally distributed parameters, as determined by Shapiro-Wilk testing, Spearman correlation was used. Otherwise, Pearson correlation was employed.

After a mean clinical follow-up time of 11.2 months after recruitment into the study, 8 CIS patients had converted to MS. To investigate if  $R_2^*$  differences (potentially iron) at *baseline* relate to subsequent conversion to clinically definite MS, mean age-adjusted  $R_2^*$  levels in the ROIs identified above were compared between healthy controls, patients who had not yet converted from CIS, and patients who had converted to clinically definite MS. Comparisons were made using a one-way ANOVA and Tukey post-hoc testing.

### 4.2.7 Lesion $R_2^*$ analyses

Average lesion  $R_2^*$  was calculated for each patient using co-registered lesion masks and  $R_2^*$  volumes at a resolution of  $1 \times 1 \times 1 \text{ mm}^3$ , before blurring. Average lesion  $R_2^*$  was correlated against the clinical/imaging parameters.

## 4.3 Results

### 4.3.1 $R_2^*$ depends on age in the cortex, putamen, edge of lateral ventricles

Representative slices are shown in the first column of Figure 4.1 of the results of age-correlation, where regression coefficients are overlaid on the template. Expected trends due to iron accumulation with age are seen:  $R_2^*$  increases with age in various cortical areas, and at an increased rate in the putamen and red nucleus (arrows in Fig. 4.1c, d respectively). Moreover, negative coefficients were found in significant clusters at the lateral ventricles (arrows in Fig. 4.1b) and edge of the brain, consistent with age-related atrophy as cerebrospinal fluid has a lower  $R_2^*$  than grey and white matter.

### 4.3.2 In patients, $R_2^*$ is decreased in normal appearing white matter (NAWM) and increased in deep grey matter and cortical areas

In the second column of Fig. 4.1, clusters are shown at positions where the age-adjusted difference in  $R_2^*$  between patients and controls was significant. Positive values indicate

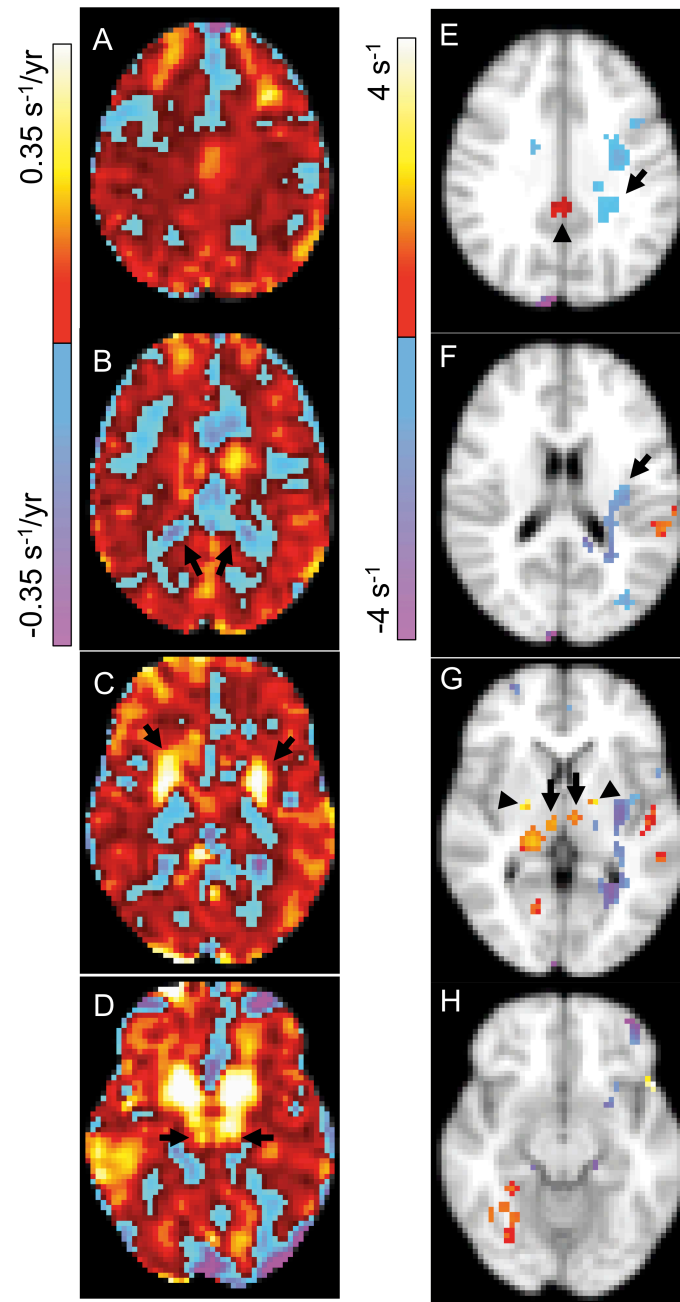


Figure 4.1 Representative results from voxel-wise age-adjusted t-tests. Coefficients for age (a-d) as estimated in healthy controls reveal  $R_2^*$  increases with age in various cortices, putamen, and red nuclei; as well,  $R_2^*$  decreases with age around the edges of the lateral ventricles and brain. Age-adjusted differences between patients and controls are shown in the second column (e-h), where lesions have been excluded. Patients have decreased  $R_2^*$  in deep white matter as well as increased  $R_2^*$  in the bilateral thalamus (g), right pulvinar (g), and some cortices, including the posterior cingulate (e). The color look-up table at left of a and b applies to the first column. The color look-up table at the left of e and f applies to the second column.

increased  $R_2^*$  (putative iron) in patients. In some white matter regions, patients have decreased  $R_2^*$  (arrows in Fig. 4.1e, f). The presence of clusters of reduced  $R_2^*$  in white matter despite exclusion of lesions indicates these significant changes between patients and controls are not due to classical demyelination alone. Moreover, patients have increased  $R_2^*$  in the medial thalamus (arrows in Fig. 4.1g), in a region encompassing the right pulvinar, and in the bilateral globus pallidus (arrowheads in Fig. 4.1g), and, while not shown here, the right putamen. At several positions within cortical grey matter, patients have significantly increased  $R_2^*$ , for example, within a significant cluster in the posterior cingulate (arrowhead in Fig. 4.1e).

#### 4.3.3 Mean CSA of the right IJV is reduced in patients compared to controls

Metrics of mean IJV CSA are tabulated (Table 4.2) for controls and patients. No differences between patients and controls were detected for the left IJV. The mean CSA of the right IJV was significantly smaller for patients than controls. While not a significant difference, there was a trend ( $P < 0.10$ ) for the total CSA to be smaller in patients than in healthy controls. There were no significant correlations for any CSA metric (right, left, or sum) with age (evaluated over patients *and* controls), EDSS, or disease duration (evaluated over patients only). A Bland-Altman difference plot is shown (Figure 4.2), pooled for all subjects, to establish test-retest stability of total CSA. Neither the bias of the difference between baseline and follow-up measurements, nor the correlation between axes is significantly different from zero, which suggests IJV CSA is well reproducible.

Table 4.2 Mean cross-sectional areas of internal jugular veins

	Controls (n=16)	Patients (n=22)	
	Mean (SD) [mm <sup>2</sup> ]	Mean (SD) [mm <sup>2</sup> ]	P
Left	54.2 (27.8)	52.6 (25.0)	0.679 <sup>a</sup>
Right	96.0 (31.5)	65.7 (28.6)	<b>0.004</b>
Total (sum)	148.5 (42.2)	123.3 (39.2)	0.066

Two sided t-test, except for <sup>a</sup> where Mann-Whitney U test was used.

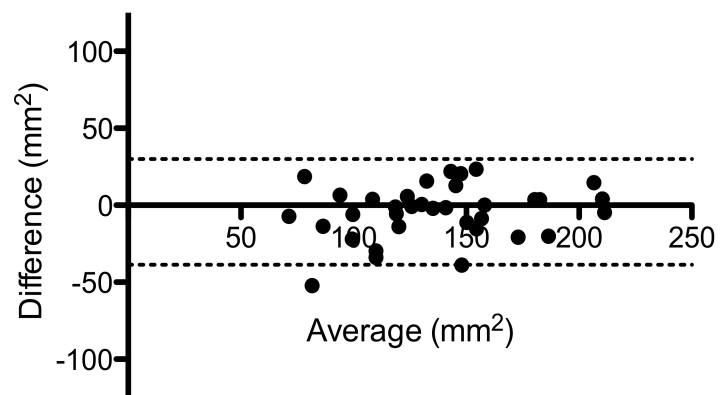


Figure 4.2 Bland-Altman difference plot of baseline and 4 month follow-up of total IJV CSA, pooled for all subjects. The dashed horizontal lines represent the 95% confidence intervals of the bias of the difference between the two measurements. This bias, as well as the correlation between difference and average, is not significantly different from zero.

#### 4.3.4 Correlations of $R_2^*$ differences with clinical and imaging parameters

Anatomically similar significant clusters were grouped into categories, as presented (Table 4.3). Mean  $R_2^*$  was measured for all such clusters within a category and correlations with disease status parameters were made in patients. Significant P-values and correlation coefficients are listed (Table 4.3). Of note, for no ROI was a significant correlation with IJV CSA detected.

#### 4.3.5 Baseline $R_2^*$ levels do not differ between MS and unconverted CIS

Figure 4.3 presents  $R_2^*$  values in the ROIs identified in Table 4.3, as measured at baseline, for: healthy controls, unconverted CIS patients, and MS patients (i.e. patients who had CIS at baseline and have since received a diagnosis of MS). In no case was there a significant difference between CIS and MS patients; from visual inspection the distribution of  $R_2^*$  values is highly similar for both patient groups for all ROIs investigated.

#### 4.3.6 Lesion $R_2^*$ has no association with IJV CSA

Average lesion  $R_2^*$  was not significantly correlated with any parameter, including any IJV CSA metric. Mean lesion  $R_2^*$  in patients was  $15.4 \pm 2.0 \text{ s}^{-1}$ . No lesions had a bright rim on  $R_2^*$ .

Table 4.3 Mean  $R_2^*$  and correlations in various ROIs. Correlations of mean  $R_2^*$  with age and IJV CSA were evaluated with Pearson test, correlations of mean  $R_2^*$  with EDSS and disease duration were performed with Spearman test. n.s., not-significant.

ROI description	volume (ml)	difference:		P-value (t-test)	Age correlation	EDSS correlation	IJV CSA correlation	Disease duration correlation
		patients	controls (95% CI)					
bilateral thalamus, right pulvinar	1.08	1.67	(0.69,2.66)	<0.005	ns	$r=+0.47$ , $P=0.028$	ns	ns
bilateral globus pallidus	0.14	2.11	(0.51,3.72)	<0.05	ns	ns	ns	ns
right putamen	0.14	2.29	(0.47,4.11)	<0.05	ns	ns	ns	ns
cortical hot spots	4.33	1.60	(1.09,2.11)	<0.000001	$r=-0.48$ , $P=0.024$	ns	ns	ns
white matter cool spots	4.99	-1.49	(-2.27,-0.71)	<0.0001	ns	ns	ns	ns



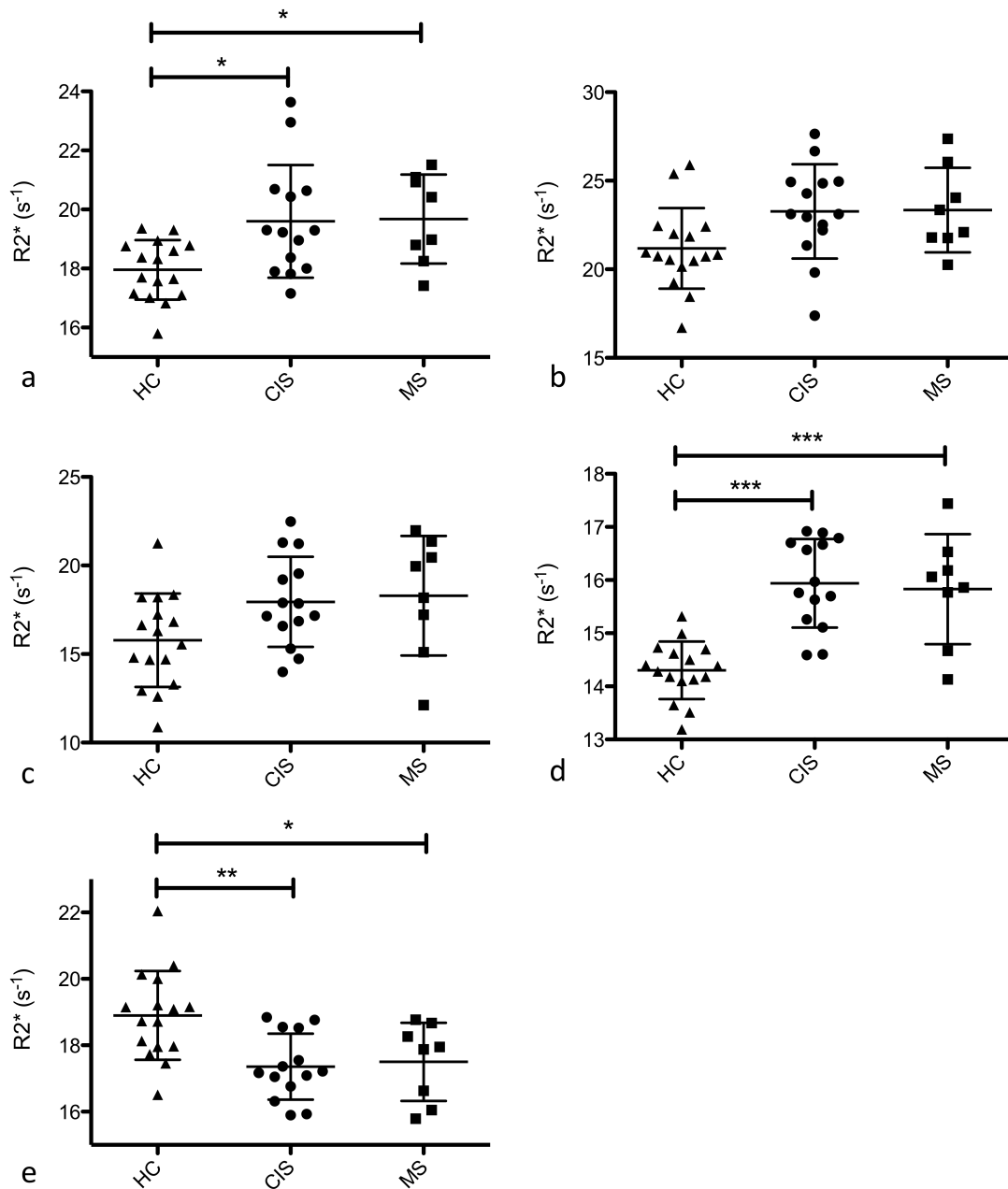


Figure 4.3 Mean  $R_2^*$  at baseline for healthy controls (HC, n=16), CIS patients who have not converted to MS (CIS, n=14), and MS patients (MS, n=8, i.e. those subjects who were in the CIS group at baseline that have since received a diagnosis of clinically definite MS). For ROIs identified previously: bilateral thalamus and right pulvinar (a), bilateral globus pallidus (b), right putamen (c), cortical hotspots (d), and white matter cool spots (e). Error bars denote standard deviations. All significant pairwise differences are indicated: \*,  $P < 0.05$ ; \*\*,  $P < 0.01$ ; \*\*\*,  $P < 0.001$ .

## 4.4 Discussion

In this study, we evaluated brain iron in patients at high risk for a diagnosis of MS. With our voxel-wise methodology, we were able to reproduce well-known findings regarding iron accumulation with age<sup>9</sup>: specifically, iron increases in numerous sub-cortical nuclei, and, at a lesser rate, in various cortical areas.

Previous 3T MRI studies have investigated differences in brain iron between patients with CIS and controls with conflicting results. In the study of Khalil et al., patients with MS had significantly increased  $R_2^*$  in the basal ganglia compared to both CIS patients and controls, whereas no differences were detected between CIS patients and controls<sup>10</sup>. In that study, comparisons between patients and controls were made for  $R_2^*$  measured in ROIs which are large in volume compared to the voxel-wise analyses performed in the present study. Thus, an exclusively ROI-based approach has inherently reduced sensitivity to iron deposition that is limited to only a portion of a structure. In contrast, Hagemeyer et al. used a MRI phase-based measurement to quantify iron that is sensitive to variations in iron content within a structure<sup>11</sup>. In that study, the authors found evidence of increased iron in CIS patients compared to healthy controls in the pulvinar, putamen, caudate, and total sub-cortical deep grey matter. A difference in ages of subjects in each study might also account for the different results. Khalil et al. studied a cohort of CIS patients of ages  $33.7 \pm 10.3$  years and a healthy control cohort of ages  $36.7 \pm 13.7$  years. In contrast, in Hagemeyer et al.'s study, the CIS patients ( $40.1 \pm 10.4$  years) and healthy controls ( $42.8 \pm 14$  years) were older. One possibility is that, in CIS/MS, normal age-

related accumulation of iron is accelerated so that a difference is only detected at an older age.

Our results suggest that iron accumulation in deep grey matter nuclei including the putamen, globus pallidus, pulvinar, and medial portion of the thalamus has occurred by the earliest clinical stages of the disease. Whether iron accumulation preceded other pathology, occurred immediately after inflammation began, or is ongoing at the time of clinical presentation remains unknown; this question will benefit from longitudinal studies. Iron in these structures is in keeping with known iron accumulation and potentially related atrophy in clinically definite MS<sup>1,12,13</sup>. In particular, increased thalamic iron may mediate damage<sup>4</sup> and contribute to common clinical symptoms associated with the thalamus that can be present early in the disease course, including fatigue<sup>14</sup> and cognitive decline<sup>15</sup>. Curiously, a recent study at 7 T, which used quantitative susceptibility mapping to interrogate iron levels in CIS patients, found increased iron in CIS<sup>16</sup>, but failed to reproduce the above-mentioned and well-accepted trends in iron accumulation with age. None of these previous studies have investigated correlations between  $R_2^*$  differences and IJV caliber.

Our finding of no differences in  $R_2^*$  between MS and unconverted CIS may suggest that increased brain iron is a nonspecific finding of early demyelinating disease. This must be interpreted with caution because the stratification is not perfect: likely some currently unconverted CIS patients will be diagnosed with MS in the future. With longitudinal follow-up of this patient cohort, we will have more accurate diagnosis for all patients; such comparisons will be more telling at that time.

We find that at some positions within the cortex, CIS patients have significantly increased  $R_2^*$ , after age adjustment, compared to controls. This result may indicate that cortical iron accumulation occurs in early MS. Such iron may be implicated with grey matter lesions<sup>17</sup> and is consistent with the growing notion that the cortex is not spared in MS evolution<sup>18</sup>. As cortical changes in  $R_2^*$  were unanticipated, the study was not designed to investigate the presence of cortical demyelination that might co-localize with putative iron increases.

In the future, we intend to compare observed iron changes in patients to the magnitude of healthy age-related increases in iron. This could be done by dividing significant differences in  $R_2^*$  between patients and healthy controls by healthy rates of change of  $R_2^*$  with age. These rates were estimated in the present study from 16 healthy controls. The observed rates (Fig. 4.1 a-d) were measured from a large and relatively well-sampled range of ages and agree with well-known relationships of iron and atrophy with age in different parts of the brain. Therefore we felt these values were sufficiently accurate for a first order correction of  $R_2^*$  data prior to t-test (indeed, this is a standard process for age-adjusted t-tests). However, given that conversion of  $R_2^*$  differences into equivalent years of ageing would involve a division by rate of change of  $R_2^*$ , it would be very sensitive to noise/inaccuracies in the rate of change data. Increased recruitment into the present study is anticipated in the future; this data will facilitate more robust correlations between  $R_2^*$  and age.

In this study, we detected positions in lesion-free white matter with significantly *reduced*  $R_2^*$  in patients compared to controls. These regions are located in areas where WM lesions

are commonly observed in MS patients. Previous studies have interpreted decreased relaxation rates in the NAWM of MS brains as *decreased* myelin or iron content, inflammation, glial proliferation, and/or axonal loss<sup>19</sup>. Such changes in NAWM may precede development of lesions; however, as decreases in  $R_2^*$  are non-specific, further work remains to be done to identify specific disease mechanisms responsible. For example, it is even possible that iron is diffusely increased in these regions and other factors changing  $R_2^*$  overwhelm the expected increase due to iron.

To evaluate a potential role for the extracranial venous system in the observed iron increases, we measured the CSA of the IJVs. We found a difference between CIS patients and controls in the mean CSA of the right IJV only. Mean CSA metrics obtained from TOF MRV are operator independent and reproducible. It is well known that the right IJV is generally of larger caliber than the left<sup>20,21</sup> – this difference is less pronounced in patients with CIS. Our finding of significant differences in IJV caliber between patients and controls is consistent with a recent study that found that patients with clinically definite MS have significantly flattened IJVs compared to controls<sup>22</sup>, although the evaluation of vessel caliber in that study was based on *subjective* rating by blinded radiologists. The authors of that study did not report differences for left and right IJVs separately, so it is difficult to make a complete comparison. Ultimately, we must be cautious when interpreting IJV flattening or reduction of CSA as this may represent: reduced intraluminal pressure which fails to force the vessel to be round, improper IJV development, or external (i.e. outside of IJV) source of vessel pinching/occlusion.

We did not directly interrogate flow, nor did we quantify CSA metrics for vessels other than the IJVs; however, at least one of the IJVs is invariably involved in every potential

CCSVI case<sup>23</sup>. Retrograde/turbulent flow may result in reduced signal intensity within the vessel, but this does not necessarily translate to a reduction in CSA given the very high and relatively uniform contrast that we found to be typical between IJVs and surrounding tissue. If *substantial* flow abnormalities were present, then it is possible that a reduced CSA would be measured due to reduction in signal intensity at the edge of a vessel where such turbulence was present and this could fall below the segmentation threshold. However, such abnormalities would also be associated with poor venous contrast and ghosting or phase-encode artifacts; such artifacts are absent in the IJVs in our data. We found the IJVs to be almost always very well demarcated with excellent contrast from surrounding tissue in controls and patients alike. Therefore, our finding of reduced CSA is most likely explained as reduction in the real CSA of the IJV; it is a remote possibility that reduced CSA may be a consequence of highly turbulent/retrograde flow, given that the artifacts that should accompany such flow disturbances are absent. Such artifacts are notoriously variable from scan session to scan session whereas we have successfully demonstrated that there is no significant scan-rescan variability in CSA metrics. Even if there were a change in CSA introduced by turbulence or retrograde flow, our data show that this is consistent over time. The lack of correlation between CSA and age suggests that CSA is not a dynamically evolving property of the IJVs in adults. Moreover, CSA is not related to conventional clinical metrics such as EDSS or disease duration.

To explore correlates of  $R_2^*$  changes in CIS, we performed a regression of  $R_2^*$  against various potentially disease related parameters for patients for clusters where the age-adjusted difference in  $R_2^*$  between groups was significant. The positive correlation between EDSS, a measure of clinical disability, and thalamic  $R_2^*$  suggests worsening

clinical status with increased brain iron. This result is consistent with findings in definite MS<sup>10</sup>. The observed negative correlation of cortical grey matter increases in  $R_2^*$  with age might indicate patients with CIS are more susceptible to increased tissue loss or atrophy at these positions with age, possibly due to iron-related oxidative stress. We found no evidence that changes in IJV caliber are related to changes in  $R_2^*$  in any structure, including putative iron accumulation in grey matter, or diffuse damage in NAWM.

White matter  $R_2^*$  is typically on the order of  $20 \text{ s}^{-1}$ <sup>24</sup>; however, in white matter lesions in CIS,  $R_2^*$  was measured to be dramatically smaller, suggesting against significant intra-lesion iron in CIS. The lack of association between IJV CSA and lesion  $R_2^*$  also contradicts vein-mediated deposition of iron in classical MS lesions. The absence of bright lesion rims on  $R_2^*$  may indicate that iron arrives at these positions later in the disease<sup>2</sup>.

## 4.5 Conclusion

In summary, we find that CIS patients have increased  $R_2^*$ , a putative metric of iron deposition, in deep and cortical grey matter compared to controls. Damage to NAWM is present in CIS, as indicated by reduction in  $R_2^*$ . These  $R_2^*$  changes may be nonspecific for early demyelinating disease and of limited predictive value for future MS diagnosis: future work is needed to confirm these hypotheses. Our observations confirm IJV narrowing at the earliest stages of MS, but do not support a role for venous caliber changes in explaining the increased iron deposition observed in CIS. Other events must give rise to the detected changes in  $R_2^*$ .

## 4.6 References

1. Drayer B, Burger P, Hurwitz B, Dawson D, Cain J. Reduced signal intensity on MR images of thalamus and putamen in multiple sclerosis: increased iron content? *AJR Am J Roentgenol* 1987; **149**:357-363.
2. Craelius W, Migdal MW, Luessenhop CP, Sugar A, Mihalakis I. Iron deposits surrounding multiple sclerosis plaques. *Arch Pathol Lab Med* 1982; **106**:397-399.
3. LeVine SM, Chakrabarty A. The role of iron in the pathogenesis of experimental allergic encephalomyelitis and multiple sclerosis. *Ann N Y Acad Sci* 2004; **1012**:252-266.
4. Campbell A, Smith MA, Sayre LM, Bondy SC, Perry G. Mechanisms by which metals promote events connected to neurodegenerative diseases. *Brain Res Bull* 2001; **55**:125-132.
5. Yao B, Li TQ, Gelderen P, Shmueli K, de Zwart JA, Duyn JH. Susceptibility contrast in high field MRI of human brain as a function of tissue iron content. *Neuroimage* 2009; **44**:1259-1266.
6. Zamboni P. The big idea: iron-dependent inflammation in venous disease and proposed parallels in multiple sclerosis. *J R Soc Med* 2006; **99**:589-593.
7. Charcot JM. Histologie de la sclérose en plaque. *Gazette des Hopitaux, Paris* 1868; **41**:554-555.
8. Polman CH, Reingold SC, Banwell B et al. Diagnostic criteria for multiple sclerosis: 2010 revisions to the McDonald criteria. *Ann Neurol* 2011; **69**:292-302.
9. Hallgren B, Sourander P. The effect of age on the non-haemin iron in the human brain. *J Neurochem* 1958; **3**:41-51.
10. Khalil M, Langkammer C, Ropele S et al. Determinants of brain iron in multiple sclerosis: A quantitative 3T MRI study. *Neurology* 2011; **77**:1691-1697.



11. Hagemeyer J, Weinstock-Guttman B, Bergsland N et al. Iron deposition on SWI-filtered phase in the subcortical deep gray matter of patients with clinically isolated syndrome may precede structure-specific atrophy. *AJNR Am J Neuroradiol* 2012; **33**:1596-1601.
12. Neema M, Arora A, Healy BC et al. Deep gray matter involvement on brain MRI scans is associated with clinical progression in multiple sclerosis. *J Neuroimaging* 2009; **19**:3-8.
13. Shiee N, Bazin PL, Zackowski KM et al. Revisiting brain atrophy and its relationship to disability in multiple sclerosis. *PLoS One* 2012; **7**:e37049.
14. Tellez N, Rio J, Tintore M, Nos C, Galan I, Montalban X. Fatigue in multiple sclerosis persists over time: a longitudinal study. *J Neurol* 2006; **253**:1466-1470.
15. Feuillet L, Reuter F, Audoin B et al. Early cognitive impairment in patients with clinically isolated syndrome suggestive of multiple sclerosis. *Mult Scler* 2007; **13**:124-127.
16. Al-Radaideh AM, Wharton SJ, Lim SY et al. Increased iron accumulation occurs in the earliest stages of demyelinating disease: an ultra-high field susceptibility mapping study in Clinically Isolated Syndrome. *Mult Scler* 2012;
17. Mainero C, Benner T, Radding A et al. In vivo imaging of cortical pathology in multiple sclerosis using ultra-high field MRI. *Neurology* 2009; **73**:941-948.
18. Geurts JJ, Calabrese M, Fisher E, Rudick RA. Measurement and clinical effect of grey matter pathology in multiple sclerosis. *Lancet Neurol* 2012; **11**:1082-1092.
19. Neema M, Goldberg-Zimring D, Guss ZD et al. 3 T MRI relaxometry detects T2 prolongation in the cerebral normal-appearing white matter in multiple sclerosis. *Neuroimage* 2009; **46**:633-641.
20. Lobato EB, Sulek CA, Moody RL, Morey TE. Cross-sectional area of the right and left internal jugular veins. *J Cardiothorac Vasc Anesth* 1999; **13**:136-138.

21. Lichtenstein D, Saïfi R, Augarde R et al. The internal jugular veins are asymmetric. Usefulness of ultrasound before catheterization. *Intensive Care Medicine* 2001; **27**:301-305.
22. McTaggart RA, Fischbein NJ, Elkins CJ et al. Extracranial venous drainage patterns in patients with multiple sclerosis and healthy controls. *AJNR Am J Neuroradiol* 2012; **33**:1615-1620.
23. Zamboni P, Galeotti R, Menegatti E et al. Chronic cerebrospinal venous insufficiency in patients with multiple sclerosis. *J Neurol Neurosurg Psychiatry* 2009; **80**:392-399.
24. Denk C, Rauscher A. Susceptibility weighted imaging with multiple echoes. *J Magn Reson Imaging* 2010; **31**:185-191.

## 5 Central veins in white matter hyperintensities can be detected at 3 T and may be predictive of an MS diagnosis

### 5.1 Introduction

Demonstration of white matter lesions with magnetic resonance imaging (MRI) is central to multiple sclerosis (MS) diagnosis<sup>1</sup>. However, white matter hyperintensities (WMHs) are not specific to MS and may reflect a number of physiological processes other than inflammatory demyelination (which is itself not specific to MS), including metabolic, vascular, and neurodegenerative disorders<sup>2</sup>. Requirements for MS diagnosis include that demyelinating lesions be proved as disseminated in space and time, moreover mimics of MS must be excluded from the differential<sup>3</sup>. Ultimately, the process of diagnosing a patient with MS can take months or years<sup>4</sup>.

An early and accurate diagnosis with MS will allow quality of life to be retained through early initiation of *disease-appropriate* management<sup>5</sup>. To that end, there is a growing interest in identifying biomarkers to facilitate discrimination between MS and non-MS at first clinical presentation.

One such biomarker may be an MRI-detectable penetrating vein within a WMH. MS lesions have been known to be venocentric since the earliest descriptions of the disease<sup>6</sup>. It was not until 2000 that Tan and colleagues directly demonstrated this physiological finding *in vivo* with MRI<sup>7</sup>. Interest in this biomarker has grown in subsequent years.

In particular, several studies performed by the Nottingham group have addressed this topic<sup>8-11</sup>, and have taken advantage of the excellent visibility of small veins achievable with 7T MRI. In one study, they reported that *all* patients who converted from suspected MS to clinically definite MS had >40% white matter lesions with central veins at baseline<sup>11</sup>. It must be noted that 7T MRI is exclusively a research tool, with virtually no prospect for clinical use in the near future. In clinical practice, 3T and more commonly 1.5T MRI systems are used; however at these lower field strengths, the visibility of veins using conventional image contrasts is diminished and the practicality of the proposed biomarker remains unestablished. Our objectives in the present study are to determine how well central veins in WMHs can be detected using our multi-echo SWI methodology at 3T, and also to investigate the value of such MRI-detectable penetrating veins in WMHs for predicting conversion from clinically isolated syndromes (CIS) to MS.

## 5.2 Methods

### 5.2.1 Subject recruitment

The same patient and control cohorts as in Chapter 4 of this thesis were studied. In short, 22 patients with a CIS suggestive of MS were recruited from the MS Clinic at the London Health Sciences Centre. Additionally, 16 age- and sex-matched healthy controls were recruited from the general population. Informed, written consent was obtained from all study participants. The Health Sciences Research Ethics Board of The University of Western Ontario approved this study.

From a mean follow-up of 11.2 months, updated clinical statuses for all patients were available, namely whether or not an MS diagnosis had been made.

### 5.2.2 MR imaging

All study participants were imaged on a 3T MRI system (TIM Trio, Siemens Medical Solutions, Erlangen, Germany). Relevant contrasts acquired include 2D axial FLAIR: TE/TI/TR = 136/2850/15000 ms; in-plane resolution =  $1 \times 1 \text{ mm}^2$ , 50 slices, slice thickness = 3 mm. 3D T1-weighted (T1w) MPRAGE: TI/TE/TR = 900/6.9/2060 ms; voxel size =  $0.5 \times 0.5 \times 1.0 \text{ mm}^3$ . Additionally, 3D multi-echo gradient echo (GRE):  $TE_1/\Delta TE/TR = 10/7/52 \text{ ms}$  (6 echoes), voxel size =  $0.5 \times 0.5 \times 1.0 \text{ mm}^3$ . Three GRE volumes were acquired, with approximately 15 to 20 mm of overlap between adjacent slabs, providing full brain coverage including the cerebellum.

### 5.2.3 Image processing

Processing was performed in MATLAB (The MathWorks, Inc., Natick, MA) and FSL (FMRIB, Oxford, UK).

Magnitude and phase data from each GRE slab were combined to produce multi-echo susceptibility weighted images (SWI) according to post-average processing with the conventional, linear mask function as described in Chapter 2. From magnitude data, maps of  $S_0$ , the steady state signal, were generated via voxel-wise curve fit to Eq. 2.3.

Using transformation matrices calculated from co-registering mean magnitude for each slab to the T1w volume (as in Chapter 4), SWI and  $S_0$  volumes were transformed into the space of the corresponding T1w volume for that patient. The three registered slabs of

each contrast for a given patient were concatenated by arithmetic averaging of overlapping voxels. To remove T1-weighting and the effect of flip-angle variations over the imaging slab from SWI, the  $S_0$  volume was first median-filtered with a  $5 \times 5 \times 5$  mm<sup>3</sup> kernel to smooth and denoise the volume. The full-brain SWI volume was divided by the filtered  $S_0$  volume to produce a full-brain SWI with consistent contrast throughout the volume. Representative SWI images before and after correction with filtered  $S_0$  are shown in Figure 5.1. FLAIR volumes were co-registered to T1w volumes using the FLIRT tool from FSL.

#### 5.2.4 Image analysis

SWI and FLAIR for each volunteer (patients and controls), as processed above, were saved to a directory with a random label. All identifiers were removed to ensure image rating was blinded. Vein rating was performed for one subject at a time, as follows.

FLAIR and SWI were loaded in FSLVIEW viewer, which allows volumes to be viewed in the three orthogonal planes simultaneously. WMHs were identified on FLAIR; only WMHs with a maximum dimension in one of the three orthogonal planes of at least 3 mm were rated. FLAIR image was then toggled off to reveal the SWI image. The presence of a central vein was then rated (yes or no) using the criteria proposed by Tallantyre<sup>9</sup>. Venous vessels were hypointense on SWI and were only counted if they (i) could be visualized in at least 2 perpendicular planes, (ii) appeared linear in at least 1 plane, and (iii) were completely surrounded by hyperintense signal in at least 1 plane. The total number of WMHs and the total number of venocentric WMHs were recorded for each volunteer.

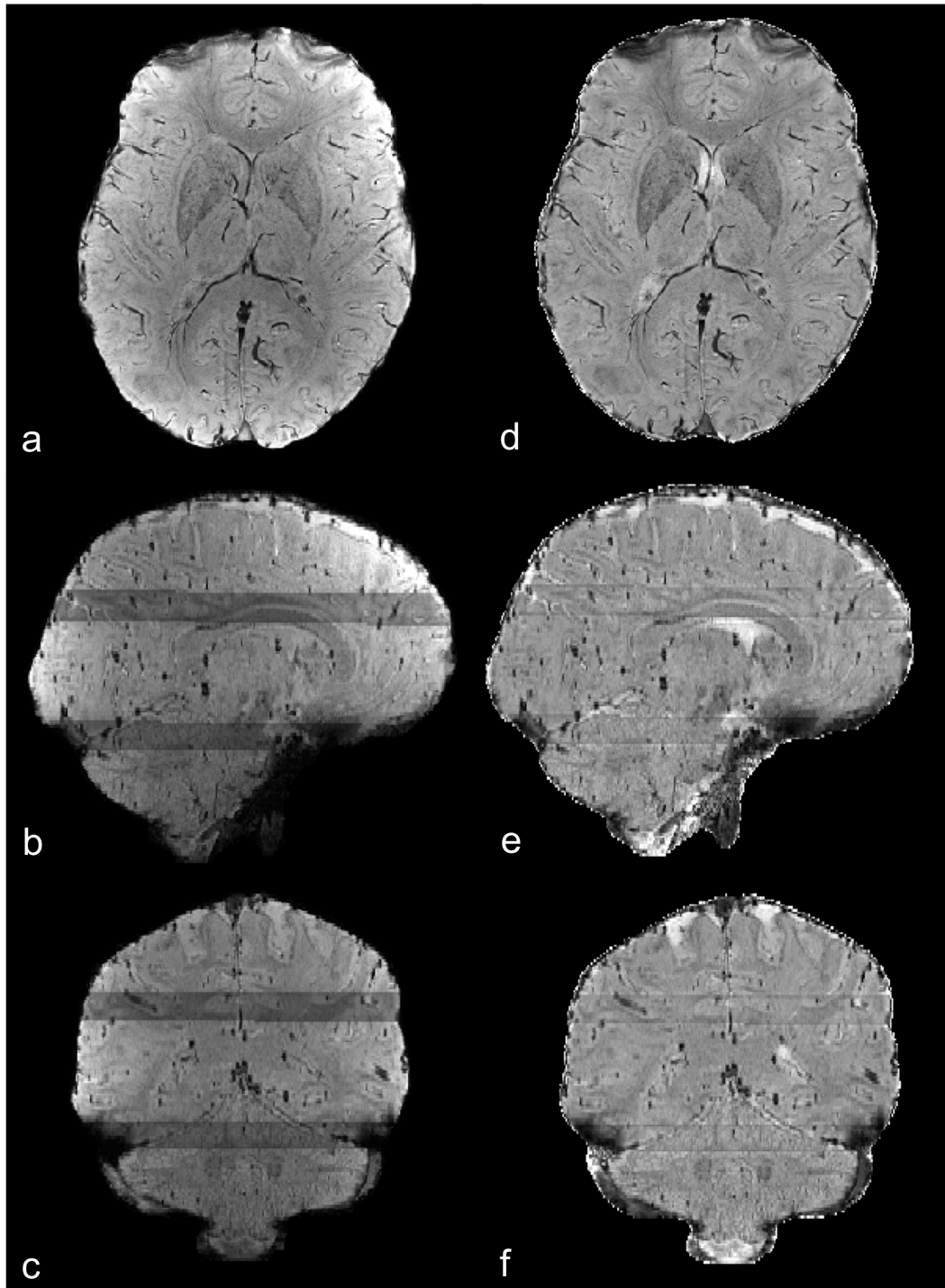


Figure 5.1 Multi-echo SWI images before (a-c) and after (d-f) correction by division with blurred  $S_0$ . Unwanted effects of non-uniform flip angle, T1-weighting, and receive coil sensitivity are mitigated using this methodology.

We acknowledge that the number and distribution of WMHs in a given subject had the potential to unblind the primary rater in this study with respect to subject status (patient versus control). We evaluated this possibility as follows. Thirteen lesions from different subjects were cropped from surrounding tissue. A secondary rater, blinded to the original rating results, was shown these cropped lesions one at a time and asked to rate for a central vein. As a measure of inter-rater agreement, Cohen's kappa was calculated to be 0.70, indicating adequate agreement. For future work, we propose rating by consensus of two physicians to improve inter-rater agreement.

### 5.2.5 Statistical evaluation

All statistical analyses were performed in Prism v. 5.0 (GraphPad, LaJolla, CA).

Using Fisher's exact test, WMH counts (venocentric versus non-venocentric) were compared between healthy controls and all CIS patients. Using Chi-squared, WMH counts were compared between healthy controls, CIS patients who did not convert to MS by follow-up, and CIS patients who did convert to MS by follow-up. Post-hoc comparisons were made between pairs of columns using Fisher's exact test with Holm-Bonferroni correction of P-values.

For each subject, the %LCV (percentage lesions with central veins) was calculated as  $(\text{number of WMHs with a central vein})/(\text{total number of WMHs}) \times 100\%$ . Using two-sided t-test, %LCV was compared between healthy controls and all CIS patients. Using one-way ANOVA with Tukey post hoc, %LCV was compared between healthy controls, CIS patients who did not convert to MS by follow-up, and CIS patients who did convert to MS by follow-up.



### 5.3 Results

Representative FLAIR and SWI images are shown for a venocentric WMH in Figure 5.2a,b and for a non-venocentric WMH in Fig. 5.2c,d. Despite similar appearance on FLAIR, a radiological standard for lesion identification, there is a differential appearance on SWI.

By the follow-up, 8 patients had been diagnosed with MS. These patients make up the MS group referred to subsequently; all other patients comprise the non-converted CIS group. Group totals of WMHs with and without central veins are presented (Table 5.1). In the MS group, 67% of all lesions were venocentric; in non-converted CIS, 50% of lesions were venocentric; in the healthy control group, 24% of WMHs were venocentric. In the entire baseline CIS group, of 288 lesions, 59% were venocentric. When comparing WMH venocentricity counts in healthy controls to all CIS patients, Fisher's test yields  $P=0.0003$ . When considering all three groups separately, the Chi-square test yielded a highly significant  $P<0.0001$ . P-values from post-hoc pair-wise comparisons, corrected for multiple comparisons, were: between healthy controls and non-converted CIS,  $P=0.013$ ; between healthy controls and MS,  $P<0.001$ ; and between non-converted CIS and MS,  $P=0.011$ .

Means and standard deviations of %LCV were calculated for healthy controls ( $12\pm 19\%$ ,  $n=8$ ) and all patients with CIS at baseline ( $55\pm 33\%$ ,  $n=20$ ) and compared with a t-test, yielding  $P=0.002$ . Figure 5.3 presents %LCV for each subject: healthy controls, unconverted CIS, and MS patients (ANOVA  $P=0.0004$ , post hoc significant pairwise differences illustrated).

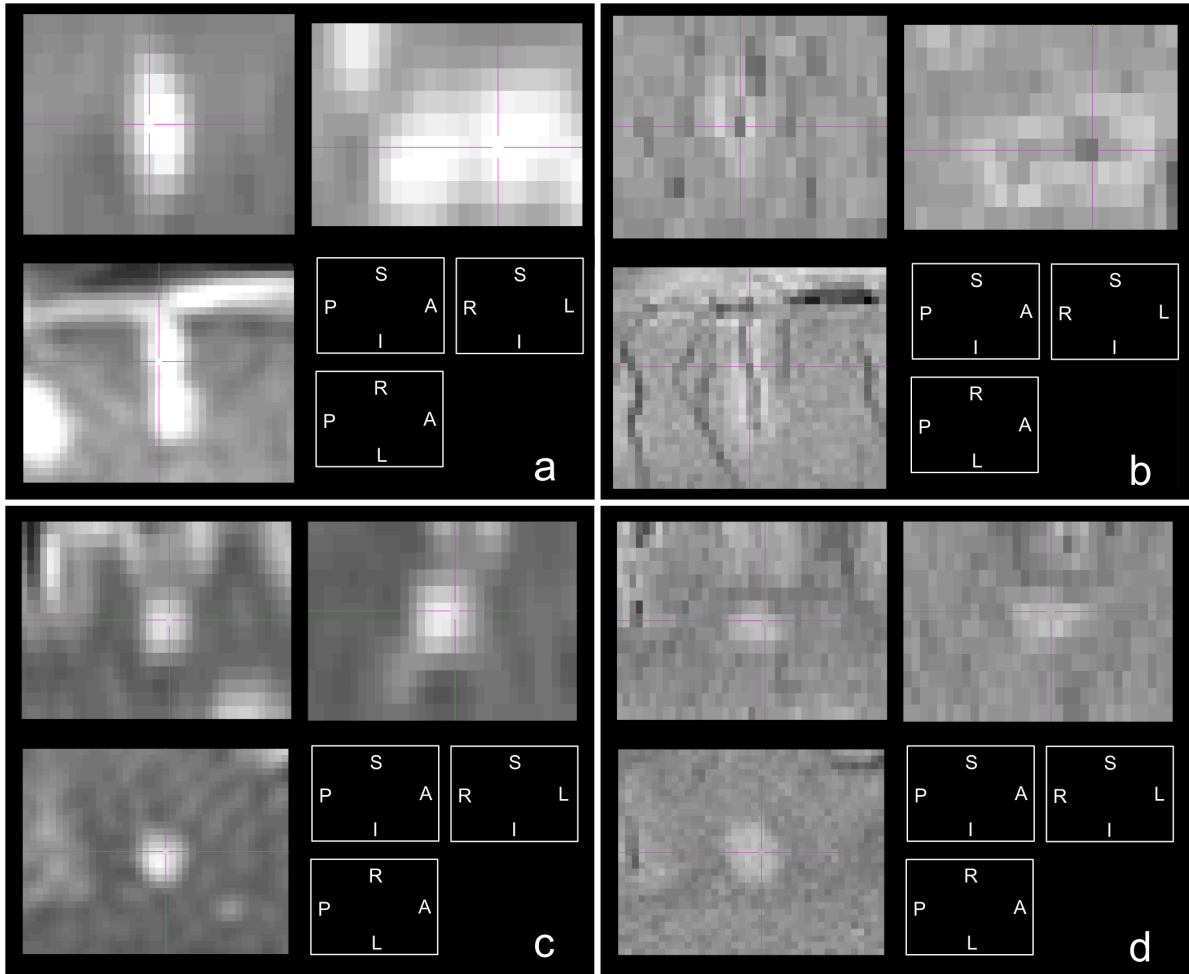


Figure 5.2 FLAIR (a,c) and multi-echo SWI (b,d) of a venocentric WMH in a patient with MS (a,b) and of a non-venocentric WMH (c,d) in a healthy control.

Table 5.1 Contingency table of WMH counts in healthy controls and patients.

	Healthy Controls	Non-converted CIS	MS
Venocentric WMHs	7	65	106
Non-venocentric WMHs	22	64	53

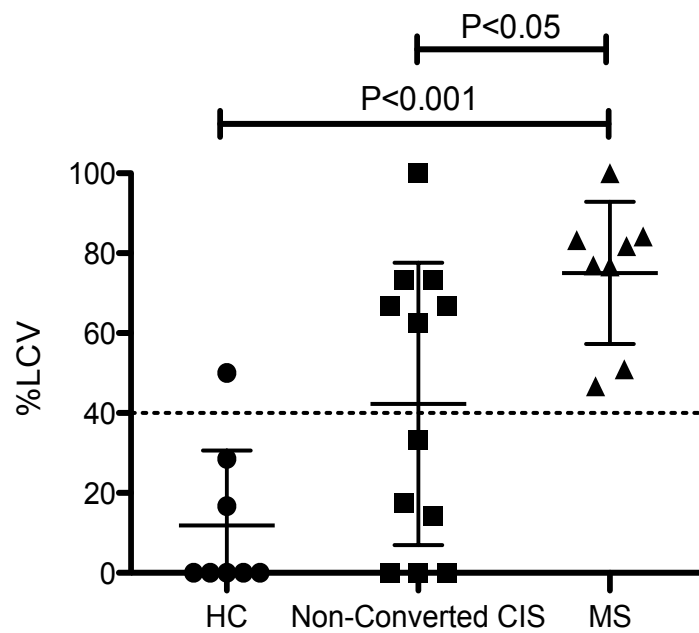


Figure 5.3 %LCV for different study groups. Patients with diagnosed MS show a substantial increase in %LCV compared to both other groups. The dashed line indicates %LCV of 40%, proposed to allow discrimination between MS and non-MS. All subjects with no WMHs (8 controls, 2 non-converted CIS) were excluded from this analysis.

## 5.4 Discussion

In this study, we investigated a newly proposed biomarker for MS – MRI detectable veins within white matter lesions – using post-average multi-echo SWI with a linear mask function at 3 T, as optimized in Chapter 2. We are able to detect such veins using our methodology and differentiate between WMHs with and without central veins (Fig. 5.2). This study did not include imaging at 7 T, thus it is impossible to directly compare our sensitivity to small veins using 3 T versus 7 T, but given the similarity of our results to previous work at 7 T, as will be elaborated on below, we are confident our sensitivity is similar.

When comparing the number of WMHs with and without central veins between study groups, it is clear that we are able to detect significantly more WMHs with central veins in patients with MS, as compared to both unconverted CIS patients and to healthy controls. Various studies at 7 T have reported that in MS patients, the fraction of lesions with central veins ranges from 59%<sup>12</sup> to 92%<sup>13</sup>. Our detected incidence of central veins within MS lesions (67%) appears to be at the lower end of this range.

Given the intimate role of a central vein in the development of a lesion in MS (Chapter 1, Section 1.1.5), it is not unreasonable to expect all MS plaques to be associated with central veins. Indeed, by use of SWI post-contrast injection, Tan et al. demonstrated central veins in 99% of MS lesions<sup>7</sup>. Measurements of %LCV<100% *in MS* are likely due to failure to visualize a certain fraction of veins, perhaps those that fall below the detection threshold due to size, orientation, or oxygenation.

There is a significantly larger fraction of lesions that are venocentric in the non-converted CIS group compared to healthy controls (50% versus 24%). This suggests either (1) several MS patients remain in the non-converted CIS group who have yet to be diagnosed, (2) venocentric lesions are a feature of other diseases which might be indistinguishable from MS at early clinical presentations, or (3) both of the above.

According to the literature, WMHs in individuals in the healthy control cohort may be associated with relatively benign pathology such as high blood pressure<sup>14</sup> or headache<sup>15</sup>, neither of which are necessarily associated with venocentric pathology. Alternatively, these WMHs may be idiopathic and without clinical manifestation. Healthy controls included in this study had relatively few WMHs (median: 2, min: 1, max: 7) but it is not unrealistic that these foci could occasionally be associated with a vein merely ‘by chance’ given the ubiquitous nature of veins in the brain.

When evaluating %LCV on a subject by subject basis (Fig. 5.3) we are able to reproduce the 7T finding of Tallantyre et al. that all patients with MS have %LCV>40% at baseline<sup>10</sup>. This reinforces speculation that detection of this biomarker at first clinical presentation may have utility in expediting MS diagnosis. Due to the relatively short study window (less than 1 year, although patients will continue to be followed until 2 years) it is likely that some CIS patients who have not yet received an MS diagnosis will eventually receive one. In fact, the non-converted CIS group shows a bi-modal tendency, with one cluster of patients (%LCV>40%) having %LCV distinctly larger than the other cluster (%LCV<40%). An interesting hypothesis that awaits confirmation at the study’s completion is that those non-converted CIS patients in the upper cluster will eventually be diagnosed with MS, and those in the lower cluster will not. Given the short follow-up,

and the fact that we expect many non-converted CIS patients to yet receive an MS diagnosis, at this time calculation of positive and negative predictive values is inappropriate.

A single other 3T study has also reported that venocentric lesions in possible MS are predictive of subsequent MS diagnosis<sup>16</sup>. That study used single-echo SWI (potentially a more practical approach, as discussed below). The authors, however, did not report fraction of lesions that were venocentric; rather, they reported the total number of large lesions with penetrating veins for each patient. This rating methodology may not be useful in radiological presentations with numerous small foci.

One significant limitation of the present study is the choice of MRI contrast for vein detection. As implemented here, multi-echo SWI requires approximately 32 minutes for full brain coverage. This is prohibitively long for clinical use. We did not investigate the ability of multi-echo SWI with fewer echoes, or single-echo SWI (both of which require reduced scan time) to visualize intra-lesional veins. Given the increasing prevalence of 3T systems in clinical use (both in developed and developing countries), investigating the feasibility of imaging this biomarker at 1.5 T may be a less important goal than optimization at 3 T, given the increased venous contrast at the latter field.

Moreover, as alluded to previously, the specificity of this biomarker to MS remains unestablished. Certainly, not all CIS patients have MS<sup>17</sup>. The prospective value of this biomarker might be diminished if large values of %LCV are also detected in common MS mimics. To partially address this question, we are currently recruiting patients with

WMH who have clinical diagnoses *other than* MS to serve as a control group for the same type of analyses described herein.

Two notable challenges for all scientists working in this field remain. The first: what to do in the case of patients with very small or large lesion burdens? In the first case, what is the minimum number of lesions that must be rated (and therefore be present) to obtain a confident evaluation? In this study, we had 2 patients with no WMHs. In the second case, might it be appropriate to rate only a subset of the lesions in order to obtain a representative but accurate %LCV? Using hypergeometric distribution methodology, Tallantyre et al. report that if only 10 lesions per patient were rated (in patients with >10 lesions), the diagnosis of MS/non-MS could correctly be predicted with 90% certainty in 44 out of 45 patients tested<sup>10</sup>.

The second challenge is: what constitutes a penetrating vein from a radiological standpoint? The shape of the lesion, and possibly the course of the vein within are relevant. In several studies, criteria for venocentricity are clearly and unambiguously outlined; in others, they are absent. It would be best to adopt a common set of criteria, such as those used herein and originally outlined in the works of the Nottingham group<sup>9</sup>.

## 5.5 Conclusion

We report that WMHs with penetrating veins can be detected in MS using multi-echo SWI at 3 T. A larger fraction of venocentric WMHs were detected in MS (67%) compared to non-converted CIS patients (50%), and healthy controls (24%). Our sensitivity to central veins appears to be in line with that of higher field systems.



Preliminary results in a cohort of CIS patients that are being followed serially are consistent with previous reports that a large %LCV at baseline is highly predictive of a subsequent MS diagnosis.

## 5.6 References

1. Polman CH, Reingold SC, Banwell B et al. Diagnostic criteria for multiple sclerosis: 2010 revisions to the McDonald criteria. *Ann Neurol* 2011; **69**:292-302.
2. Eckstein C, Saidha S, Levy M. A differential diagnosis of central nervous system demyelination: beyond multiple sclerosis. *J Neurol* 2012; **259**:801-816.
3. Charil A, Yousry TA, Rovaris M et al. MRI and the diagnosis of multiple sclerosis: expanding the concept of "no better explanation". *Lancet Neurol* 2006; **5**:841-852.
4. Moraal B, Pohl C, Uitdehaag BM et al. Magnetic resonance imaging predictors of conversion to multiple sclerosis in the BENEFIT study. *Arch Neurol* 2009; **66**:1345-1352.
5. Bergamaschi R, Quaglini S, Tavazzi E et al. Immunomodulatory therapies delay disease progression in multiple sclerosis. *Mult Scler* 2012;
6. Charcot JM. Histologie de la sclérose en plaque. *Gazette des Hopitaux, Paris* 1868; **41**:554-555.
7. Tan IL, van Schijndel RA, Pouwels PJ et al. MR venography of multiple sclerosis. *AJNR Am J Neuroradiol* 2000; **21**:1039-1042.
8. Tallantyre EC, Brookes MJ, Dixon JE, Morgan PS, Evangelou N, Morris PG. Demonstrating the perivascular distribution of MS lesions in vivo with 7-Tesla MRI. *Neurology* 2008; **70**:2076-2078.

9. Tallantyre EC, Morgan PS, Dixon JE et al. A comparison of 3T and 7T in the detection of small parenchymal veins within MS lesions. *Invest Radiol* 2009; **44**:491-494.
10. Tallantyre EC, Dixon JE, Donaldson I et al. Ultra-high-field imaging distinguishes MS lesions from asymptomatic white matter lesions. *Neurology* 2011; **76**:534-539.
11. Mistry N, Dixon J, Tallantyre E et al. Central Veins in Brain Lesions Visualized With High-Field Magnetic Resonance Imaging: A Pathologically Specific Diagnostic Biomarker for Inflammatory Demyelination in the Brain. *JAMA Neurol* 2013; 1-6.
12. Ge Y, Zohrabian VM, Grossman RI. Seven-Tesla magnetic resonance imaging: new vision of microvascular abnormalities in multiple sclerosis. *Arch Neurol* 2008; **65**:812-816.
13. Sinnecker T, Dorr J, Pfueller CF et al. Distinct lesion morphology at 7-T MRI differentiates neuromyelitis optica from multiple sclerosis. *Neurology* 2012; **79**:708-714.
14. Dufouil C, de Kersaint-Gilly A, Besancon V et al. Longitudinal study of blood pressure and white matter hyperintensities: the EVA MRI Cohort. *Neurology* 2001; **56**:921-926.
15. Porter A, Gladstone JP, Dodick DW. Migraine and white matter hyperintensities. *Curr Pain Headache Rep* 2005; **9**:289-293.
16. Kau T, Taschwer M, Deutschmann H, Schonfelder M, Weber JR, Hausegger KA. The "central vein sign": is there a place for susceptibility weighted imaging in possible multiple sclerosis? *Eur Radiol* 2013; DOI:10.1007/s00330-013-2791-4.
17. Miller DH, Weinshenker BG, Filippi M et al. Differential diagnosis of suspected multiple sclerosis: a consensus approach. *Mult Scler* 2008; **14**:1157-1174.

## 6 Conclusion

In this thesis, we have proposed and developed methodology that has allowed subtle components of multiple sclerosis pathology to be probed with MRI, especially in regard to iron accumulation and a role for veins. To implement this methodology in the context of early MS, we have recruited a cohort of patients with clinically isolated syndromes (CIS) as well as healthy controls; we are currently following these cohorts longitudinally with scans every 4 months over a 2-year period. This chapter provides a brief summary and discussion of experiments described in this thesis. Possible extensions of this study and methodology are discussed.

### 6.1 Thesis Summary and Discussion

For decades, an association has been recognized between MS and iron accumulation in deep grey matter nuclei<sup>1</sup> as well as focally within lesions<sup>2</sup>. Questions posed about iron's role as either a mediator of damage or as an epiphenomenon remain unanswered<sup>3</sup>. In this thesis, we sought to characterize biomarkers associated with iron deposition in patients with early presentations of MS.

Chapter 2 addressed **Specific Aim 1**: *to optimize an MRI post-processing technique to produce both cerebral venograms and quantitative images for measuring iron*. In this regard, we established an optimal method to perform multi-echo susceptibility weighted imaging (SWI), a qualitative contrast that yields excellent visibility of small veins and iron-rich structure. Such a contrast holds promise for investigating changes in early MS, given the established, yet incompletely understood link between small veins, iron

accumulation, and the disease. In addition to the above-mentioned central objective of the chapter, we demonstrated that numerical simulation and scoring by trained raters are not equivalent in terms of optimization of contrast for SWI. One particularly promising application of this technique to which we are looking forward is the study of central veins within white matter hyperintensities in MS (as described in Chapter 5) versus in other neurological conditions. Moreover, the advantage of a multi-echo gradient echo sequence is that such data facilitate computation of maps of  $R_2^*$ , a *quantitative* parameter which is highly sensitive to iron levels in the brain<sup>4</sup> (as used in Chapter 4). In this chapter, we also validated our measurements of  $R_2^*$  against numerous previously reported values.

Chapter 3 addressed **Specific Aim 2**: *to establish reproducibility of quantitative measures of internal jugular vein (IJV) caliber, given the proposed role for these veins in MS pathogenesis*. Inasmuch, we proposed methodology to obtain quantitative metrics of IJV caliber from axial time of flight magnetic resonance venograms. We established that these metrics are sufficiently reproducible to allow the anatomy of these veins to be described in a quantitative manner. We report coefficient of variation of measurements of average CSA along the entire vessel to have typical values on the order of 7%; this is our motivation for using this metric in Chapter 4.

Chapter 4 addressed **Specific Aim 3**: *to compare relative levels of iron between CIS patients and healthy controls*. We applied above methodology to study differences in iron that potentially manifest early in MS by comparing  $R_2^*$  for each voxel in the brain between healthy controls and patients with CIS. Evidence for increased iron was found in deep as well as cortical grey matter. Increased thalamic iron was associated with clinical disability, suggesting that iron may cause tissue damage; alternatively, iron deposition

may occur as a possibly quiescent epiphenomenon very soon after the primary pathology. With future work, we intend to track iron levels in deep brain structures over time to differentiate between the two scenarios. If initially high iron levels are responsible for toxicity, they may not increase. If iron accumulation is a side-effect of an ongoing (and possibly immune-related) process throughout the disease, then we expect iron levels to increase with time. Of course, a dual role for iron is possible – as both a cause and consequence of pathology. Our preliminary finding that iron levels at CIS may not necessarily be predictive of subsequent MS diagnosis is very intriguing and requires additional clinical diagnoses for our unconverted CIS cohort before confirmation. Perhaps increased brain iron is typical early on in several idiopathic demyelinating diseases, whereas MS is additionally marked by iron accumulation throughout the disease? At the very least, our current findings, including correlation between deep grey matter iron and clinical status, serve as a reminder that MS is a disease that extends beyond the white matter and includes factors in addition to inflammatory demyelination.

In white matter, we did not detect increased  $R_2^*$  at lesion rims, a correlate of increased iron at these positions<sup>5</sup> that is known from histology. Beyond that, we are limited in our ability to comment on the presence of lesion iron. We detected decreased  $R_2^*$  within lesions. In MS tissue, we expect increases in  $R_2^*$  to be specific for increased iron, while acknowledging many factors can contribute to a decrease in  $R_2^*$  (even in the presence of increased iron) including demyelination and edema. Following longitudinal studies and use of different quantitative contrasts (such as local frequency), we will be able to comment on intra-lesion iron as a function of time.

Taking our findings in deep grey matter and white matter lesions together, a possible scenario emerges where iron in at least two compartments (deep grey matter and lesion) accumulates differentially throughout the disease and thus may reflect different contributions to tissue damage.

To explore one possible explanation of iron increases in the deep brain, we measured the calibers of the IJVs. We found that the right IJV was significantly narrower in patients than in healthy controls and the total IJV CSA (i.e. summed across left and right IJVs) trended towards being lower in patients. This finding will need to be explored in the context of longitudinal data for robustness. One important findings is that, after regression between  $R_2^*$  increases and total IJV CSA, we found no evidence that these iron increases were a function of IJV caliber, suggesting another disease mechanism must be responsible for iron accumulation at these positions. In summary, increased iron is present in early clinical stages of MS, but this is not due to vessel occlusion. Venous abnormalities may exist in MS, but appear not to be functionally related to pathogenesis.

While CIS represents a relatively early point in the clinical disease course (ex. relative to RRMS or SPMS), there is likely a window of a finite length of time between onset of CNS inflammation and CIS. Information about iron concentration in affected tissue during this window would be highly useful for elucidating iron's role in MS. In the future, insights into this problem may be acquired via imaging studies in groups of individuals at high risk for developing MS or in appropriate animal models.

In the studies described herein, we did not use quantitative susceptibility mapping (QSM), a relatively new technique for quantitative brain imaging<sup>6</sup>, although a brief

discussion is warranted here. In a quantitative susceptibility map, which is derived from phase data, voxel intensity scales with local magnetic susceptibility, an intrinsic property of the tissue (unlike  $R_2^*$ ). Like  $R_2^*$ , tissue susceptibility scales linearly with iron concentration<sup>7</sup> and is strongly influenced by myelin content<sup>8</sup>. An advantage of QSM is that these images can be generated from a single gradient echo, although multi-echo GRE can also be used. Using QSM, at least two studies have reported on increases in iron in CIS compared to healthy controls by taking mean values in relatively large ROIs<sup>9,10</sup>. These results suggest that QSM is more sensitive to iron than  $R_2^*$ , as a previous study using the ROI approach with  $R_2^*$  failed to detect any difference between CIS and controls<sup>11</sup>. However, an inherent problem with using QSM for the study of iron is that in the presence of high iron concentrations, the signal-to-noise ratio in the phase image will be reduced. This might lead to unreliable estimates of tissue susceptibility at these positions.

A major challenge with QSM is the extensive post-processing, errors in which can lead to image artifacts. In brief, a local frequency map is generated by unwrapping phase and then filtering the unwrapped phase to remove background field contributions. Since a very robust frequency map is required to create QSM of acceptable quality, homodyne filtering is not sufficient. Instead, filtering is performed using more sophisticated models<sup>6,12</sup>. Subsequently, this filtered and unwrapped phase is scaled to create a local frequency map. The Fourier transform of this frequency map is divided by a dipole kernel to produce the (Fourier transform) of the quantitative susceptibility map. This last step, the field-to-source inversion, in particular is challenging as for some positions in Fourier space, the kernel is equal to zero; therefore, the inversion is ill-posed and a solution

cannot be found. A number of techniques have been proposed to overcome this challenge, and can be found in the literature<sup>13</sup>.

QSM has also been used to study white matter fiber tracts by considering myelin as an anisotropic perturber of magnetic field<sup>14</sup>, as opposed to a magnetic dipole (such as punctate iron). While this is an area of ongoing research and optimization, this speaks to the potential of QSM to study both myelin and iron.

In our studies, we did not use QSM for two major reasons. First, our phase data included open-ended fringe lines<sup>15</sup>, a phase artifact that is the result of sub-optimal combination of data from different receiver elements in the RF coil. In the presence of open-ended fringe lines, all phase unwrapping algorithms currently used for QSM do not produce an acceptable result. For SWI, unwrapping and filtering are performed automatically and simultaneously by the homodyne method; although, as pointed out above, this type of phase filtering is insufficient for QSM. Without properly unwrapped phase maps, QSM cannot be performed. Second, at the onset of the study, optimization of QSM was in its infancy and robust validations of a linear relationship between QSM and iron concentration were absent. Therefore, our MRI protocol was designed with the goal of generating  $R_2^*$ , which remains a widely used marker for iron, even alongside QSM<sup>8</sup>. Indeed, if the phase unwrapping challenge can be overcome in the future, we anticipate performing QSM in addition to relaxometry to study changes in iron and myelin in early MS.

Chapter 5 addressed **Specific Aim 4**: *to determine if venules can be detected within lesions in CIS patients*. We used optimized multi-echo SWI (Chapter 2) to interrogate the



presence of central venules in white matter hyperintensities (WMHs). We find that patients who have converted from CIS to MS had, at baseline, a significantly larger fraction of WMHs with central veins compared to non-converted CIS patients, as well as to healthy controls. More significantly, we also found that all patients who had been diagnosed with MS within the (relatively short) study window had, at baseline, >40% lesions with central veins. This supports previous work suggesting this biomarker could be used to predict MS diagnosis at first clinical presentation<sup>16</sup>. Challenges remain when considering the clinical feasibility of this biomarker, including studying its specificity for MS lesions, adoption of standard sequences and rating schemes, and large sample size validation.

## 6.2 Future Work

The CIS and healthy control cohorts described in Chapters 4 and 5 are part of an ongoing study, where all subjects are imaged every 4 months over a 2-year window. One strength of our experimental design is that, by the end of the study, we will have reasonable confidence in terms of an MS diagnosis of each CIS patient. This will facilitate comparisons not between only patients and controls, but also between healthy controls, patients who had MS at baseline, and those who did not. Ultimately, this will allow us to increase the specificity of our analyses and make conclusions about the predictive value at CIS of different metrics and factors for conversion to MS. The following are specific experiments we intend to perform using this longitudinal data.

### 6.2.1 Longitudinal study of deep grey matter iron

In Chapter 4 of this thesis, we compared  $R_2^*$  between all patients and healthy controls in a cross-sectional manner (i.e. at study baseline). By the study's conclusion, we will be able to evaluate temporal changes including rates of change of  $R_2^*$  (either for each voxel in the brain or for specific structures). An interesting question would be: do patients with early MS demonstrate increased rates of iron accumulation compare to healthy controls, or are local concentrations of iron relatively constant in time during this phase of the disease? Phrased alternatively, we know there are differences in the intercepts of plots of iron versus time for CIS patients and controls; are there also differences in the slopes? Increased iron at baseline in MS compared to healthy controls is required if (but does not necessarily indicate that) iron is a primary cause of damage to deep grey matter structure. Alternatively, accumulation of iron with time might favour iron's role as one of an epiphenomenon of disease<sup>11</sup>. Only after both possibilities have been thoroughly vetted on the entire study cohort will we be able to draw useful conclusions.

### 6.2.2 Longitudinal study of lesion iron and microstructure

The exact pathogenic mechanism of plaque development (including any role for iron) remains unknown. One possibility is that the neuro auto-antigen for unknown reasons (potentially related to environmental or genetic factors) stimulates an immune response that results in irregular iron metabolism<sup>17</sup>. In this case, increased iron may only be detectable after it has been sequestered by macrophages later in the lesion's lifetime<sup>18</sup>. Alternatively, increased iron may be detectable in the earliest stages of lesion pathogenesis as an immediate result of increased iron transport<sup>19</sup> or microhemorrhage<sup>2</sup>. It

is unknown whether iron is directly responsible for inflammation and attraction of cellular effectors, as proposed by Zamboni<sup>20</sup>, although if iron is a driving force for damage, it should be present early in the lesion's development. With our longitudinal study data, we intend to perform retrospective and prospective analyses of lesions to determine the spatial and temporal patterns of lesion iron via  $R_2^*$  measurements. In the literature, it has been reported that as many as one quarter of white matter lesions in CDMS have a hypointense rim on gradient echo magnitude images (corresponding with increased  $R_2^*$ ) indicative of iron<sup>21</sup>. One study suggested that such iron accumulation patterns are exclusive to the subset of lesions that are chronically active<sup>18</sup>. In our CIS patients, no such signal changes at any lesions' rims were seen at baseline. This is consistent with iron accumulating at the lesion rim later in the disease; however after quantitative analyses of serial data for many lesions we will have a more complete picture.

Recently, it has been proposed that local frequency (an additional quantitative contrast attainable from gradient echo images) is very sensitive to changes in tissue microstructure, including changes in myelin and axons, during the progression of lesion pathology in MS<sup>22</sup>, and could be used to estimate the activity within the lesion. This hypothesis has only been explored through numerical simulation, as well as cross-sectionally in vivo. The longitudinal nature of our data set will eventually facilitate tracking of intra-lesional signal changes over time on a lesion-by-lesion basis, which will allow us to study both lesion microstructure, and as noted above, iron.

### 6.2.3 Study of venocentricity of white matter lesions

From the earliest descriptions of MS, the venocentric characteristic of plaques was noted<sup>23</sup>. A central venule is certainly involved in the inflammatory machinery of the plaque<sup>2</sup>, including iron deposition. Recently, numerous MRI studies<sup>16,24,25</sup> have proposed this finding might be non-invasively detected as a prospective biomarker for MS. We explored this issue in Chapter 5, in a proof-of-principle experiment.

Given the prospective nature of our cohort, and increased recruitment that is anticipated, we plan on extending the preliminary work presented in Chapter 5 of this thesis with respect to a role for venocentric lesions in predicting conversion to MS. While the study presented in Chapter 5 was limited by low sample size, we aim to recruit until a total of 30 to 50 CIS patients. By the study's conclusion, we will be able to determine with confidence if a high percentage of lesions with central veins at baseline is predictive of subsequent MS diagnosis; our preliminary work suggests this is the case. Two recent studies have reported on iron at the lesion rim in MS compared to other conditions, as indicated by hypointense signal on  $T_2^*$  weighted MRI at the edge of the lesion<sup>21,26</sup>. Perhaps the coincidental findings of increased iron and a central vein would improve specificity of this methodology.

Given that white matter hyperintensities on T2-weighted MRI are notoriously non-specific, one aspect of MS diagnosis for which this methodology would be highly useful is differentiating MS from other neurological diseases on the basis of lesions with central veins. Very few studies have investigated the presence of central veins in white matter lesions of other diseases. Sinnecker and colleagues showed that in neuromyelitis optica

spectrum disorders (which involve inflammatory demyelination and can be confused with MS) only 35% of WMHs had a central vein, as opposed to 92% in MS<sup>21</sup>. This result suggests the approach explored in Chapter 5 has potential to differentiate between the two. Alternatively, Lummel et al. reported WMHs in patients with small vessel disease were as often found along small veins as in MS (78% versus 80%)<sup>27</sup>. Certainly, work remains to be done to establish in which diseases, if any, venocentric WMHs are expected in addition to MS.

To further investigate these topics, we are recruiting an additional cohort of patients for our study: patients with clinical diagnoses of neurological diseases other than MS but with similar white matter hyperintensities (migraine, neurological presentations of systemic autoimmune diseases, vascular disorders). We intend to recruit 20 patients in this category that are age- and sex- matched to our control and CIS cohorts for a single MRI using our 3T protocol. A revision to our ethics protocol has recently been submitted to this effect.

The addition of this non-MS patient group will allow us to probe the specificity of venocentric lesions, and potentially iron-containing lesions, to MS. Moreover, this new group can serve as an alternative control when evaluating, for example, deep brain iron levels or IJV CSA in MS. This will allow us to address additional relevant questions: Are increases in iron, or changes in vein caliber (as detected in Chapter 4) specific to MS, or prevalent in other neurologic disease as well?

#### 6.2.4 Longitudinal study of IJV caliber

In Chapter 4, we reported that the right IJV was of significantly reduced mean CSA in CIS patients than in healthy controls, while no significant differences were found for the left IJV, or sum of means. Following IJV CSA longitudinally in our complete cohort will establish whether this difference is truly robust and if it is limited to MS, or if it is present in other neurological conditions. This methodology will also allow us to examine the possibility that IJV CSA is a dynamic property in MS (reflecting adaptive venous return).

### 6.3 In closing

The central objective of this thesis was to characterize MRI biomarkers associated with iron deposition in patients with early presentations of MS; major findings in this regard are summarized here. We found that metrics of brain iron were increased in CIS patients, a cohort which included several early MS cases. While increased iron in MS is well known, the predictive value of increased iron in CIS of a future MS diagnosis remains unclear. Moreover, while IJVs were of reduced caliber in CIS patients, this was not associated with metrics of iron accumulation, suggesting that another mechanism must be responsible for iron deposition. Finally, we have reproduced ultra high field strength findings that small veins can be detected within MS plaques, suggesting that there may be diagnostic value in classifying the fraction of lesions which have a central vein in early clinical presentations.

## 6.4 References

1. Drayer BP, Burger P, Hurwitz B et al. Magnetic resonance imaging in multiple sclerosis: decreased signal in thalamus and putamen. *Ann Neurol* 1987; **22**:546-550.
2. Adams CW. Perivascular iron deposition and other vascular damage in multiple sclerosis. *J Neurol Neurosurg Psychiatry* 1988; **51**:260-265.
3. Khalil M, Enzinger C, Langkammer C et al. Quantitative assessment of brain iron by R(2)\* relaxometry in patients with clinically isolated syndrome and relapsing-remitting multiple sclerosis. *Mult Scler* 2009; **15**:1048-1054.
4. Yao B, Li TQ, Gelderen P, Shmueli K, de Zwart JA, Duyn JH. Susceptibility contrast in high field MRI of human brain as a function of tissue iron content. *Neuroimage* 2009; **44**:1259-1266.
5. Walsh AJ, Lebel RM, Eissa A et al. Multiple sclerosis: validation of MR imaging for quantification and detection of iron. *Radiology* 2013; **267**:531-542.
6. Schweser F, Deistung A, Lehr BW, Reichenbach JR. Quantitative imaging of intrinsic magnetic tissue properties using MRI signal phase: an approach to in vivo brain iron metabolism? *Neuroimage* 2011; **54**:2789-2807.
7. Langkammer C, Schweser F, Krebs N et al. Quantitative susceptibility mapping (QSM) as a means to measure brain iron? A post mortem validation study. *Neuroimage* 2012; **62**:1593-1599.
8. Deistung A, Schafer A, Schweser F, Biedermann U, Turner R, Reichenbach JR. Toward in vivo histology: a comparison of quantitative susceptibility mapping (QSM) with magnitude-, phase-, and R2\*-imaging at ultra-high magnetic field strength. *Neuroimage* 2013; **65**:299-314.
9. Langkammer C, Liu T, Khalil M et al. Quantitative susceptibility mapping in multiple sclerosis. *Radiology* 2013; **267**:551-559.

10. Al-Radaideh AM, Wharton SJ, Lim SY et al. Increased iron accumulation occurs in the earliest stages of demyelinating disease: an ultra-high field susceptibility mapping study in Clinically Isolated Syndrome. *Mult Scler* 2012;
11. Khalil M, Langkammer C, Ropele S et al. Determinants of brain iron in multiple sclerosis: A quantitative 3T MRI study. *Neurology* 2011; **77**:1691-1697.
12. Liu T, Khalidov I, de Rochefort L et al. A novel background field removal method for MRI using projection onto dipole fields (PDF). *NMR Biomed* 2011; **24**:1129-1136.
13. Liu T, Spincemaille P, de Rochefort L, Kressler B, Wang Y. Calculation of susceptibility through multiple orientation sampling (COSMOS): a method for conditioning the inverse problem from measured magnetic field map to susceptibility source image in MRI. *Magn Reson Med* 2009; **61**:196-204.
14. Liu C. Susceptibility tensor imaging. *Magn Reson Med* 2010; **63**:1471-1477.
15. Chavez S, Xiang QS, An L. Understanding phase maps in MRI: a new cutline phase unwrapping method. *IEEE Trans Med Imaging* 2002; **21**:966-977.
16. Mistry N, Dixon J, Tallantyre E et al. Central Veins in Brain Lesions Visualized With High-Field Magnetic Resonance Imaging: A Pathologically Specific Diagnostic Biomarker for Inflammatory Demyelination in the Brain. *JAMA Neurol* 2013; 1-6.
17. Mehindate K, Sahlas DJ, Frankel D et al. Proinflammatory cytokines promote glial heme oxygenase-1 expression and mitochondrial iron deposition: implications for multiple sclerosis. *J Neurochem* 2001; **77**:1386-1395.
18. Mehta V, Pei W, Yang G et al. Iron is a sensitive biomarker for inflammation in multiple sclerosis lesions. *PLoS One* 2013; **8**:e57573.



19. Sfagos C, Makis AC, Chaidos A et al. Serum ferritin, transferrin and soluble transferrin receptor levels in multiple sclerosis patients. *mult scler* 2005; **11**:272-275.
20. Zamboni P. The big idea: iron-dependent inflammation in venous disease and proposed parallels in multiple sclerosis. *J R Soc Med* 2006; **99**:589-593.
21. Sinnecker T, Dorr J, Pfueller CF et al. Distinct lesion morphology at 7-T MRI differentiates neuromyelitis optica from multiple sclerosis. *Neurology* 2012; **79**:708-714.
22. Yablonskiy DA, Luo J, Sukstanskii AL, Iyer A, Cross AH. Biophysical mechanisms of MRI signal frequency contrast in multiple sclerosis. *Proc Natl Acad Sci U S A* 2012; **109**:14212-14217.
23. Charcot JM. Histologie de la sclérose en plaque. *Gazette des Hopitaux, Paris* 1868; **41**:554-555.
24. Tallantyre EC, Dixon JE, Donaldson I et al. Ultra-high-field imaging distinguishes MS lesions from asymptomatic white matter lesions. *Neurology* 2011; **76**:534-539.
25. Kau T, Taschwer M, Deutschmann H, Schonfelder M, Weber JR, Hausegger KA. The "central vein sign": is there a place for susceptibility weighted imaging in possible multiple sclerosis? *Eur Radiol* 2013; DOI:10.1007/s00330-013-2791-4.
26. Wuerfel J, Sinnecker T, Ringelstein EB et al. Lesion morphology at 7 Tesla MRI differentiates Susac syndrome from multiple sclerosis. *Mult Scler* 2012; **18**:1592-1599.
27. Lummel N, Boeckh-Behrens T, Schoepf V, Burke M, Bruckmann H, Linn J. Presence of a central vein within white matter lesions on susceptibility weighted imaging: a specific finding for multiple sclerosis? *Neuroradiology* 2011; **53**:311-317.

# Appendix A: Ethics approval notice



## Use of Human Participants - Ethics Approval Notice

**Principal Investigator:** Ravi Menon  
**Review Number:** 18335E  
**Review Level:** Delegated  
**Approved Local Adult Participants:** 85  
**Approved Local Minor Participants:** 0  
**Protocol Title:** Magnetic Resonance Imaging of Iron in Multiple Sclerosis at 3 Tesla  
**Department & Institution:** Medical Biophysics, Robarts Research Institute  
**Sponsor:** Canadian Institutes of Health Research

**Ethics Approval Date:** September 15, 2011                      **Expiry Date:** August 31, 2014  
**Documents Reviewed & Approved & Documents Received for Information:**

Document Name	Comments	Version Date
UWO Protocol		
Advertisement	Healthy Control	
Letter of Information & Consent	Healthy Control (Multiple Visit) - Version 2	
Letter of Information & Consent	Healthy Control (Single Visit) Version 2	
Letter of Information & Consent	Patients with CIS (Multiple Visits) Version 2	
Letter of Information & Consent	Patients with MS (Single Visit) Version 2	
Advertisement	Patient	

This is to notify you that The University of Western Ontario Research Ethics Board for Health Sciences Research Involving Human Subjects (HSREB) which is organized and operates according to the Tri-Council Policy Statement: Ethical Conduct of Research Involving Humans and the Health Canada/ICH Good Clinical Practice Practices: Consolidated Guidelines; and the applicable laws and regulations of Ontario has reviewed and granted approval to the above referenced revision(s) or amendment(s) on the approval date noted above. The membership of this REB also complies with the membership requirements for REB's as defined in Division 5 of the Food and Drug Regulations.

The ethics approval for this study shall remain valid until the expiry date noted above assuming timely and acceptable responses to the HSREB's periodic requests for surveillance and monitoring information. If you require an updated approval notice prior to that time you must request it using the UWO Updated Approval Request Form.

Members of the HSREB who are named as investigators in research studies, or declare a conflict of interest, do not participate in discussion related to, nor vote on, such studies when they are presented to the HSREB.

The Chair of the HSREB is Dr. Joseph Gilbert. The UWO HSREB is registered with the U.S. Department of Health & Human Services under the IRB registration #11-0000001A.

Signature

**Ethics Officer to Contact for Further Information**

<input type="checkbox"/> Janice Sutherland	<input checked="" type="checkbox"/> Grace Kelly	<input type="checkbox"/> Shantel Walcott
--	---	--

*This is an official document. Please retain the original in your files.*

# Appendix B: Ethics revision approval notice



Research Ethics

Use of Human Participants - Ethics Approval Notice

**Principal Investigator:** Ravi Menon  
**File Number:**101468  
**Review Level:**Delegated  
**Approved Local Adult Participants:**85  
**Approved Local Minor Participants:**0  
**Protocol Title:**Magnetic Resonance Imaging of Iron in Multiple Sclerosis at 3 Tesla  
**Department & Institution:**Schulich School of Medicine and Dentistry/Medical Biophysics,Robarts Research Institute  
**Sponsor:**Canadian Institutes of Health Research

**Ethics Approval Date:**August 13, 2012 **Expiry Date:**August 31, 2014  
**Documents Reviewed & Approved & Documents Received for Information:**

Document Name	Comments	Version Date
Addition of Co-investigator	Dr. Sarah Morrow and Dr. Amy Lin have been added as co-investigators.	

This is to notify you that The University of Western Ontario Research Ethics Board for Health Sciences Research Involving Human Subjects (HSREB) which is organized and operates according to the Tri-Council Policy Statement: Ethical Conduct of Research Involving Humans and the Health Canada/ICH Good Clinical Practice Practices: Consolidated Guidelines; and the applicable laws and regulations of Ontario has reviewed and granted approval to the above referenced revision(s) or amendment(s) on the approval date noted above. The membership of this REB also complies with the membership requirements for REB's as defined in Division 5 of the Food and Drug Regulations.

The ethics approval for this study shall remain valid until the expiry date noted above assuming timely and acceptable responses to the HSREB's periodic requests for surveillance and monitoring information. If you require an updated approval notice prior to that time you must request it using the University of Western Ontario Updated Approval Request Form.

Members of the HSREB who are named as investigators in research studies, or declare a conflict of interest, do not participate in discussion related to, nor vote on, such studies when they are presented to the HSREB.

The Chair of the HSREB is Dr. Joseph Gilbert. The HSREB is registered with the U.S. Department of Health & Human Services under the IRR registration number IRR 00000940.

Signature \_\_\_\_\_

Ethics Officer to Contact for Further Information

Janice Sutherland	Grace Kelly	Shantel Walcott
-------------------	-------------	-----------------

*This is an official document. Please retain the original in your files.*

## Appendix C: Copyright release of material in Chapter 2

**Mary Harder**

---

**Subject:** FW: Permission to Use Copyrighted Material in a Doctoral Thesis

**From:** Matt Quinn [mailto: ]  
**Sent:** Thursday, March 21, 2013 10:34 AM  
**To:** Mary Harder  
**Subject:** Permission to Use Copyrighted Material in a Doctoral Thesis

Dear Ms Harder

I am a University of Western Ontario graduate student completing my Doctoral thesis tentatively entitled "Magnetic resonance imaging of iron in multiple sclerosis at 3 Tesla". My thesis will be available in full-text on the internet for reference, study and / or copy. Except in situations where a thesis is under embargo or restriction, the electronic version will be accessible through the Western Libraries web pages, the Library's web catalogue, and also through web search engines. I will also be granting Library and Archives Canada and ProQuest/UMI a non-exclusive license to reproduce, loan, distribute, or sell single copies of my thesis by any means and in any form or format. These rights will in no way restrict republication of the material in any other form by you or by others authorized by you.

I would like permission to allow inclusion of the following material in my thesis: "Comparison of multi-echo post-processing schemes for susceptibility weighted imaging using linear and non-linear mask functions" currently under preparation by AJNR for publication in Volume 34 November 2013 issue (manuscript AJNR-12-01328.R1).

The material will be attributed through a citation.

Please confirm in writing or by email that these arrangements meet with your approval.

Sincerely,

Matthew Quinn  
 MD/PhD Candidate  
 Vanier Canada Graduate Scholar  
 Department of Medical Biophysics  
 Schulich School of Medicine & Dentistry

Permission granted by the copyright owner, contingent upon the consent of the author(s); provided complete credit is given to the original source and © owner. Credit line: (initials, last name of author(s), (title of article), (name of journal), (volume #), (issue #), (inclusive pages), (year of publication). © by American Society of Neur

Per: \_\_\_\_\_ 3/22/13  
 (Permissions Editor)

## Appendix D: Copyright release of material in Chapter 4

### ELSEVIER LICENSE TERMS AND CONDITIONS

Aug 14, 2013

---

This is a License Agreement between Matthew P Quinn ("You") and Elsevier ("Elsevier") provided by Copyright Clearance Center ("CCC"). The license consists of your order details, the terms and conditions provided by Elsevier, and the payment terms and conditions.

**All payments must be made in full to CCC. For payment instructions, please see information listed at the bottom of this form.**

Supplier	Elsevier Limited
Registered Company Number	1982084
Customer name	Matthew P Quinn
Customer address	Robarts Research Institute
License number	3207581287374
License date	Aug 14, 2013
Licensed content publisher	Elsevier
Licensed content publication	Multiple Sclerosis and Related Disorders
Licensed content title	Increased deep gray matter iron is present in clinically isolated syndromes
Licensed content author	Matthew P. Quinn, Joseph S. Gati, Martyn L. Klassen, Donald H. Lee, Marcelo Kremenchtzky, Ravi S. Menon
Licensed content date	30 July 2013
Licensed content volume number	
Licensed content issue number	
Number of pages	1
Start Page	
End Page	
Type of Use	reuse in a thesis/dissertation
Portion	full article
Format	both print and electronic
Are you the author of this	Yes

Elsevier article?	
Will you be translating?	No
Order reference number	
Title of your thesis/dissertation	Magnetic resonance imaging of iron in early multiple sclerosis at 3 Tesla
Expected completion date	Aug 2013
Estimated size (number of pages)	
Elsevier VAT number	GB 494 6272 12
Permissions price	0.00 USD
VAT/Local Sales Tax	0.00 USD / GBP
Total	0.00 USD
Terms and Conditions	

### INTRODUCTION

1. The publisher for this copyrighted material is Elsevier. By clicking "accept" in connection with completing this licensing transaction, you agree that the following terms and conditions apply to this transaction (along with the Billing and Payment terms and conditions established by Copyright Clearance Center, Inc. ("CCC"), at the time that you opened your Rightslink account and that are available at any time at <http://myaccount.copyright.com>).

### GENERAL TERMS

2. Elsevier hereby grants you permission to reproduce the aforementioned material subject to the terms and conditions indicated.

3. Acknowledgement: If any part of the material to be used (for example, figures) has appeared in our publication with credit or acknowledgement to another source, permission must also be sought from that source. If such permission is not obtained then that material may not be included in your publication/copies. Suitable acknowledgement to the source must be made, either as a footnote or in a reference list at the end of your publication, as follows:

“Reprinted from Publication title, Vol /edition number, Author(s), Title of article / title of chapter, Pages No., Copyright (Year), with permission from Elsevier [OR APPLICABLE SOCIETY COPYRIGHT OWNER].” Also Lancet special credit - “Reprinted from The Lancet, Vol. number, Author(s), Title of article, Pages No., Copyright (Year), with permission from Elsevier.”

4. Reproduction of this material is confined to the purpose and/or media for which permission is hereby given.

5. Altering/Modifying Material: Not Permitted. However figures and illustrations may be

altered/adapted minimally to serve your work. Any other abbreviations, additions, deletions and/or any other alterations shall be made only with prior written authorization of Elsevier Ltd. (Please contact Elsevier at [permissions@elsevier.com](mailto:permissions@elsevier.com))

6. If the permission fee for the requested use of our material is waived in this instance, please be advised that your future requests for Elsevier materials may attract a fee.

7. **Reservation of Rights:** Publisher reserves all rights not specifically granted in the combination of (i) the license details provided by you and accepted in the course of this licensing transaction, (ii) these terms and conditions and (iii) CCC's Billing and Payment terms and conditions.

8. **License Contingent Upon Payment:** While you may exercise the rights licensed immediately upon issuance of the license at the end of the licensing process for the transaction, provided that you have disclosed complete and accurate details of your proposed use, no license is finally effective unless and until full payment is received from you (either by publisher or by CCC) as provided in CCC's Billing and Payment terms and conditions. If full payment is not received on a timely basis, then any license preliminarily granted shall be deemed automatically revoked and shall be void as if never granted. Further, in the event that you breach any of these terms and conditions or any of CCC's Billing and Payment terms and conditions, the license is automatically revoked and shall be void as if never granted. Use of materials as described in a revoked license, as well as any use of the materials beyond the scope of an unrevoked license, may constitute copyright infringement and publisher reserves the right to take any and all action to protect its copyright in the materials.

9. **Warranties:** Publisher makes no representations or warranties with respect to the licensed material.

10. **Indemnity:** You hereby indemnify and agree to hold harmless publisher and CCC, and their respective officers, directors, employees and agents, from and against any and all claims arising out of your use of the licensed material other than as specifically authorized pursuant to this license.

11. **No Transfer of License:** This license is personal to you and may not be sublicensed, assigned, or transferred by you to any other person without publisher's written permission.

12. **No Amendment Except in Writing:** This license may not be amended except in a writing signed by both parties (or, in the case of publisher, by CCC on publisher's behalf).

13. **Objection to Contrary Terms:** Publisher hereby objects to any terms contained in any purchase order, acknowledgment, check endorsement or other writing prepared by you, which terms are inconsistent with these terms and conditions or CCC's Billing and Payment terms and conditions. These terms and conditions, together with CCC's Billing and Payment terms and conditions (which are incorporated herein), comprise the entire agreement between you and publisher (and CCC) concerning this licensing transaction. In the event of any conflict between your obligations established by these terms and conditions and those established by CCC's Billing and Payment terms and conditions, these terms and conditions

shall control.

14. **Revocation:** Elsevier or Copyright Clearance Center may deny the permissions described in this License at their sole discretion, for any reason or no reason, with a full refund payable to you. Notice of such denial will be made using the contact information provided by you. Failure to receive such notice will not alter or invalidate the denial. In no event will Elsevier or Copyright Clearance Center be responsible or liable for any costs, expenses or damage incurred by you as a result of a denial of your permission request, other than a refund of the amount(s) paid by you to Elsevier and/or Copyright Clearance Center for denied permissions.

#### LIMITED LICENSE

The following terms and conditions apply only to specific license types:

15. **Translation:** This permission is granted for non-exclusive world **English** rights only unless your license was granted for translation rights. If you licensed translation rights you may only translate this content into the languages you requested. A professional translator must perform all translations and reproduce the content word for word preserving the integrity of the article. If this license is to re-use 1 or 2 figures then permission is granted for non-exclusive world rights in all languages.

16. **Website:** The following terms and conditions apply to electronic reserve and author websites:

**Electronic reserve:** If licensed material is to be posted to website, the web site is to be password-protected and made available only to bona fide students registered on a relevant course if:

This license was made in connection with a course,

This permission is granted for 1 year only. You may obtain a license for future website posting,

All content posted to the web site must maintain the copyright information line on the bottom of each image,

A hyper-text must be included to the Homepage of the journal from which you are licensing at <http://www.sciencedirect.com/science/journal/xxxxx> or the Elsevier homepage for books at <http://www.elsevier.com> , and

Central Storage: This license does not include permission for a scanned version of the material to be stored in a central repository such as that provided by Heron/XanEdu.

17. **Author website** for journals with the following additional clauses:

All content posted to the web site must maintain the copyright information line on the bottom of each image, and the permission granted is limited to the personal version of your paper. You are not allowed to download and post the published electronic version of your article (whether PDF or HTML, proof or final version), nor may you scan the printed edition to create an electronic version. A hyper-text must be included to the Homepage of the journal from which you are licensing at <http://www.sciencedirect.com/science/journal/xxxxx> . As part of our normal production process, you will receive an e-mail notice when your article appears on Elsevier's online service ScienceDirect ([www.sciencedirect.com](http://www.sciencedirect.com)). That e-



mail will include the article's Digital Object Identifier (DOI). This number provides the electronic link to the published article and should be included in the posting of your personal version. We ask that you wait until you receive this e-mail and have the DOI to do any posting.

Central Storage: This license does not include permission for a scanned version of the material to be stored in a central repository such as that provided by Heron/XanEdu.

18. **Author website** for books with the following additional clauses:

Authors are permitted to place a brief summary of their work online only.

A hyper-text must be included to the Elsevier homepage at <http://www.elsevier.com>. All content posted to the web site must maintain the copyright information line on the bottom of each image. You are not allowed to download and post the published electronic version of your chapter, nor may you scan the printed edition to create an electronic version.

Central Storage: This license does not include permission for a scanned version of the material to be stored in a central repository such as that provided by Heron/XanEdu.

19. **Website** (regular and for author): A hyper-text must be included to the Homepage of the journal from which you are licensing at <http://www.sciencedirect.com/science/journal/xxxxx>. or for books to the Elsevier homepage at <http://www.elsevier.com>

20. **Thesis/Dissertation**: If your license is for use in a thesis/dissertation your thesis may be submitted to your institution in either print or electronic form. Should your thesis be published commercially, please reapply for permission. These requirements include permission for the Library and Archives of Canada to supply single copies, on demand, of the complete thesis and include permission for UMI to supply single copies, on demand, of the complete thesis. Should your thesis be published commercially, please reapply for permission.

21. **Other Conditions**: Permission is granted to submit your article in print and electronic format. This license permits you to post this Elsevier article online if it is embedded within your thesis. You are also permitted to post your Author Accepted Manuscript online however posting of the final published article is prohibited. Please refer to Elsevier's Posting Policy for further information:

<http://www.elsevier.com/wps/find/authors.authors/postingpolicy>

v1.6

**If you would like to pay for this license now, please remit this license along with your payment made payable to "COPYRIGHT CLEARANCE CENTER" otherwise you will be invoiced within 48 hours of the license date. Payment should be in the form of a check or money order referencing your account number and this invoice number RLNK501089925.**

**Once you receive your invoice for this order, you may pay your invoice by credit card. Please follow instructions provided at that time.**

# CURRICULUM VITAE

MATTHEW P. QUINN

MD/PhD Candidate

## EDUCATION

Degree	Institution	Specialty	Date
MD/PhD	University of Western Ontario	Medical Imaging	09/2010 – ongoing
BSc	University of Western Ontario	Medical Physics	09/2006 – 04/2010

## HONORS & AWARDS

<i>London Imaging Day 2<sup>nd</sup> Place Poster Presentation</i> Amount: \$150	06/2012
<i>Vanier Canada Graduate Scholarship</i> Government of Canada, CIHR Academic and research excellence. Amount: \$150 000	05/2011 – 04/2014
<i>CIHR Master's Award (declined)</i> CIHR Academic, research excellence. Amount: \$17 500	09/2011
<i>MS Society of Canada Ph.D. Studentship (declined)</i> Multiple Sclerosis Society of Canada Academic and research excellence. Amount: \$20 000	05/2011
<i>Schulich Graduate Scholarship</i> The University of Western Ontario Academic excellence. Amount: \$8271/year	09/2010 – 08/2013

<p><i>NSERC Undergraduate Student Research Award</i>  The University of Western Ontario  Academic excellence, research potential.  Amount: \$9000</p>	05/2010 – 08/2010
<p><i>Governor General's Academic Medal – Silver</i>  The University of Western Ontario  Highest academic standing in graduating class.</p>	06/2010
<p><i>Western Gold Medal – Medical Physics</i>  The University of Western Ontario  Highest academic standing, Medical Physics</p>	06/2010
<p><i>Strik-Coupric-Inch Cancer Research Course Prize</i>  The University of Western Ontario  Highest standing in Medical Biophysics 4467B:  “Radiobiology with Medical Applications”</p>	06/2010
<p><i>Donald R. Hay Prize</i>  The University of Western Ontario  Highest standing in Physics 4999E:  “Undergraduate honors thesis project”</p>	06/2010
<p><i>John Gordon McIntosh Scholarship</i>  The University of Western Ontario  Highest standing in 3<sup>rd</sup> Year Physics.  Amount: \$700</p>	04/2010
<p><i>Robert and Ruth Lumsden Scholarship in Science</i>  The University of Western Ontario  Academic excellence in the Faculty of Science.  Amount: \$700</p>	04/2010
<p><i>NSERC Undergraduate Student Research Award</i>  The University of Western Ontario  Academic excellence, research potential.  Amount: \$8600</p>	05/2009 – 08/2009
<p><i>Continuing Admission Scholarship</i>  The University of Western Ontario  Entrance average &gt; 95%  Amount: \$10 000</p>	09/2006 – 04/2010

- National Merit Scholarship* 09/2006  
 The University of Western Ontario  
 All-round excellence.  
 Amount: \$2000
- Governor General's Academic Medal – Bronze* 09/2006  
 Medway High School  
 Highest standing in high school graduating class.

## RESEARCH EXPERIENCE

- PhD Candidate 09/2010 – 07/2013  
 Project: “Imaging iron in early multiple sclerosis at 3 Tesla”  
 Supervisor: Dr. Ravi Menon, PhD
- Undergraduate research student (16 month project) 05/2009 – 08/2010  
 Project: “Investigation of the radiation response of metastatic cancer cells using a novel three-dimensional cell-culture environment”  
 Supervisor: Dr. Eugene Wong, PhD, FCCPM

## PUBLICATIONS

- Quinn, MP**, Menon, RS, Kremenchutzky, M. “Venocentric lesions: an MRI marker of MS?” *Front Neurol* 2013. 4: Article 98. doi: 10.3389/fneur.2013.00098
- Quinn, MP**, Gati, JS, Klassen, LM, Lee, DH, Menon, RS. “Increased deep gray matter iron is present in clinically isolated syndromes.” *MSARD* 2013. *In press*, doi: 10.1016/j.msard.2013/06/017
- Quinn, MP**, Gati, JS, Klassen, LM, Lee, AW, Bird, JR, Leung, SE, Menon, RS. “Comparison of multi-echo post-processing schemes for susceptibility weighted imaging using linear and non-linear mask functions.” *AJNR Am J Neuroradiol* 2013. doi: 10.3174/ajnr.A3584

## PRESENTATIONS

### *Refereed presentations: Platform*

**Quinn, MP**, Gati, JS, Klassen, LM, Lee, DH, Kremenchutzky, M, Menon, RS. “No relation between iron accumulation and narrowed internal jugular veins in early multiple sclerosis.” London Imaging Discovery, London, ON, June 13, 2013.

**Quinn, MP**, Gati, JS, Klassen, LM, Lee, DH, Kremenchutzky, M, Menon, RS. “Abnormal iron deposition and narrowed internal jugular veins in early multiple sclerosis.” London Health Research Day, London, ON, March 19, 2013.

### *Refereed presentations: Poster*

**Quinn, MP**, Gati, JS, Klassen, LM, Lee, DH, Kremenchutzky, M, Menon, RS. “Abnormal iron deposition & narrowed internal jugular veins in early MS.” ISMRM Workshop on Multiple Sclerosis as a Whole Brain Disease, London, UK, June 2013.

**Quinn, MP**, Gati, JS, Klassen, LM, Menon, RS. “Time of flight magnetic resonance venography of the internal jugular veins.” 21<sup>st</sup> Annual Meeting of ISMRM, Salt Lake City, UT, April 2013.

**Quinn, MP**, Klassen, LM, Gati, JS, Menon, RS. “Novel post-processing for susceptibility weighted imaging.” London Imaging Day, London, ON, June 27, 2012.

**Quinn, MP**, Klassen, LM, Gati, JS, Menon, RS. “Frequency-based multi-echo susceptibility weighted imaging.” 20<sup>th</sup> Annual Meeting of ISMRM, Melbourne, Australia, May 2012.

**Quinn, MP**, Menon, RS. “Small veins of what diameters are visible in typical susceptibility weighted sequences?” 20<sup>th</sup> Annual Meeting of ISMRM, Melbourne, Australia, May 2012.

**Quinn, MP**, Rudko, DA, Klassen, LM, Gati, JS, Lee, DH, Kremenchutzky, M, Menon, RS. “Using susceptibility contrasts to study multiple sclerosis.” 2012 UofT Neuroinflammation Symposium and MB-ON endMS RRTC Research Retreat, King City, ON, March 30, 2012.

**Quinn, MP**, Klassen, LM, Gati, JS, Menon, RS. “Multi-echo susceptibility weighed imaging.” London Health Research Day, London, ON, March 20, 2012.

**TEACHING EXPERIENCE**

Physics Instructor 04/2009 – ongoing  
Medical College Admissions Test Preparation Course  
Employer: The Princeton Review  
Courses taught: 15

**INSTITUTIONAL SERVICE**

Invited participant, Physics and Astronomy Curriculum Review 09/2010  
President, Physics and Astronomy Student Association 05/2009 – 04/2010